

FORMATION OF SEMICONDUCTOR NANOCRYSTALS IN SiO<sub>2</sub> BY ION  
IMPLANTATION

A THESIS SUBMITTED TO  
THE GRADUATE SCHOOL OF NATURAL AND APPLIED SCIENCES  
OF  
MIDDLE EAST TECHNICAL UNIVERSITY

BY

UĞUR SERİNCAN

IN PARTIAL FULFILLMENT OF THE REQUIREMENTS FOR THE DEGREE OF

DOCTOR OF PHILOSOPHY

IN

PHYSICS

JUNE 2004

Approval of the Graduate School of Natural and Applied Sciences.

---

Prof. Dr. Canan Özgen  
Director

I certify that this thesis satisfies all the requirements as a thesis for the degree of Doctor of Philosophy.

---

Prof. Dr. Sinan Bilikmen  
Head of Department

This is to certify that we have read this thesis and that in our opinion it is fully adequate, in scope and quality, as a thesis for the degree of Doctor of Philosophy.

---

Prof. Dr. Raşit Turan  
Supervisor

Examining Committee Members

Prof. Dr. Hüsnü Özkan (METU,PHYS) \_\_\_\_\_

Prof. Dr. Raşit Turan (METU,PHYS) \_\_\_\_\_

Prof. Dr. Yalçın Elerman (AU,PHYS ENG) \_\_\_\_\_

Prof. Dr. Macit Özenbaş (METU,METE) \_\_\_\_\_

Prof. Dr. Şinasi Ellialtıođlu (METU,PHYS) \_\_\_\_\_

**I hereby declare that all information in this document has been obtained and presented in accordance with academic rules and ethical conduct. I also declare that, as required by these rules and conduct, I have fully cited and referenced all material and results that are not original to this work.**

Name, Last name : Uğur, Serincan

Signature :

## ABSTRACT

### FORMATION OF SEMICONDUCTOR NANOCRYSTALS IN SiO<sub>2</sub> BY ION IMPLANTATION

Serincan, Uğur

Ph.D., Department of Physics

Supervisor: Prof. Dr. Raşit Turan

June 2004, 111 pages.

In this study, we used ion implantation technique to synthesize semiconductor (Ge, Si) nanocrystals in SiO<sub>2</sub> matrix. Ge and Si nanocrystals have been successfully formed by Ge and Si implantation and post annealing. Implanted samples were examined by characterization techniques such as TEM, XPS, EDS, SAD, SIMS, PL, Raman and FTIR spectroscopy and the presence of Ge and Si nanocrystals in the SiO<sub>2</sub> matrix has been evidenced by these measurements. It was shown that implantation dose, implantation energy, annealing temperature, annealing time and annealing ambient are important parameters for the formation and evolution of semiconductor nanocrystals embedded in SiO<sub>2</sub> matrix. The size and size distribution of Ge and Si nanocrystals were estimated successfully by fitting Raman and PL spectra obtained from Ge and Si implanted samples,

respectively. It was demonstrated that Si implanted and post annealed samples exhibit two broad PL peaks at  $\sim 625$  and  $850$  nm, even at room temperature. Origin of these peaks was investigated by temperature, excitation power and excitation wavelength dependence of PL spectrum and etch-measure experiments and it was shown that the peak observed at  $\sim 625$  nm is related with defects (clusters or chain of Si located near the surface) while the other is related to the Si nanocrystals. As an expected effect of quantum size phenomenon, the peak observed at  $\sim 850$  nm was found to depend on the nanocrystal size. Finally, the formation and evolution of Ge and Si nanocrystals were monitored by FTIR spectroscopy and it was shown that the deformation in  $\text{SiO}_2$  matrix caused by ion implantation tends to recover itself much quicker in the case of the Ge implantation. This is a result of effective segregation of Ge atoms at relatively low temperatures.

Keywords: Si, Ge,  $\text{SiO}_2$ , nanocrystal, ion implantation, Photoluminescence.

## ÖZ

# SiO<sub>2</sub> İÇİNDE YARIİLETKEN NANOKRİSTALLERİN İYON EKME TEKNİĞİ İLE OLUŞTURULMASI

Serincan, Uğur

Doktora , Fizik Bölümü

Tez Yöneticisi: Prof. Dr. Raşit Turan

Haziran 2004, 111 sayfa.

Biz bu çalışmada, SiO<sub>2</sub> matris içinde yarıiletken (Ge, Si) nanokristallerinin oluşturulması için iyon ekme tekniği kullandık. Ge ve Si nanokristalleri, Ge ve Si ekimi ve fırınlamanın ardından başarı ile oluşturuldu. Ekilmiş örnekler, TEM, XPS, EDS, SAD, SIMS, PL, Raman ve FTIR spektroskopisi gibi teknikler kullanılarak incelendi ve Ge ve Si nanokristallerinin SiO<sub>2</sub> matris içindeki varlığı bu ölçümlerle kanıtlandı. SiO<sub>2</sub> matris içerisine yerleştirilen yarıiletken nanokristallerin oluşumunda ve gelişiminde, iyon ekme dozunun, iyon ekme enerjisinin, fırınlama sıcaklığının, fırınlama süresinin ve fırınlama atmosferinin önemli parametreler olduğu gösterildi. Ge ve Si nanokristallerinin büyüklükleri ve büyüklük dağılımları, Ge ve Si ekilmiş örneklerden elde edilen Raman ve PL spektrumları teorik değerlere uydurularak, başarılı bir şekilde hesaplandı. Si ekilmiş ve

ardından fırınlanmış örneklerin, oda sıcaklığında bile, 625 ve 850 nm civarında iki geniş PL tepesi sergilediği gösterildi. Bu tepelerin kaynağı, PL spektrumunun sıcaklık, uyarma gücü ve uyarma dalgaboyu bağımlılığı ve kaldır-ölç deneyleriyle araştırıldı ve 625 nm civarındaki tepenin kusurlarla (yüzeyin yakınında bulunan Si halkaları veya öbekleri) ilgili olduğu, diğer tepeninse Si nanokristalleriyle ilgili olduğu gösterildi. Kuantum büyüklük fenomeninin beklenen bir etkisi olarak, 850 nm civarındaki tepenin nanokristal büyüklüğüne bağlı olduğu bulundu. Son olarak, Ge ve Si nanokristallerinin oluşumu ve gelişimi FTIR spektroskopisi tarafından gözlemlendi ve iyon ekiminin SiO<sub>2</sub> matris içerisinde sebep olduğu bozulmanın, Ge ekilmiş örneklerde, kendini çok daha hızlı onarmaya yatkın olduğu gösterildi. Bu Ge atomlarının efektif segregasyonunun göreceli olarak düşük sıcaklıklarda gerçekleşmesinin bir sonucudur.

Anahtar Kelimeler: Si, Ge, SiO<sub>2</sub>, nanokristal, iyon ekme, Fotolüminesans.

## ACKNOWLEDGMENTS

First of all, I would like to express my gratitude to my supervisor Prof. Dr. Raşit Turan, for having provided me excellent working conditions, encouragement and guidance throughout this study. I could summarize my feelings as: “If you have chance to work with him don’t miss it.”

I would like to thank my committee members Prof. Dr. Hüsni Özkan, Prof. Dr. Yalçın Elerman, Prof. Dr. Macit Özenbaş and Prof. Dr. Şinasi Ellialtıođlu for their time and helpful comments.

The author is most grateful to his family members for their continued moral support and love. Especially his sister, Fehmiye, for joining his Ph. D. dissertation and his mother and father for their invaluable patience and love.

He wishes to thank all colleagues and friends from the lab. Many thanks to Bülent Aslan for helpful discussions and a lot of good time spent together. Thanks to Ayşe Seyhan, Sema Memiş, Gülnur Aygün, Mustafa Kulakçı, Selçuk Yerci, Mustafa Arıkan and Yücel Eke. He would like to express his thanks to Terje G. Finstand for TEM, Giray Kartopu for Raman spectroscopy and Temel Büyüklımanlı for SIMS measurements.

He also would like to thank the Scientific and Technical Research Council of Turkey (TUBITAK) for financial support during this study.

To my wife Emine and my son Anıl

## TABLE OF CONTENTS

ABSTRACT . . . . .	iv
ÖZ . . . . .	vi
ACKNOWLEDGMENTS . . . . .	viii
DEDICATION . . . . .	ix
TABLE OF CONTENTS . . . . .	x
LIST OF TABLES . . . . .	xiii
LIST OF FIGURES . . . . .	xiv
CHAPTERS	
1 INTRODUCTION . . . . .	1
1.1 Introduction . . . . .	1
1.2 Size Matters . . . . .	2
1.2.1 Weak Confinement Limit . . . . .	4
1.2.2 Strong Confinement Limit . . . . .	4
1.3 Why Study Semiconductor Nanocrystals Embedded in SiO <sub>2</sub> ? . . . . .	7
1.4 Recent Developments on Semiconductor Nanocrystal Technology . . . . .	8
1.4.1 Nanocrystal Based Flash Memories . . . . .	8
1.4.2 Nanocrystal Based LEDs . . . . .	10
1.4.3 Biotechnology Applications . . . . .	10
2 FORMATION OF Ge OR Si NANOCRYSTALS IN SiO <sub>2</sub> FILMS BY ION IMPLANTATION: EXPERIMENTAL PROCEDURES . . . . .	12
2.1 Introduction . . . . .	12
2.2 SiO <sub>2</sub> Films . . . . .	13

2.3	Ion Implantation . . . . .	13
2.3.1	Ion Implantation System . . . . .	14
2.3.2	Ion Implantation Problems . . . . .	18
2.3.3	Ge Implantation . . . . .	19
2.3.4	Si Implantation . . . . .	20
2.3.5	Ion Concentration Profiles Estimated by TRIM . . . . .	20
2.4	Annealing Process . . . . .	21
2.5	Measurement Systems . . . . .	25
3	THEORY OF CLUSTER FORMATION . . . . .	27
3.1	Classical Nucleation Theory . . . . .	27
3.2	Ostwald Ripening . . . . .	29
3.3	Lifshitz-Wagner Theory . . . . .	33
4	FORMATION AND EVOLUTION OF Ge NANOCRYSTALS . . . . .	36
4.1	Introduction . . . . .	36
4.2	Structural Properties of Ge Implanted SiO <sub>2</sub> Films . . . . .	37
4.2.1	Ge Nanocrystals . . . . .	37
4.2.2	Voids . . . . .	43
5	RAMAN ANALYSIS OF Ge NANOCRYSTALS . . . . .	48
5.1	Introduction . . . . .	48
5.2	Size Determination of Ge Nanocrystals by Raman Line Profile Analysis . . . . .	49
5.2.1	Experimental Procedures . . . . .	49
5.2.2	Theoretical Model . . . . .	50
5.2.3	Results and Discussion . . . . .	51
6	PL SPECTROSCOPY OF Si NANOCRYSTALS . . . . .	61
6.1	Introduction . . . . .	61
6.2	PL Spectroscopy . . . . .	62
6.3	Possible Light Emitting Mechanisms from a Nanocrystal/SiO <sub>2</sub> System . . . . .	65
6.4	PL Spectrum of Si Nanocrystals . . . . .	66

6.4.1	Dependence on Excitation Source . . . . .	68
6.5	Observation of Si Nanocrystal Distribution by Etch-Measure Experiment . . . . .	69
6.6	Temperature Dependence of PL Spectrum . . . . .	74
6.7	Excitation Power Dependence of PL Spectrum . . . . .	75
6.8	Theoretical Results . . . . .	77
6.9	Conclusion . . . . .	82
7	FTIR ANALYSIS OF Si AND Ge NANOCRYSTALS . . . . .	84
7.1	Introduction . . . . .	84
7.2	FTIR Spectroscopy . . . . .	84
7.3	FTIR Results of Si Implanted SiO <sub>2</sub> Films . . . . .	85
7.4	FTIR Results of Ge Implanted SiO <sub>2</sub> Films . . . . .	88
7.5	Conclusion . . . . .	90
8	CONCLUSION . . . . .	93
	REFERENCES . . . . .	97
	APPENDICES	
A	ABBREVIATIONS AND ACRONYMS . . . . .	104
B	PHYSICAL PARAMETERS . . . . .	105
	VITA . . . . .	107

## LIST OF TABLES

2.1	Ge isotopes with corresponding percentages . . . . .	19
2.2	Implantation Parameters for Ge Implanted SiO <sub>2</sub> Samples . . . . .	20
2.3	Si isotopes with corresponding percentages . . . . .	20
2.4	Implantation Parameters for Si Implanted SiO <sub>2</sub> Samples . . . . .	21
5.1	Summary of the $\bar{L}$ , experimental and theoretical peak frequency shift (PFS) and corresponding FWHM values. For experimental and theoretical PFS, 303.3 and 300.0 cm <sup>-1</sup> were used as the bulk Ge value, respectively. . . . .	60
6.1	Parameters and values for the calculation of PL fit. . . . .	80
B.1	Parameters of the most common semiconductors [113]. . . . .	105
B.2	Bond Strengths In Diatomic Molecules [115]. . . . .	105
B.3	Melting Temperatures of Ge, Si and SiO <sub>2</sub> [115]. . . . .	106

## LIST OF FIGURES

1.1	The density of states in different confinement configurations: (a) bulk, (b) quantum well, (c) quantum wire, (d) quantum dot. The conduction band ( $E_c$ ) and valence bands ( $E_v$ ) split into overlapping subbands that become successively narrower as the electron motion is restricted in more dimensions [5]. . . . .	3
1.2	Energy of the absorption onset versus crystallite size calculated according to the effective mass approximation for (a) a number of semiconductor materials [8] and (b) Ge and Si [9]. . . . .	6
1.3	Band structure of (a) direct and (b) indirect gap semiconductors. The electrons and holes are demonstrated by filled and open circles, respectively. . . . .	8
1.4	Process sequence of Si- or Ge-implanted nanocrystal based memory [13]. . . . .	9
1.5	(a) Size dependence of PL emission from CdSe nanocrystals with various sizes. These nanocrystals are commercially available and fabricated by Evident Technologies [32] and (b) By injecting this type of nanocrystals into the mouse it is possible to glow the mouse!(Obtained by Nie & Gao, Georgia Tech/Emory University).	11
2.1	Layout of the Model 200-DF4 System, Top View. . . . .	15
2.2	Layout of the Model 200-DF4 System, Rear View. . . . .	16
2.3	Depth distribution of (a) 30 keV and (b) 100 keV $^{74}\text{Ge}$ implanted $\text{SiO}_2$ matrix with corresponding projected ranges ( $R_p$ ). . . . .	22
2.4	Depth distribution of (a) 30 keV and (b) 100 keV $^{28}\text{Si}$ implanted $\text{SiO}_2$ matrix with corresponding projected ranges ( $R_p$ ). . . . .	23
3.1	Phase separation in supersaturated solid solutions. . . . .	28
3.2	Free energy of formation of a nucleus as a function of its radius [53].	29
3.3	Small crystals have a larger surface area to volume ratio than large crystals. . . . .	30
3.4	Plot of Eq. 3.15. . . . .	34
4.1	TEM cross-section of a sample which is implanted with $^{74}\text{Ge}$ at a dose of $1 \times 10^{17} \text{ cm}^{-2}$ at 100 keV and annealed at 1000 °C for a) 15 min b) 30 min c) 45 min d) 60 min under $\text{N}_2$ atmosphere. . . . .	38

4.2	XPS spectra around $2p_{3/2}$ peak from a sample implanted with $1 \times 10^{17} \text{ cm}^{-2}$ $^{74}\text{Ge}$ . Both spectra are taken after sputtering in from the surface: (a) is from a sample annealed for 15 min at $1000^\circ\text{C}$ and is interpreted as arising from a region with Ge crystalline precipitates, (b) from a sample annealed for 1 h at $1000^\circ\text{C}$ and is interpreted as coming from a region with Ge in an oxidized state probably a SiGe glass. Note that the tabulated binding energies of Ge and $\text{GeO}_2$ around $2p_{3/2}$ peak are 1217 and 1220 eV, respectively.	39
4.3	TEM cross-section of a sample which is implanted with $^{74}\text{Ge}$ at a dose of $1 \times 10^{17} \text{ cm}^{-2}$ at 100 keV and annealed at (a) $800^\circ\text{C}$ and (b) $900^\circ\text{C}$ for 60 min under $\text{N}_2$ atmosphere. . . . .	40
4.4	SIMS depth profile of a $\text{SiO}_2$ layer implanted with a dose of $7 \times 10^{15} \text{ cm}^{-2}$ at 100 keV and annealed at $1050^\circ\text{C}$ for 45 min under $\text{N}_2$ atmosphere. . . . .	41
4.5	TEM cross-section of a sample which is implanted with $^{74}\text{Ge}$ at a dose of $3 \times 10^{16} \text{ cm}^{-2}$ at 100 keV and annealed at $800^\circ\text{C}$ for 60 min under $\text{N}_2$ atmosphere. Lattice fringes and spots in the corresponding diffraction pattern (inset) provide evidence of crystallinity. . .	42
4.6	TEM cross-section of a sample which is implanted with $^{74}\text{Ge}$ at a dose of $3 \times 10^{16} \text{ cm}^{-2}$ at 100 keV and annealed at $1000^\circ\text{C}$ for 60 min under $\text{N}_2$ atmosphere. . . . .	45
4.7	TEM cross-section of a sample which is implanted with $^{74}\text{Ge}$ at a dose of $1 \times 10^{17} \text{ cm}^{-2}$ at 100 keV and annealed at $1000^\circ\text{C}$ for 60 min under $\text{N}_2$ atmosphere: (a) before intense electron beam irradiation and (b) after intense electron beam irradiation. . . . .	47
5.1	The calculated (a) peak frequency and (b) linewidth (FWHM) as a function of Ge crystal size ( $d_{ave}$ ). Corresponding bulk Ge values are indicated. . . . .	52
5.2	Raman spectra for a $1 \times 10^{17} \text{ cm}^{-2}$ $^{74}\text{Ge}$ -implanted $\text{SiO}_2$ film (a) before and (b) after annealing (at $900^\circ\text{C}$ for 45 min under $\text{N}_2$ atmosphere) and (c) bulk Ge. . . . .	53
5.3	Raman spectra for a $\text{SiO}_2$ film implanted with $1 \times 10^{17} \text{ cm}^{-2}$ $^{74}\text{Ge}$ and (a) annealed at $900^\circ\text{C}$ (b) after etching in HF and (c) the difference between curves a and b. . . . .	55
5.4	Experimental background-subtracted Raman spectrum of Ge nanocrystals compared to theoretical Raman spectrum calculated for $\bar{L} = 8.7 \text{ nm}$ and $\sigma = 2.1 \text{ nm}$ using a phonon confinement model. . . .	56

5.5	Raman spectra for the films implanted with $3 \times 10^{16} \text{ cm}^{-2}$ $^{74}\text{Ge}$ . The spectrum of the as-implanted film is amorphous Ge-like. The crystalline Ge peaks in the spectrum of annealed films (squares) are fitted using a phonon confinement model considering spherical nanocrystals (solid lines). Calculated $\bar{L}$ , and annealing temperatures are indicated near the theoretical curves. . . . .	59
6.1	PL setup consisting of a laser, monochromator, CCD and cryostat.	64
6.2	Possible light emitting mechanism of PL from nanocrystal/SiO <sub>2</sub> system: Left: pictorial illustration, right: energy levels including (1) recombination of electron-hole pairs in the nanocrystal, (2) radiative states at the interface between the nanocrystal and SiO <sub>2</sub> matrix (3) luminescent defect centers due to the matrix defects. . . . .	65
6.3	Room temperature PL of a sample which is implanted with $^{28}\text{Si}$ at a dose of $1.5 \times 10^{17} \text{ cm}^{-2}$ at 100 keV and annealed at various temperatures and times. . . . .	67
6.4	Excitation wavelength dependence of a sample implanted with $^{28}\text{Si}$ at a dose of $1.5 \times 10^{17} \text{ cm}^{-2}$ at 100 keV and annealed at 1050 °C for 5 hr. The PL intensity was normalized in order to spot the shift easily. . . . .	68
6.5	The sketch and energy band diagram of nc-Si/SiO <sub>2</sub> structure. . . . .	70
6.6	Depth profile calculated using the TRIM code for a Si implanted sample at a dose of $1.5 \times 10^{17} \text{ cm}^{-2}$ . Corresponding Projected Range ( $R_p$ ) is indicated in the inset. . . . .	71
6.7	Room temperature PL of an etched sample which is implanted with $^{28}\text{Si}$ at a dose of $1.5 \times 10^{17} \text{ cm}^{-2}$ at 100 keV and annealed at 1050 °C for 2 hr under N <sub>2</sub> atmosphere. . . . .	72
6.8	Room temperature PL summary of the peak position of the etched sample. . . . .	72
6.9	Temperature dependent PL of a sample which is implanted with $^{28}\text{Si}$ at a dose of $1.5 \times 10^{17} \text{ cm}^{-2}$ at 100 keV and annealed at 1050 °C for 2 hr under N <sub>2</sub> atmosphere. . . . .	74
6.10	Schematic of the singlet and triplet energy levels, split by the electron-hole exchange energy $\Delta$ . . . . .	76
6.11	Illustration of Auger recombination. Filled and empty circles denote electrons and holes, respectively. Energy released during a transition from the conduction band ( $E_c$ ) to the valence band ( $E_v$ ) is given to another electron or hole. . . . .	77
6.12	Dependence of the PL intensity on the excitation power at room temperature. . . . .	78

6.13	Theoretical PL fit result of a sample which is implanted with $^{28}\text{Si}$ at a dose of $1.5 \times 10^{17} \text{ cm}^{-2}$ at 100 keV and annealed at 1050 °C for (a) 2 hr and (b) 5 hr. . . . .	81
6.14	The variation of PL intensity with temperature. . . . .	82
7.1	FTIR spectra of Si implanted samples. . . . .	86
7.2	Annealing temperature dependence of (a) Si-O stretching frequency, (b) absorption intensity of the Si-O stretching peak, obtained from Si implanted samples. For reference, the as-implanted values are indicated also. . . . .	87
7.3	FTIR spectra of Ge implanted samples. . . . .	89
7.4	Annealing temperature dependence of (a) Si-O stretching frequency, (b) absorption intensity of the Si-O stretching peak, obtained from Ge implanted samples. For reference, the as-implanted values are indicated also. . . . .	91
7.5	Annealing temperature dependence of FWHM of the Si-O stretching peak, obtained from Ge and Si implanted samples. For reference the non-implanted $\text{SiO}_2$ and corresponding as-implanted values are indicated. . . . .	92

## CHAPTER 1

### INTRODUCTION

#### 1.1 Introduction

Getting smaller and smaller ...

It was the Faraday who, in 1856, first started to study the size dependence of the physical properties of a material. He started with very small pieces of gold (nanocrystalline gold) in solution and, by pressing them together, made bigger pieces of gold. His amazement at what he observed is clear from the March 11, 1856 entry in his diary [1] :

. . . and then put on the gold above the convex surface of a rock crystal plano convex lens and pressed it by hand steadily, rocking it a little. This pressure converted the violet or dark tint of the place (of contact) to a beautiful green - far more beautiful than any I have seen in a gold leaf beaten - the effect was perfect.

Faraday was one of the greatest scientists of the 19<sup>th</sup> century. So, it is not all that surprising that his diary continues with, what we now know to be, a rather accurate explanation of this phenomenon:

Has the pressure converted the layer of atoms into a continuous layer by expansion and welding, and is that all the difference? I rather think it is... So it

appears that these different layers are all gold, and owe their different appearances not to composition but to physical differences.

Faraday discovered that the color (or to be more precise: the electronic structure) of a metal can become size dependent below a certain critical size. What this critical size was, and why it was different for the different metals that he investigated, was something that Faraday did not understand, and could not have understood [2]. Many years later, the first experiments were proved that this size dependence of material properties also applied to semiconductors [3].

## 1.2 Size Matters

An explosion of interest in zero-dimensional Si was set off in 1990 with Canham's discovery of the PL properties of porous Si which he attributed to the quantum confinement of carriers [4]. Nowadays, semiconductor nanocrystals embedded in SiO<sub>2</sub> matrix are preferred because of their better performance in PL emission and possibility of producing flash memory devices from these structures.

The semiconductor nanocrystals are quantum dots usually with the size of 2-25 nm. Just as in an atom, the energy levels in nanocrystals are quantized due to the confinement of electrons (see Fig. 1.1). The electron and hole energy states within the nanocrystals are a function of the quantum dot diameter: The smaller the nanocrystals become the larger the difference between energy states. Since all optical and electronic properties are dependent upon the energy and density of electron states, they can be altering by engineering size of these tiny structures. Quantum confinement results in a controlled blue shifting of the bulk energy band

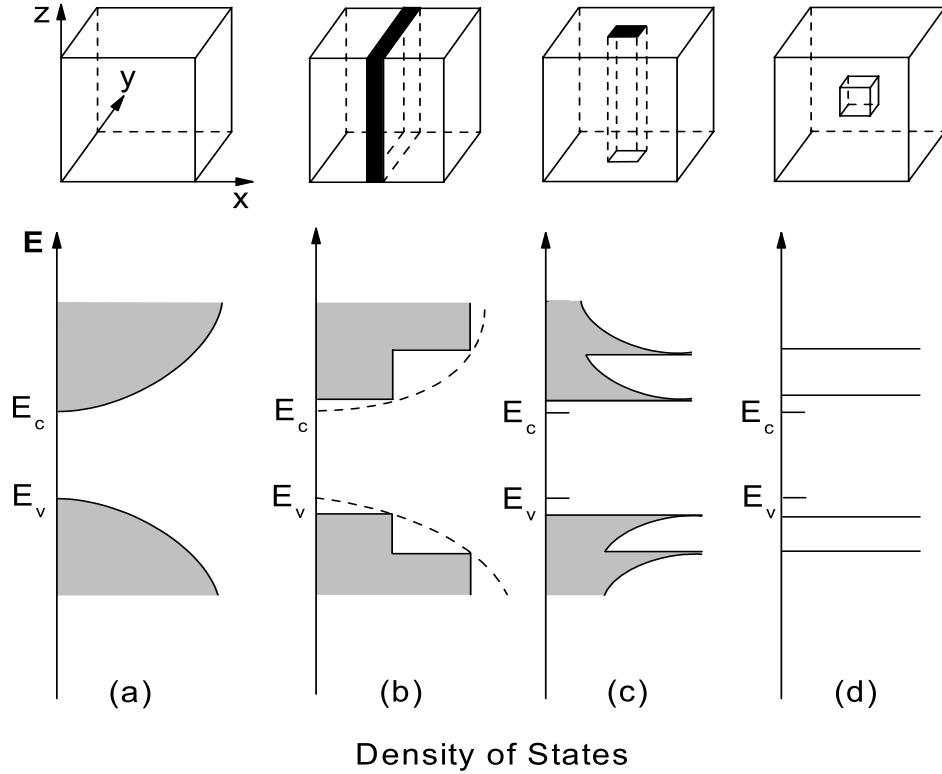


Figure 1.1: The density of states in different confinement configurations: (a) bulk, (b) quantum well, (c) quantum wire, (d) quantum dot. The conduction band ( $E_c$ ) and valence bands ( $E_v$ ) split into overlapping subbands that become successively narrower as the electron motion is restricted in more dimensions [5].

gap. Hence, the peak PL wavelength can be tunable with nanocrystal size.

A. L. Efros and Al. L. Efros [6] proposed a model based on the effective mass approach to describe the dependence of excitonic optical properties on the nanocrystal size. This model deals with the simplest three-dimensional potential well, the spherical potential box with an infinite potential and considers electrons and holes with isotropic effective masses. The main energy terms are the electron-hole interaction energy (the Coulomb term) and the confinement energy of the electron and hole (the kinetic energy term). We describe this model briefly for

the two limiting cases, the so called weak confinement and strong confinement limits.

### 1.2.1 Weak Confinement Limit

Weak confinement limit corresponds to the case when the dot radius,  $a$ , is small but still a few times larger than the exciton Bohr radius,  $a_B$ . In this regime, the exciton, as a single physical entity of mass  $M$ , is confined within a spherical box and the exciton center-of-mass motion is quantized. The dominant energy is the Coulomb term and then the lowest-energy state is the exciton state whose energy is shifted to higher energies by confinement. The shift  $\Delta E$  energy of the ground-state exciton is given approximately by [7]

$$\Delta E \approx \frac{\hbar^2 \pi^2}{2MR^2} \quad (1.1)$$

where  $M$ , the mass of the exciton, is given by  $M = m_e^* + m_h^*$ , with  $m_e^*$  and  $m_h^*$  being the effective masses of the electron and hole, respectively.

### 1.2.2 Strong Confinement Limit

This regime corresponds to the condition  $a \ll a_B$ . This condition states that the confined electron and hole have no bound state corresponding to the hydrogen like exciton. The electrons and holes can be treated as confined independent particles. Hence, the Coulomb term may be ignored and separate size quantization of the electron and hole may be considered as the dominant factor. Then

the shift in the energy as a function of crystallite size can be expressed as [7]

$$\Delta E \approx \frac{\hbar^2 \pi^2}{2\mu R^2} \quad (1.2)$$

in which the exciton mass  $M$  is replaced by the reduced exciton mass  $\mu$  where

$$\frac{1}{\mu} = \frac{1}{m_e^*} + \frac{1}{m_h^*} \quad (1.3)$$

In conclusion, the effective mass approximation provides a description of electronic properties of nanocrystals on the way from crystal-like to cluster-like behavior in terms of particle-in-a-box problem. It predicts a number of size-dependent features due to the three-dimensional spatial confinement of electrons and holes. In order to give an idea about quantum size effect, size dependent band gaps of several semiconductor materials are presented in Fig. 1.2(a). It is observed from this figure that, the quantum confinement results in a monotonic blue shift of the absorption onset with decreasing crystallite size. For the same size range, the effect is more pronounced in GaAs with respect to the CuCl since the exciton Bohr radius of GaAs is much larger than that of CuCl (see Appendix B). With an exciton Bohr radius of 12.5 nm, GaAs obeys the strong confinement limit. In the case of CuCl because of its small exciton Bohr radius,  $a_B = 0.7$  nm, the weak confinement limit occurs in the same size range. For crystallite radius exceeding 20 nm the absorption onset corresponds to that of the bulk crystal while for radii less than 2 nm the validity of the effective mass approximation becomes questionable [8]. Since we concentrate mostly on Ge and Si in this thesis, the corresponding calculated exciton energy [9] is shown as a function of the crystallite radius in Fig. 1.2(b).

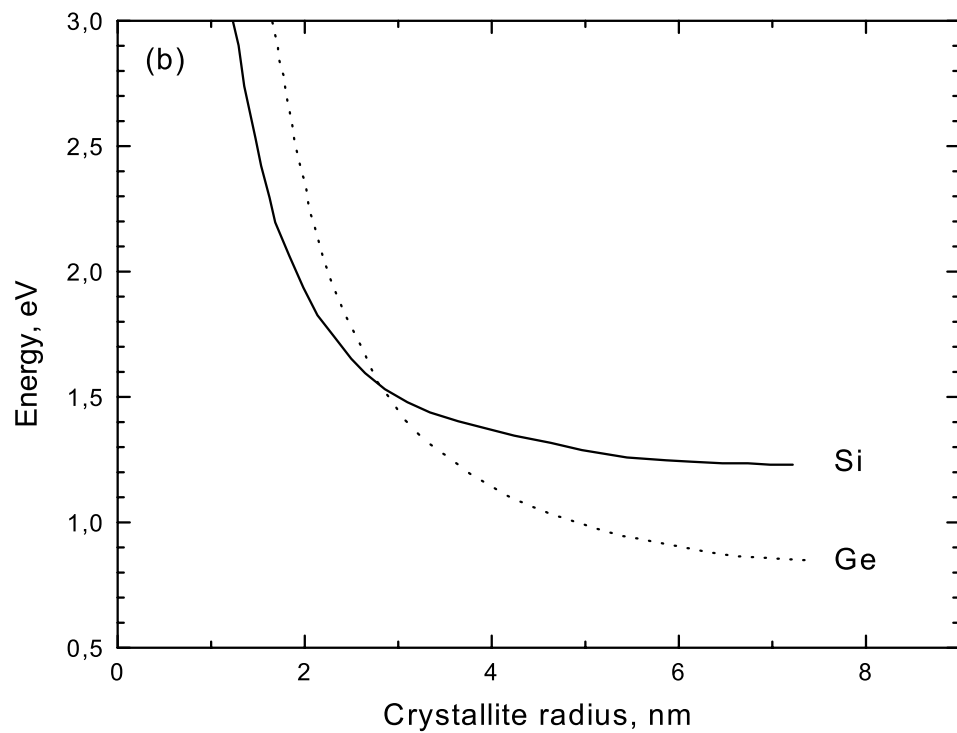
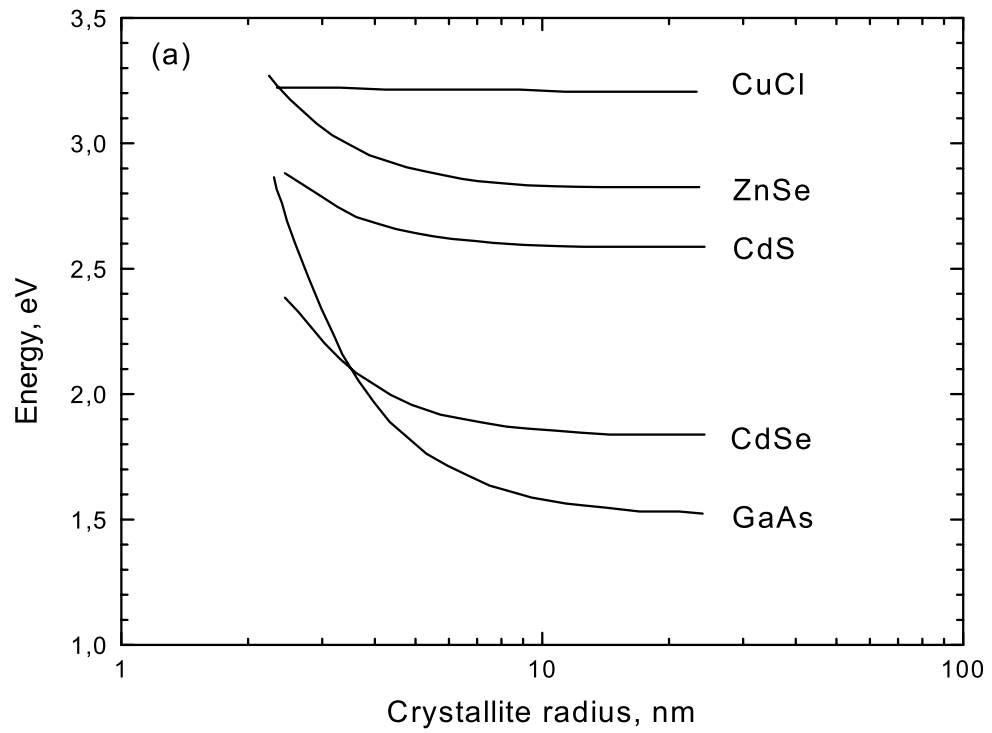


Figure 1.2: Energy of the absorption onset versus crystallite size calculated according to the effective mass approximation for (a) a number of semiconductor materials [8] and (b) Ge and Si [9].

### 1.3 Why Study Semiconductor Nanocrystals Embedded in SiO<sub>2</sub>?

In today's technology, most of the materials contain Si in electronic applications. In contrast to this, light emitting semiconductor devices are fabricated almost exclusively from GaAs and InP because of their efficient light emitting property. This prevents the production of Si-based photonic components integrated with the electronic circuits. Then why do not we use Si instead of GaAs or InP in the production of LEDs? The answer of this question lies in the band structure of Si and GaAs. GaAs and InP are direct band gap semiconductors whereas Si is an indirect band gap semiconductor as illustrated in Fig. 1.3. The fundamental absorption process, where an electron is excited from the valence band to the conduction band is strongly affected by whether the gap is direct or indirect [10]. Since the incoming photon have negligible momentum with respect to that of the electron, the absorbing electron gains energy without changing its wavevector. In a direct gap semiconductor like GaAs, an electron at the valence band maximum performs a vertical transition to the conduction band minimum directly above. For an indirect gap semiconductor like Si, the excited electron needs additional momentum to reach the conduction band minimum at a non-zero wavevector. It gains this momentum by interacting with a phonon. The need for an additional third body interaction with the phonon makes indirect absorption far less probable than direct absorption. Same behavior is valid for the emission process. Hence, Si is an extremely inefficient light emitter. An alternative solution to this problem is to develop an optically efficient silicon-based material.

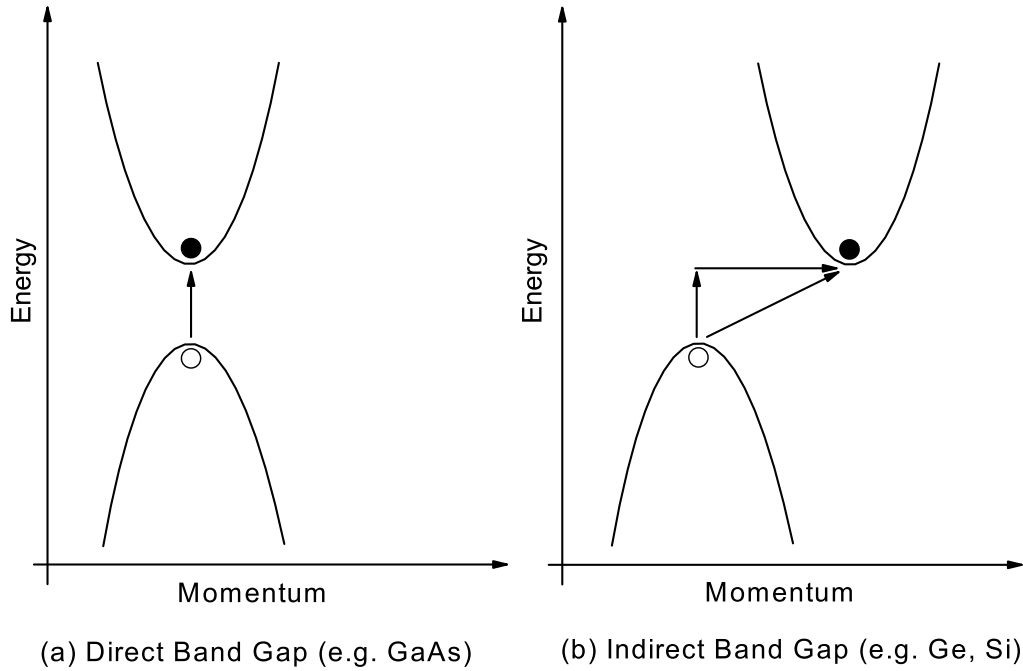


Figure 1.3: Band structure of (a) direct and (b) indirect gap semiconductors. The electrons and holes are demonstrated by filled and open circles, respectively.

Recently, it is found that, semiconductor nanocrystals embedded in  $\text{SiO}_2$  matrix is a way to overcome this problem.

## 1.4 Recent Developments on Semiconductor Nanocrystal Technology

### 1.4.1 Nanocrystal Based Flash Memories

Recently, Ge or Si nanocrystals embedded in the gate oxide of a field effect transistor have attracted much attention due to their applications for memory devices [11-18]. One way of producing such structures is ion implantation technique [13]. With this technique, nanocrystals are introduced through implantation of Ge or Si into thermally grown (5-20 nm) gate oxide as shown in Fig. 1.4.

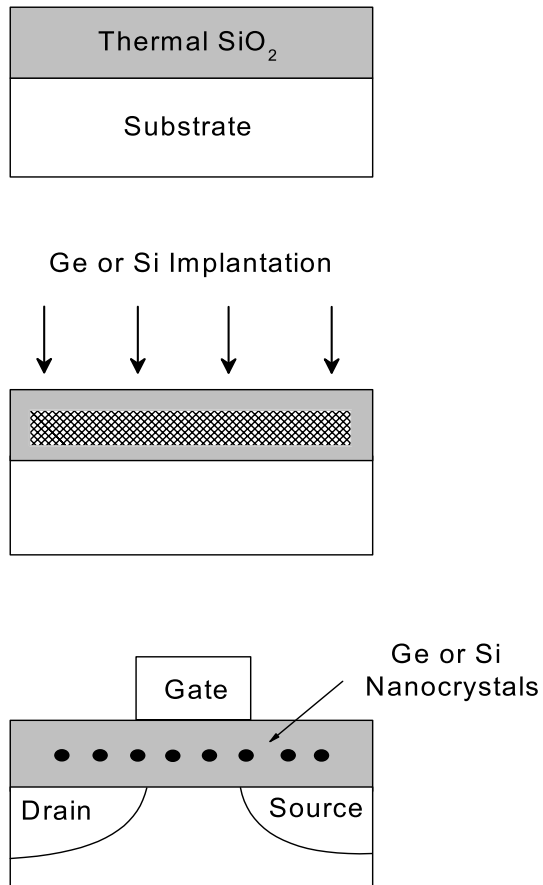


Figure 1.4: Process sequence of Si- or Ge-implanted nanocrystal based memory [13].

Nowadays, Motorola, Inc. reports that it has successfully demonstrated a 4 Mbit memory device based on Si nanocrystals. The company claims that the development of memories that are smaller, more reliable and more energy-efficient than today's floating gate-based flash memories could be possible [19].

Using traditional deposition equipment, researchers at Motorola's DigitalDNA Laboratories, deposited Si nanocrystals resembling 5 nm diameter spheres between two layers of silicon oxide. The Si grains hold charge and prevent lateral

movement of charge to other isolated nanocrystals. This is expected to increase reliability and scalability because a single oxide defect does not lead to complete charge loss as in a conventional floating gate non-volatile memory.

#### 1.4.2 Nanocrystal Based LEDs

After the first demonstration of PL from semiconductor nanocrystals embedded in  $\text{SiO}_2$  matrix, the possibility to fabricate LED, based on these structures, receive much interest. Recently, group IV semiconductor nanocrystals have been investigated extensively because they exhibit EL and thus have potential for used in Si-based LED fabrication [20-31]. Commonly, two EL emission regions (blue-green and red) have been observed in these studies. The blue-green EL, frequently obtained from the Ge nanocrystals [20-23] and the red one obtained from the Si nanocrystals [24-28]. Red EL of Ge nanocrystals embedded in  $\text{SiO}_2$  was not so often reported. Shcheglov et al. [29] observed a broad EL emission in the infrared spectral region from the Ge nanocrystals in  $\text{SiO}_2$  layer. In addition to this, Rebohle et al. [20] and Muller et al. [30] reported EL in the blue region from Si nanocrystals and a good review on blue EL from  $\text{SiO}_2$  layers implanted with group IV elements was presented by Rebohle et al. [31].

#### 1.4.3 Biotechnology Applications

Currently, Evident Technologies [32] has been able to tune the emission of CdSe from 450 nm to 650 nm and the emission of PbSe from 900-2000 nm. The

company has also demonstrated CdS (tunable from 350-470 nm), CdTe (tunable from 600-725 nm), and PbS (tunable from 800-1600nm). Fig. 1.5a shows the nanocrystal size dependent PL emission from CdSe nanocrystals fabricated by Evident Technologies. By using these tunable nanocrystals it is possible to diagnose cancer cells as shown in Fig. 1.5b. The functional organic groups on the nanocrystals can link with a variety of peptides, proteins, DNA, antibodies, etc. so that the dots can bind to and help locate targets like cancer cells, a critical issue in biomedicine.

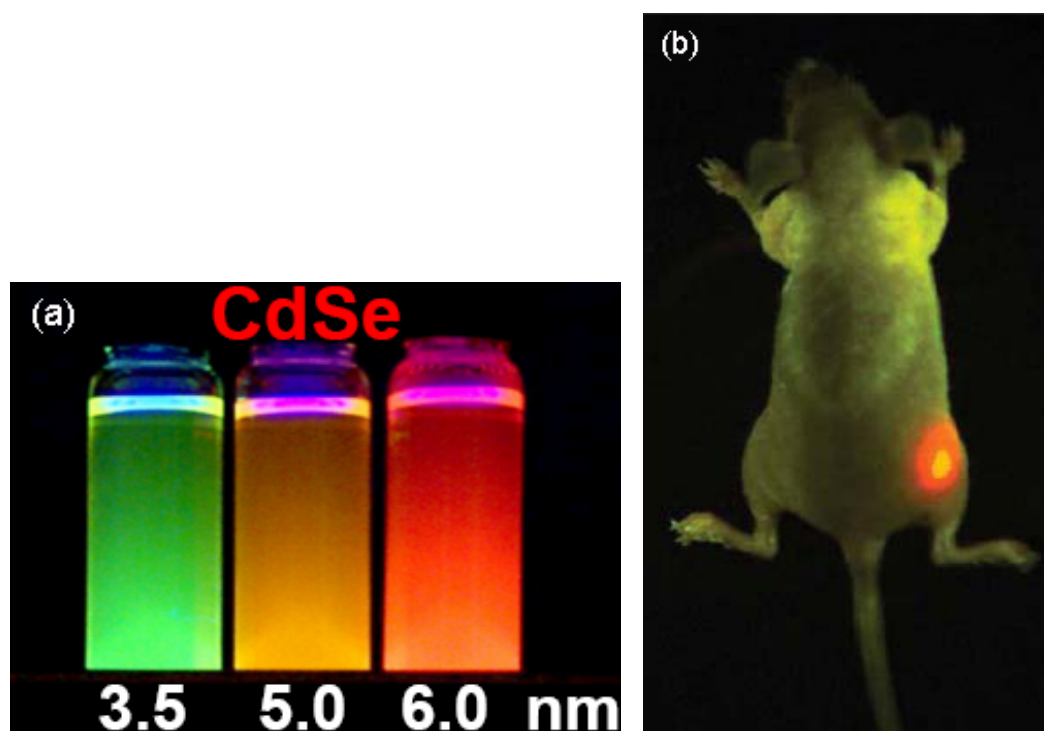


Figure 1.5: (a) Size dependence of PL emission from CdSe nanocrystals with various sizes. These nanocrystals are commercially available and fabricated by Evident Technologies [32] and (b) By injecting this type of nanocrystals into the mouse it is possible to glow the mouse!(Obtained by Nie & Gao, Georgia Tech/Emory University).

## CHAPTER 2

### FORMATION OF Ge OR Si NANOCRYSTALS IN SiO<sub>2</sub> FILMS BY ION IMPLANTATION: EXPERIMENTAL PROCEDURES

#### 2.1 Introduction

Much interest has recently been devoted to semiconductor nanocrystals embedded in SiO<sub>2</sub>. Such materials exhibit efficient luminescence and are capable of storing electrical charge. These properties make them potentially useful in optoelectronic [33] and memory device [34] applications. The properties of a material containing semiconductor nanocrystals depend strongly on the size distribution and the spatial distribution of the nanocrystals within the material. It is important to understand the mechanisms behind the formation of the nanocrystals in order to tailor materials with properties suitable for applications. Various fabrication methods have been proposed to obtain semiconductor nanocrystals embedded in SiO<sub>2</sub> layers such as ion implantation, cosputtering, CVD and MBE [29, 35-39]. Among these, ion implantation has drawn much attention because this technique can produce a controlled depth distribution, particle size and density of the desired species. This chapter presents a study of the effect of variation in different processing parameters on the formation of Ge and Si nanocrystals made by annealing of implanted SiO<sub>2</sub> films.

## 2.2 SiO<sub>2</sub> Films

Different sets of oxide films were used in this study. These sets were prepared by standard thermal oxidation of single-crystal Si wafers for integrated circuit fabrication. These sets were prepared either by dry oxidation or wet oxidation [40]. The thickness of the SiO<sub>2</sub> films vary between 100-900 nm.

## 2.3 Ion Implantation

Ion Implantation is a process that can be used to introduce controlled amounts of impurities into a layer adjacent to a semiconductor surface. In this respect it is similar to conventional semiconductor-processing techniques such as diffusion and alloy regrowth.

The ion implantation technique has been applied to the fabrication of semiconductor devices for the following purposes [41]:

- Doping in general
- Doping drain and source regions of MOSFETs
- Emitter and base doping in BJT
- $V_T$  adjustment in MOSFETs
- Buried layer SiO<sub>2</sub> and CoSi<sub>2</sub>
- SiGe production
- Semiconductor nanocrystal (Ge, Si, etc.) formation in SiO<sub>2</sub> films

### 2.3.1 Ion Implantation System

Varian Model 200-DF4 type implanter was used in this study. Figures 2.1 and 2.2 illustrate the implanter's overall configuration and its major functional components. The ion implantation system can be divided into three parts: Source, beam-line and end-station. All three regions are pumped by oil diffusion pumps, which are backed by direct drive mechanical roughing pumps. With these pumps, it is possible to reach a vacuum level of  $4 \times 10^{-7}$  Torr.

In the ion source (see Fig. 2.1), a tungsten filament is heated up to a temperature at which it emits electrons. Then a gas ( $\text{GeF}_4$ ,  $\text{SiF}_4$ ,  $\text{BF}_3$ , etc.) flows past the tungsten filament, and the gas is ionized and fragmented. If necessary, the gaseous source can be replaced with a solid source and an oven. The ions are extracted from the ion source by an electrical attraction between the source exit aperture and extraction electrode, placed just outside the ion source. The electrical attraction is supplied by a voltage difference of 25 kV between the source and the electrode.

The beam, which consists of a mixture of charged and neutral species, is directed into a magnetic field (analyzer magnet), which separated the charged species according to their mass and charge. This is basically a mass spectrometer.

Equating the force ( $\mathbf{F}$ ) on a moving charged ( $q$ ) species in a magnetic field ( $\mathbf{B}$ ) to the mass ( $M$ ) times the centripetal acceleration:

$$\mathbf{F} = q \mathbf{v} \times \mathbf{B} = \frac{Mv^2}{r} \quad (2.1)$$

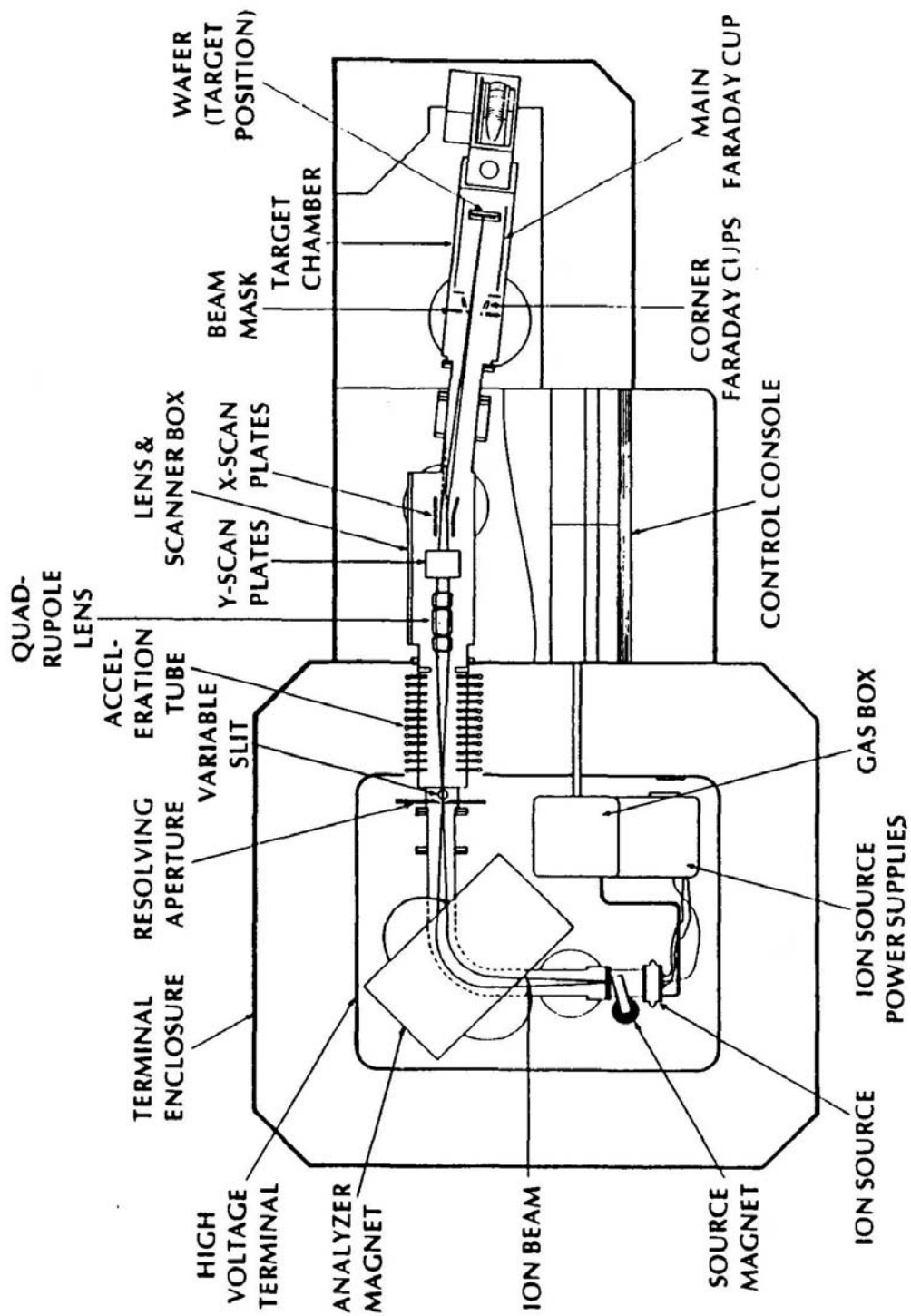


Figure 2.1: Layout of the Model 200-DF4 System, Top View.

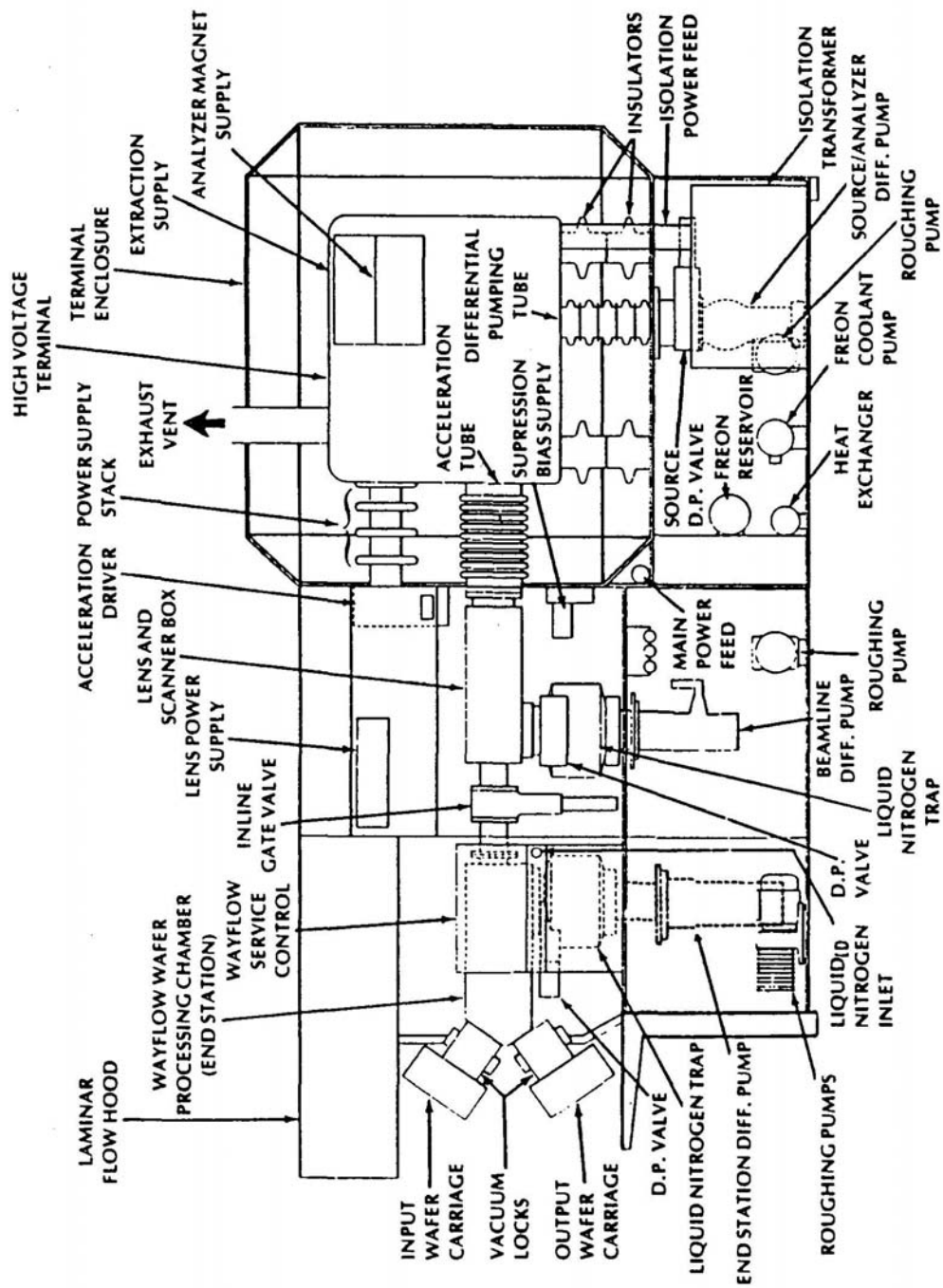


Figure 2.2: Layout of the Model 200-DF4 System, Rear View.

Where  $r$  and  $v$  are the radius of curvature and velocity of the species, respectively.

From the relation between energy and the extraction potential  $V_{ext}$ , the velocity is found as

$$v = \sqrt{\frac{2E}{M}} = \sqrt{\frac{2qV_{ext}}{M}} \quad (2.2)$$

Combining the above two equations,

$$r = \frac{Mv}{qB} = \frac{1}{B} \sqrt{2\frac{M}{q}V_{ext}} \quad (2.3)$$

By varying the magnetic field strength of the analyzer magnet, it is possible to select only those ions desired for the implant. The ions are deflected 90 degrees through the curvature of the magnet chamber for the separation and focused by the magnet at the resolving aperture. All other species except for the selected ions are deflected at angles less or greater than 90 degrees and collected on the magnet chamber walls or on the resolving aperture plate. The ion beam also passes through a variable slit, located just after the resolving aperture. If the slit is placed at the correct position, only the ions with a particular  $r$  will escape the mass spectrometer and eventually reach the sample. People often speak of selecting a particular mass, but one actually selects a particular ratio of mass/charge. For example, the two species  $B^+$  and  $B_2^+$  will both follow the same path (same  $r$ ). In this case, both species will implant B.

The ions that exit the magnetic sector and escape through the slit are accelerated by a large potential (0-200 keV) in the acceleration tube. The added electrostatic energy increases the penetration depth of the ions into the sample. The ion beam diverges as it gains energy through the acceleration tube. A

quadrupole triplet lens located just after the acceleration tube, at the beam-line, converges the ion beam. At the lens & scanner box, the ion beam is focused by the lens. The ion beam travels through one or two deflection fields (scanner), which can raster the beam across the sample. This enables the target area to be covered uniformly with ions. In order to implant ions only in certain regions, an ion implantation mask blocks a portion of the surface.

Neutral species formed in the acceleration tube and in the beam-line after the analyzer region are eliminated from the ion beam by superimposing a constant d.c. voltage across the X-plates, causing the beam to be deflected 7 degrees off its central axis in the horizontal direction. The neutral species, unaffected by this d.c. offset voltage, continue through a straight path and are stopped after the lens & scanner box. The beam-line leading to target chamber is constructed with an offset of 7 degrees allowing the ions reach to the target chamber located at the end-station. Finally, the ions are implanted into the target wafer.

How can the dose be controlled? The wafer is placed inside a Faraday cup (metal container that captures all of the ions from the implanter). If one takes the total current collected by the Faraday cup and divides by the wafer surface area, then you get the dose per unit area.

### 2.3.2 Ion Implantation Problems

If a particle exists on the surface prior to ion implantation, it will shield the underlying substrate, so the local substrate will not be implanted. Poor wafer handling, poor pump down procedures, etc. can introduce particle contamination.

Sometimes diffusion pump oil can be vaporized, with organic contamination eventually deposited onto the substrate. Carbon contamination is extremely difficult to remove from semiconductor substrates. The simplest removal method is to use an ion beam to sputter away the upper layer, but this may also remove desired features. Nitrogen traps on the diffusion pump can reduce this type of contamination.

### 2.3.3 Ge Implantation

In the implantation process  $\text{GeF}_4$  was used as a Ge source. Natural Ge has 5 isotopes with the percentages given in Table. 2.1. Since  $^{74}\text{Ge}$  isotope has the greatest percentage, thus the greatest beam current, among the isotopes it is used as the implanted ions.

Table 2.1: Ge isotopes with corresponding percentages

Isotope of Ge	$^{70}\text{Ge}$	$^{72}\text{Ge}$	$^{73}\text{Ge}$	$^{74}\text{Ge}$	$^{76}\text{Ge}$
Percentage(%)	20.5	27.4	7.8	36.5	7.8

In order to characterize the evolution of the Ge nanocrystals we prepared various sets of samples by using different implantation energies and doses. In Table 2.2 the implantation parameters can be seen.

Table 2.2: Implantation Parameters for Ge Implanted SiO<sub>2</sub> Samples

Sample	Implantation Dose, atoms/cm <sup>2</sup>	Implantation Energy, keV
Ge1	2.0x10 <sup>15</sup>	30
Ge2	7.0x10 <sup>15</sup>	30, 100
Ge3	1.0x10 <sup>16</sup>	30, 100
Ge4	3.0x10 <sup>16</sup>	100
Ge5	6.0x10 <sup>16</sup>	30, 100
Ge6	1.0x10 <sup>17</sup>	100
Ge7	1.5x10 <sup>17</sup>	100

Table 2.3: Si isotopes with corresponding percentages

Isotope of Si	<sup>28</sup> Si	<sup>29</sup> Si	<sup>30</sup> Si
Percentage(%)	92.2	4.7	3.1

#### 2.3.4 Si Implantation

For the Si implantation, SiF<sub>4</sub> was used as a Si source. Natural Si has 3 isotopes with the percentages given in Table. 2.3. With a similar reason for Ge, <sup>28</sup>Si ions were used for the implantation.

In order to form Si nanocrystals, various sets of samples were prepared. Table 2.4 presents the implantation parameters of these samples.

#### 2.3.5 Ion Concentration Profiles Estimated by TRIM

TRIM [42] is a comprehensive software included in SRIM. SRIM is a group of programs using a quantum mechanical treatment of ion-atom collisions. TRIM calculates various parameters related to the interaction of an ion beam with a

solid material by using a Monte Carlo algorithm. It calculates both the final 3D distribution of the ions and also all the kinetic phenomena associated with the ion's energy loss: target damage, sputtering, ionization and phonon production.

Table 2.4: Implantation Parameters for Si Implanted SiO<sub>2</sub> Samples

Sample	Implantation Dose, atoms/cm <sup>2</sup>	Implantation Energy, keV
Si1	4.5x10 <sup>16</sup>	100
Si2	1.5x10 <sup>17</sup>	30, 100

Using TRIM software we obtained the depth distribution of both Ge and Si implanted samples. Figs. 2.3 and 2.4 illustrates the depth distribution of Ge and Si implanted samples with corresponding projected ranges ( $R_p$ ).

## 2.4 Annealing Process

The collisions between high-energy ions and the substrate atoms can damage the near-surface layer. For this reason, the substrate is typically annealed following ion implantation. Samples can be annealed under vacuum or inert gases such as N<sub>2</sub>, O<sub>2</sub> and Ar.

It is well known that formation of semiconductor nanocrystals affected by the various annealing ambient. For example, the presence of O<sub>2</sub> or water vapor in the atmosphere results in the oxidation of Ge or Si atoms and prevents the formation of Ge or Si nanocrytals. Therefore it is better to anneal the implanted samples

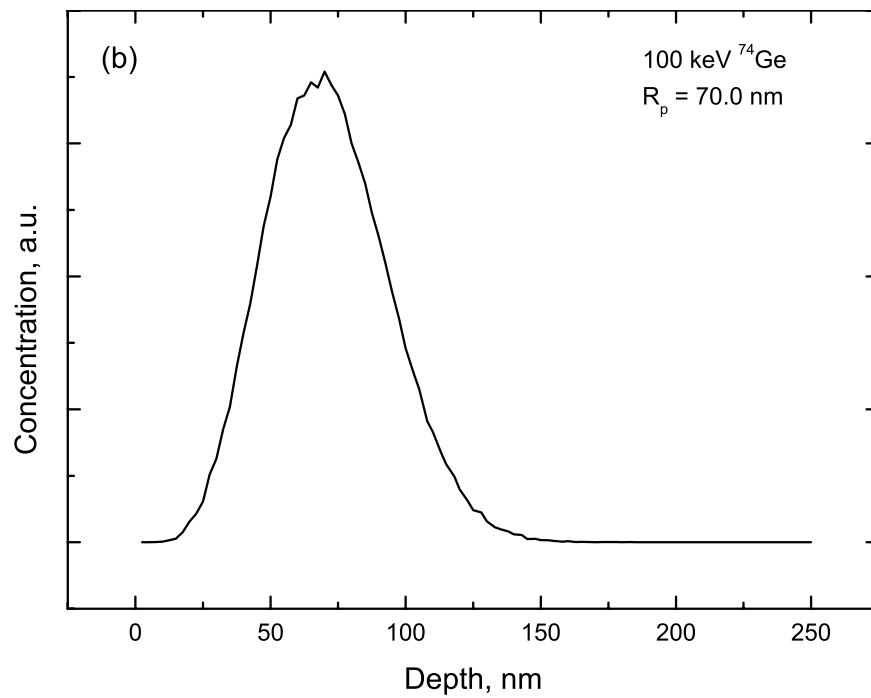
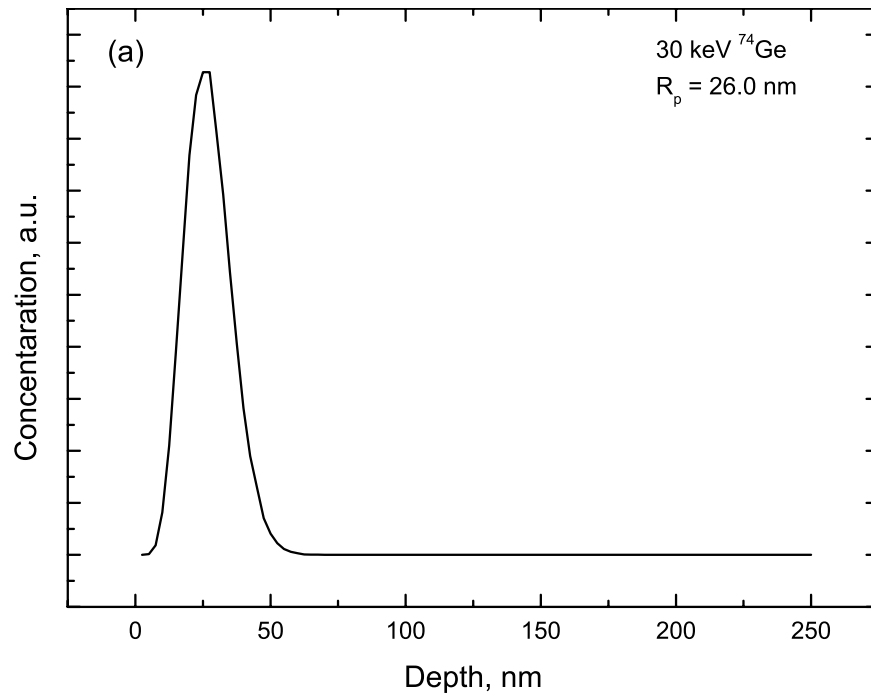


Figure 2.3: Depth distribution of (a) 30 keV and (b) 100 keV  $^{74}\text{Ge}$  implanted  $\text{SiO}_2$  matrix with corresponding projected ranges ( $R_p$ ).

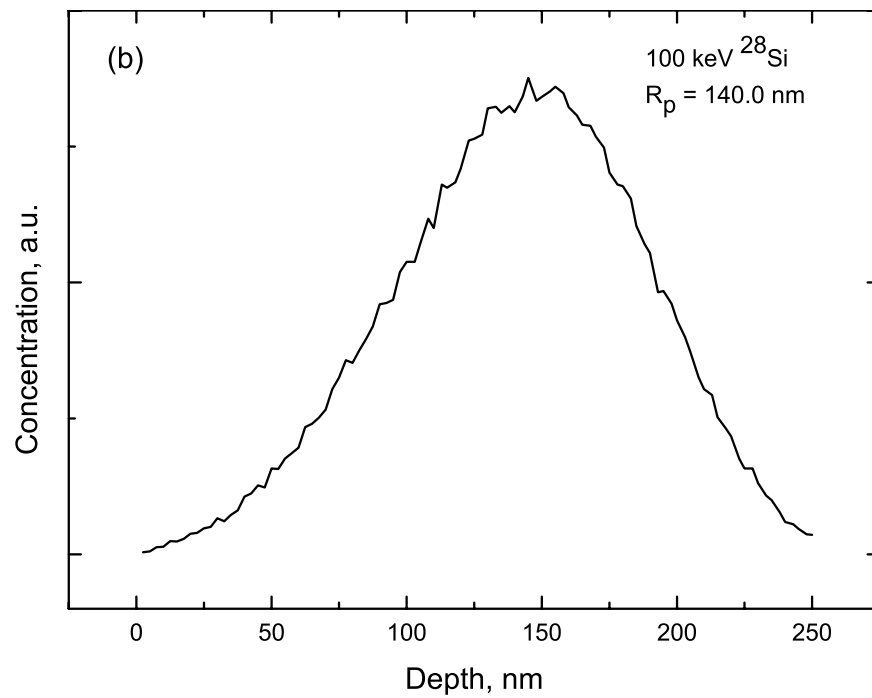
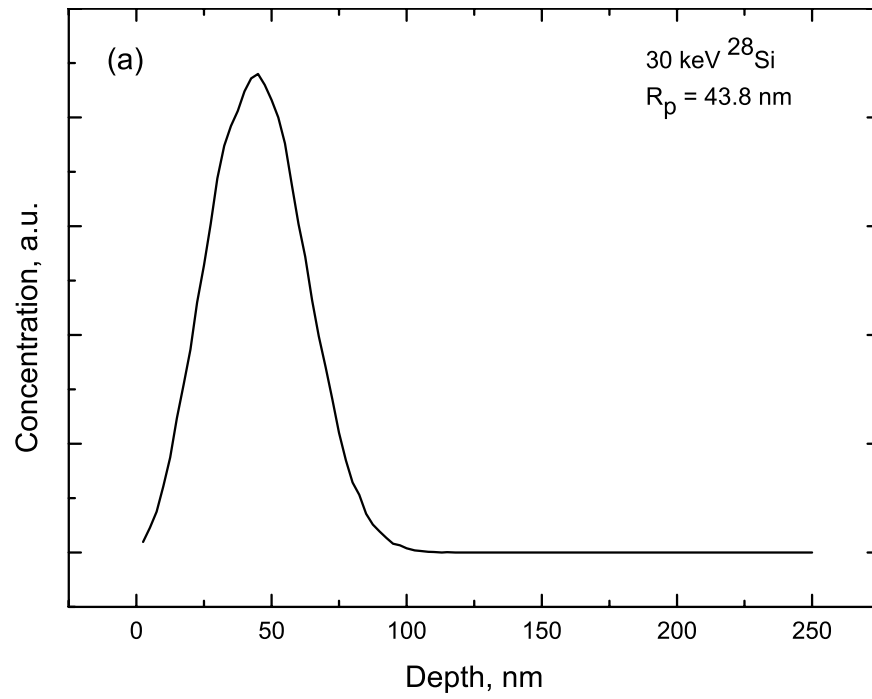


Figure 2.4: Depth distribution of (a) 30 keV and (b) 100 keV  $^{28}\text{Si}$  implanted  $\text{SiO}_2$  matrix with corresponding projected ranges ( $R_p$ ).

under vacuum or  $N_2$  atmosphere to obstruct the oxidation of Ge and Si atoms in the annealing step. On the other hand, annealing under  $O_2$  atmosphere is a way to control the size of the nanocrystals via oxidation [43]. By this way, the surface of the formed nanocrystals are oxidized and hence their sizes decreases. Another important ambient is the  $H_2$  atmosphere which has a passivation effect on the dangling bonds present at the interface between nanocrystals and the  $SiO_2$  matrix [44, 45].  $H_2$  annealing passivates also the bonds in the  $SiO_2$  matrix formed during the implantation.

In addition to the annealing ambient, the annealing temperature also effects the formation of nanocrystals. The diffusivity of the implanted semiconductor is changed by the annealing temperature, causing a difference in the annealing time. For instance, bulk Ge and Si have melting temperatures of 938 and 1414 °C, respectively (see Appendix B). Annealing temperatures higher than these values result in high diffusivity of Ge and Si atoms in the  $SiO_2$  matrix. The duration of the annealing is another process parameter that controls the size and distribution of nanocrystals. In the case of Si, where the melting point is higher than the maximum achievable temperatures of the ovens, longer annealing time is needed to induce the crystallization.

We have a commercial oven that our implanted samples can be annealed under vacuum up to  $10^{-5}$  Torr or inert gases such as  $N_2$  and  $O_2$ . Implanted samples were post annealed under vacuum or  $N_2$  atmosphere at various temperatures and times in order to form Ge or Si nanocrystals .

## 2.5 Measurement Systems

Implanted samples were investigated by TEM, XPS, EDS, SAD at Norway, by SIMS at USA, by Raman spectroscopy at England and by PL and FTIR spectroscopy at METU.

Samples for cross-sectional TEM were prepared using standard techniques. The structure of the different samples was examined at 200 keV using an analytical JEOL 2000 FX TEM and a field emission analytical JEOL 2010 F TEM equipped with a Noran Vantage DI+ EDS system. The composition of selected samples was measured using a Cameca 4F SIMS and the chemical state of elements was analyzed by XPS combined with sputtering (4 keV Ar<sup>+</sup>) in a VG Micro Lab III instrument for combining XPS with Auger Electron Spectroscopy at a residual pressure of 10<sup>-9</sup> mbar with Al K $\alpha$  radiation as excitation source. The binding energies are calibrated against the Si 2p peak from SiO<sub>2</sub> at 103.3 eV.

Raman scattering spectra of the films were obtained before and after annealing, in back-scattering configuration with a Renishaw RM series Raman microscope using a 514.5 nm Ar<sup>+</sup> laser excitation source. All of the measurements were carried out at room temperature, using a total laser power of either 4 or 0.4 mW (on the sample). The beam diameter was 1  $\mu$ m on the sample surface and scattered light was collected with a CCD camera on the head of the microscope. The spectral resolution was 1 cm<sup>-1</sup>.

FTIR measurements were conducted in the absorbance mode (350-2500 cm<sup>-1</sup>,

2 cm<sup>-1</sup> resolution), and the SiO stretching peak, including its intensity, FWHM and frequency, was used to monitor the structural changes of the SiO<sub>x</sub> films with annealing.

Finally, most of the samples were investigated by a PL setup consisting of an excitation source, MS-257 type monochromator, Hamamatsu CCD camera and closed-cycle He cryostat. In our PL experiments, 532 nm NdYag, 337 nm N<sub>2</sub> laser or 1000W Hg-Xe arc lamp was used as an excitation source. NdYag laser is a continuous laser with a maximum power of 3 W while N<sub>2</sub> laser is a pulse laser with an average power of 7 mW. By using the cryostat it is possible to carry out temperature dependent PL experiments between 10-300 K.

## CHAPTER 3

### THEORY OF CLUSTER FORMATION

The problem of particle coarsening [46] was treated in 1900 by W. Ostwald and is often referred to as Ostwald ripening. The modern theory of particle coarsening was developed by Lifshitz and Slyozov [47], C. Wagner [48] and G. W. Greenwood [49] has reviewed the theory. Recently, this theory has been adopted to the nanocrystal formation in dielectric matrices [50]. In the case of the ion implantation, atomic species begin to nucleate following the supersaturation as shown in Fig 3.1. When these nuclei first form they are extremely small, probably on the order of 1 nm, and they are considered to be spherical in shape. During the annealing process, the growth of these tiny structures occurs via a diffusion mechanism. Afterwards, the formed larger grains grow at the expense of smaller grains, so called Ostwald Ripening. The theory of the formation is described below briefly.

#### 3.1 Classical Nucleation Theory

The classical nucleation theory originated from the ideas of Volmer and Weber in 1925 [51]. The change in the Gibbs free energy when a nucleus forms,  $\Delta G$ , is the sum of a bulk and surface term [52]. Then the the free energy change to form

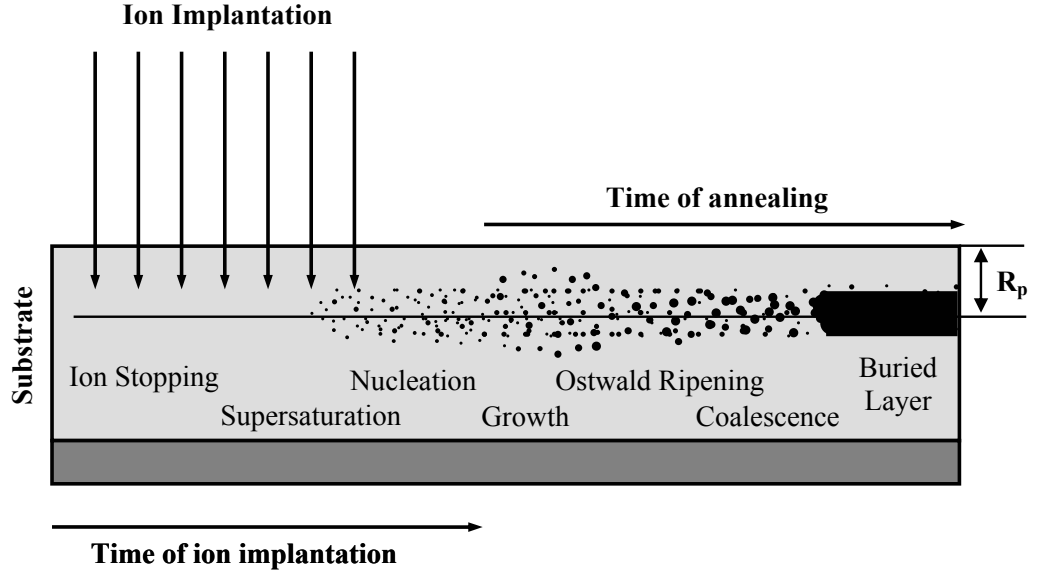
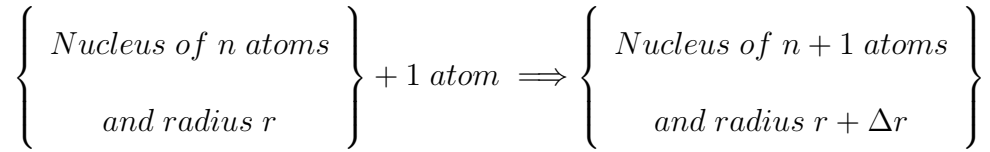


Figure 3.1: Phase separation in supersaturated solid solutions.

a nucleus is

$$\Delta G = \frac{4}{3}\pi r^3 \Delta G_B + 4\pi r^2 \gamma \quad (3.1)$$

where the surface free energy has been simply taken as the surface tension  $\gamma$  and  $\Delta G_B$  is the bulk free energy change. The two terms of Eq. 3.1 are plotted on Fig. 3.2. Now, we are interested in the following reaction:



If the free energy change of the above reaction is negative then a nucleation event is favored. From Fig. 3.2 it is observed that for all values of  $r > r^*$  this reaction has a negative free energy change. Above  $r^*$  growth of a nucleus lowers

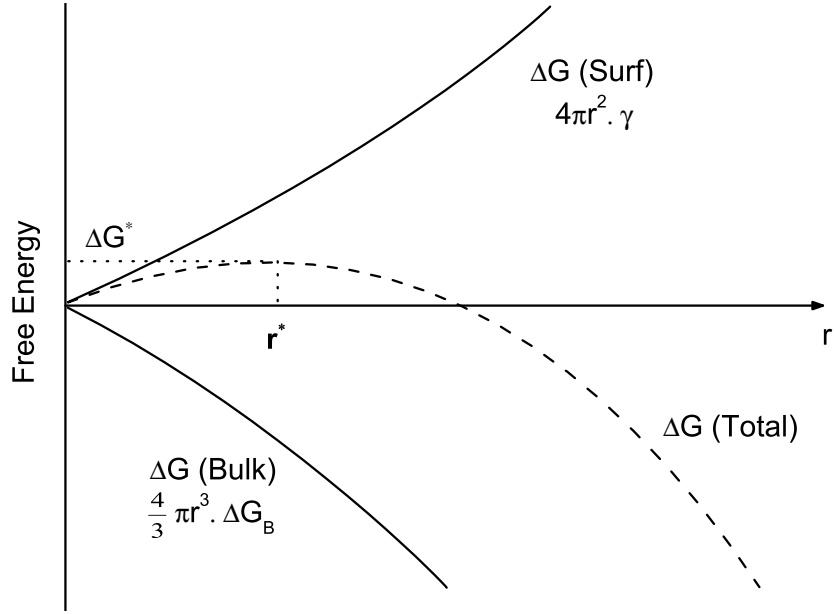


Figure 3.2: Free energy of formation of a nucleus as a function of its radius [53].

the free energy. Therefore,  $r^*$  is a critical radius and its value can be determined from Eq. 3.1 by differentiation as

$$r^* = \frac{-2\gamma}{\Delta G_B} \quad (3.2)$$

Then the free energy change to form a critical sized nucleus,  $\Delta G^*$ , is found by substituting  $r^*$  into Eq. 3.1,

$$\Delta G^* = \frac{16\pi\gamma^3}{3(\Delta G_B)^2} \quad (3.3)$$

### 3.2 Ostwald Ripening

Ostwald ripening is a spontaneous process that occurs because larger crystals are more energetically favored than smaller crystals. While the formation of many

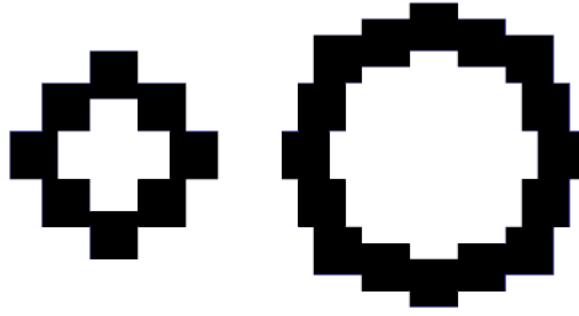


Figure 3.3: Small crystals have a larger surface area to volume ratio than large crystals.

small crystals is kinetically favored, (i.e. they nucleate more easily) large crystals are thermodynamically favored. Thus, from a standpoint of kinetics, it is easier to nucleate many small crystals. However, small crystals have a larger surface area to volume ratio than large crystals (see Fig. 3.3). Molecules on the surface are energetically less stable than the ones already well ordered and packed in the interior. Large crystals, with their greater volume to surface area ratio, represent a lower energy state. Thus, many small crystals will attain a lower energy state if transformed into large crystals and this is what we see in Ostwald ripening.

After the initial period of growth the precipitate phase closely approaches the volume fraction that one would predict from the phase diagram using the lever law [46]. After this time, growth does not stop, but proceeds by a process in which the larger particles grow at the expense of the smaller ones in an effort by the system to reduce the surface potential  $\gamma A$  (similar in these respects to normal grain growth). Consequently, the volume fraction precipitate phase remains essentially

constant so that one may write

$$\sum_{\substack{\text{All particle} \\ \text{sizes}}} \left( \frac{\text{Rate atom loss}}{\text{Particle}} \right) = 0 \quad (3.4)$$

Taking  $V$  as the volume of a particle and  $\bar{V}$  as the volume per atom in the particle, one can write the rate of atom loss from a particle as  $(dV/dt)(1/\bar{V})$ . For a sphere  $dV/dR = 4\pi R^2$ , so that Eq. 3.4 becomes

$$\sum_i \frac{4\pi R_i^2}{\bar{V}} \frac{dR_i}{dt} = 0 \quad (3.5)$$

The rate of atom loss from a particle is controlled by either the rate of transfer across the particle-matrix interface or by diffusion away from the particle into the matrix. Both of these cases has been treated by the Lifshitz-Wagner theory. It is indicated by the experimental results [49, 54] that the growth of coherent precipitates is diffusion controlled. It is assumed that the particle is a single component (i.e., pure element). One may write the rate of atom loss by diffusion from a pure spherical particle of radius  $R$  as

$$J = 4\pi R^2(-D) \left( \frac{dC}{dr} \right)_s \quad (3.6)$$

where  $D$  is the diffusion coefficient in the matrix and  $(dC/dr)_s$  is the radial concentration gradient of the precipitate atoms in the matrix at the particle-matrix surface. An important point here is that the surface concentration is increased above the equilibrium value because of the surface curvature. Since it is assumed that the particle is a pure component, the surface concentration  $C_s$  may be written as

$$C_s = C \left[ 1 + \frac{2\bar{V}\gamma}{kT \cdot R} \right] \quad (3.7)$$

where  $C$  is the equilibrium concentration if the interface were flat and  $\gamma$  is the surface tension (namely, surface free energy). It is clear from Eq. 3.7 that the concentration at the surface of a small particle will be increased more than at the surface of a large particle, so that diffusion will proceed from small to large particles. Since the concentration rise at the surface is quite small, one can assume that the particles advance at near steady-state conditions. Under steady-state conditions one may write the radial concentration gradient at the surface of a sphere of radius  $R$  as

$$\left(\frac{dC}{dr}\right)_s = \frac{C_s - C_0}{R} \quad (3.8)$$

where  $C_0$  is the concentration far from the surface. If we rewrite the rate of atom loss from a particle as

$$\left(\frac{dV}{dt}\right)\left(\frac{1}{\bar{V}}\right) = \left(\frac{dV}{dR}\frac{dR}{dt}\right)\left(\frac{1}{\bar{V}}\right) \quad (3.9)$$

and combine this with Eq. 3.6

$$\left(4\pi R^2\frac{dR}{dt}\right)\left(\frac{1}{\bar{V}}\right) = 4\pi R^2(-D)\left(\frac{dC}{dr}\right)_s \quad (3.10)$$

we obtain

$$\frac{dR}{dt} = -\bar{V}D\left(\frac{dC}{dr}\right)_s \quad (3.11)$$

By substituting Eq. 3.8 in Eq. 3.11 we obtain

$$\frac{dR_i}{dt} = \frac{-\bar{V}D(C_s - C_0)}{R_i} \quad (3.12)$$

By using this equation and Eq. 3.7 we can rewrite Eq. 3.5 as

$$(C_0 - C)\sum_i R_i = nC\frac{2\bar{V}\gamma}{kT} \quad (3.13)$$

where  $n$  is the number of particles that one sums over. The average size  $\bar{R}$  is  $\sum R_i/n$ , so that with a little algebra one obtains

$$C_0 - C_s = \frac{2\bar{V}\gamma}{kT} C \left[ \frac{1}{\bar{R}} - \frac{1}{R} \right] \quad (3.14)$$

Substituting this equation into Eq. 3.11 we obtain

$$\frac{dR}{dt} = \frac{2\gamma\bar{V}^2 DC}{kT} \frac{1}{R^2} \left[ \frac{R}{\bar{R}} - 1 \right] \quad (3.15)$$

Fig. 3.4 shows the plot of this equation. It is clearly seen from the graph that particles of radius  $R < \bar{R}$  are dissolving at a rapidly increasing rate. Another important feature of this graph is that if a particle has  $R > 2\bar{R}$  its growth rate slows down with respect to the smaller particles. Consequently, from this simple theory of Greenwood [49] it is not expected to see particles of  $R > 2\bar{R}$  in the system. In addition to these, the net growth would be zero if all particles had the same size,  $\bar{R}$ . If we solve the Eq. 3.15 for particles of maximum size,  $R = R_{max} = 2\bar{R}$ ,

$$R_{max}^3 = (R_{max})_0^3 + 6 \left[ \frac{\bar{V}^2 \gamma C D}{kT} \right] t \quad (3.16)$$

This equation states that particles of size  $2\bar{R}$  be present in the initial distribution. The mean particle size will grow at a slower rate than estimated by this equation. In addition to this, this simple theory cannot determine the mean size growth.

### 3.3 Lifshitz-Wagner Theory

Lifshitz-Wagner theory comes with a different approach by making a statistical analysis [55]. This analysis accounts the fact that a distribution of particles

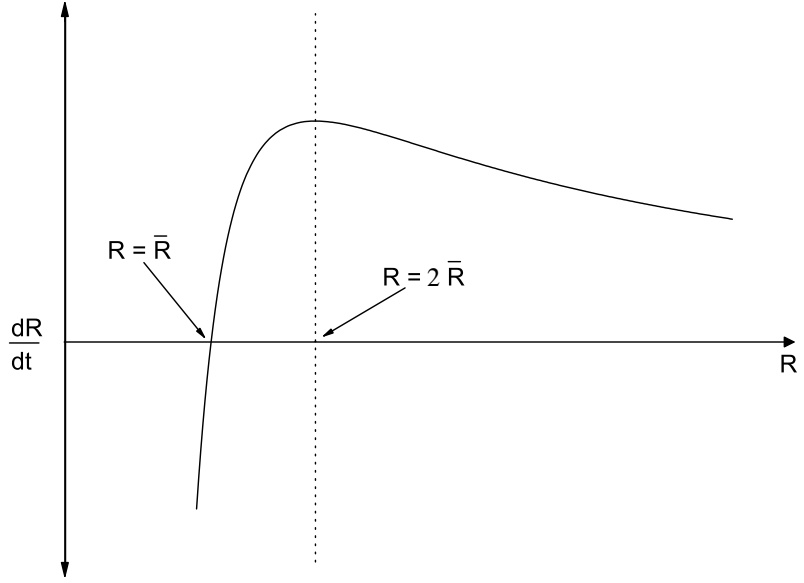


Figure 3.4: Plot of Eq. 3.15.

sizes exists in the system. It is predicted by this theory that a "quasi-steady-state" particle size distribution is approached independently of the original size distribution. The predicted distribution has a very limited range and indicates that particles larger than  $1.5 \bar{R}$  should not exist. The predicted time dependence of the mean radius is found to be

$$\bar{R}^3 = \bar{R}_0^3 + \left[ \frac{8 \bar{V}^2 \gamma CD}{9 kT} \right] t \quad (3.17)$$

where  $\bar{R}_0$  is the original mean particle size at onset of coarsening. Notice that if one substitutes  $\bar{R} = 27R/31$  into Eq. 3.15 and integrates, the result is Eq. 3.17 in terms of  $R$ .

Experimental results [49, 54] have shown that the growth of coherent particles can, in a number of cases, be described quite well by Eq. 3.17. A limiting size distribution is found, but the particle size distribution is not quite as narrow as

predicted. Li and Oriani [56] have presented modifications to the above theory for cases where the precipitate is not a pure element and not spherical.

In conclusion, it can be seen that since  $R_0$  is quite small for coherent precipitates they will coarsen their radius as the one-third of time. The average particle radius will also increase as the one-third power of the particle-matrix surface tension,  $\gamma$ , and as the one-third power of the equilibrium concentration of the precipitate atoms in the matrix phase,  $C$ . Hence, the theory predicts that coherent precipitates should coarsen more slowly than incoherent precipitates, and coarsening may be reduced by reducing the solubility of the particle atoms in the matrix.

Based on the above theories in order to form semiconductor nanocrystals in the  $\text{SiO}_2$  matrix one has to reach the supersaturation value first. The supersaturation value is controlled by the implantation dose in the case of the ion implantation. Once the supersaturation value is reached, spherical clusters of atoms form by some thermodynamic fluctuation. If a formed cluster has radius less than  $r^*$  (see Fig. 3.2), it is unstable and will shrink by losing atoms. Clusters larger than  $r^*$  have surmounted the nucleation barrier and are stable. They tend to grow larger while lowering the energy of the system during the annealing process by Ostwald ripening and the semiconductor nanocrystals are formed in the  $\text{SiO}_2$  matrix.

## CHAPTER 4

### FORMATION AND EVOLUTION OF Ge NANOCRYSTALS

#### 4.1 Introduction

In the previous chapters we discuss the formation procedure of the semiconductor nanocrystals in the SiO<sub>2</sub> matrix and the parameters which effect the formation of semiconductor nanocrystals. In this chapter we present the results of our Ge implanted SiO<sub>2</sub> samples.

The samples were investigated by EDS, SAD, SIMS, TEM and XPS. Samples for cross-sectional TEM were prepared using standard techniques. The structure of the different samples was examined at 200 keV using an analytical JEOL 2000 FX TEM and a field emission analytical JEOL 2010 F TEM equipped with a Noran Vantage DI+ EDS system. The composition of selected samples was measured using a Cameca 4F SIMS and the chemical state of elements was analyzed by XPS combined with sputtering (4 keV Ar<sup>+</sup>) in a VG Micro Lab III instrument for combining XPS with Auger Electron Spectroscopy at a residual pressure of 10<sup>-9</sup> mbar with Al K $\alpha$  radiation as excitation source. The binding energies are calibrated against the Si 2p peak from SiO<sub>2</sub> at 103.3 eV.

## 4.2 Structural Properties of Ge Implanted SiO<sub>2</sub> Films

### 4.2.1 Ge Nanocrystals

After the implantation process, samples were annealed at various temperatures and times under N<sub>2</sub> ambient to observe the formation and evolution of Ge nanocrystals. The annealing time, annealing temperature, implantation energy and dose dependence of formed Ge nanocrystals are investigated separately.

Fig. 4.1 shows TEM pictures of time evolution of sample implanted with  $1 \times 10^{17} \text{ cm}^{-2}$  <sup>74</sup>Ge at 100 keV and annealed at 1000 °C. The evolution of the Ge nanocrystals can be seen clearly. From Fig. 4.1(a), it is observed that precipitation occurs even at short annealing times. We have confirmed that the precipitates are Ge nanocrystals by SAD and EDS [57]. Fig. 4.1(a) and (b) show further that the precipitates grow in size upon increasing the annealing time. The Ge nanocrystals with well defined circular shapes are observed in the case of 30 min annealing. It is observed from these figures that by increasing annealing time, the difference between the smaller nanocrystals and larger nanocrystals increases. This is explained by the Ostwald ripening process (discussed in Chapter 3) in which the larger particles grow at the expense of the smaller ones.

For longer annealing times, Ge nanocrystals start to desolve and bright disks appear (Fig. 4.1(c) and (d)) where the Ge nanocrystal precipitates were located. These bright disks are another study and will be discussed in the next section. In addition to the bright disks a dark region near the surface also appears. This dark band is rich in Ge, as determined by EDS, and has an amorphous character

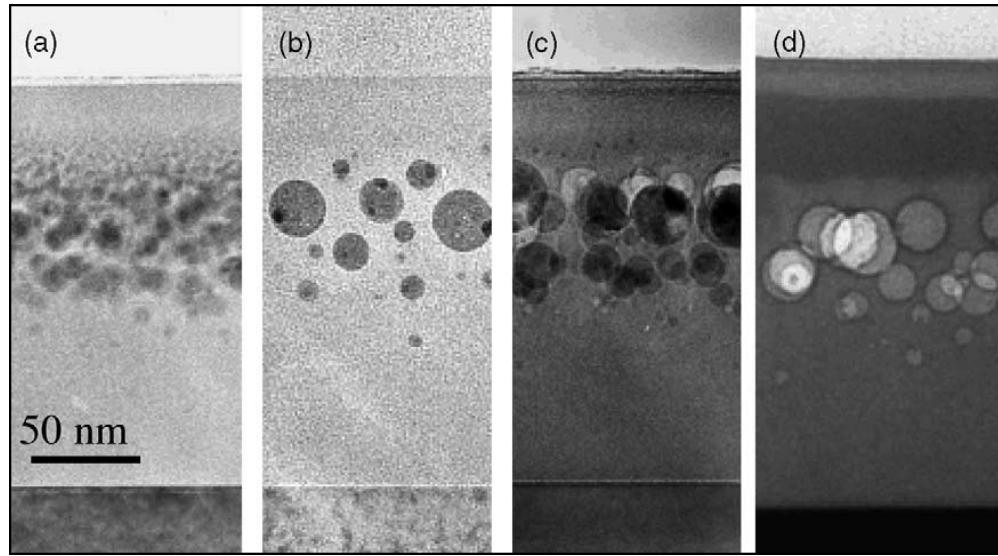


Figure 4.1: TEM cross-section of a sample which is implanted with  $^{74}\text{Ge}$  at a dose of  $1 \times 10^{17} \text{ cm}^{-2}$  at 100 keV and annealed at 1000 °C for a) 15 min b) 30 min c) 45 min d) 60 min under  $\text{N}_2$  atmosphere.

as determined by SAD. XPS from this region (as shown in Fig. 4.2(b)) indicates Ge is in an oxidized state (Traces of oxidizing species present in the annealing atmosphere can diffuse into the  $\text{SiO}_2$  films and result in the oxidation of Ge in the regions of the  $\text{SiO}_2$  films closest to the surface). This would have been observed if the dark band consisted of a SiGe-glass.

Ge nanocrystals are observed in Fig. 4.3 even at low temperatures but long annealing time for the similar sample in Fig 4.1. From Figs. 4.1(b) and 4.3(b), it is seen that annealing a Ge implanted sample at 1000 °C for 30 min gives a similar result with that of 900 °C for 60 min. This is an expected result and related with the melting temperature of bulk Ge which is discussed in Chapter 2.

By using the Figs. 4.1 and 4.3 we come up with an important result which

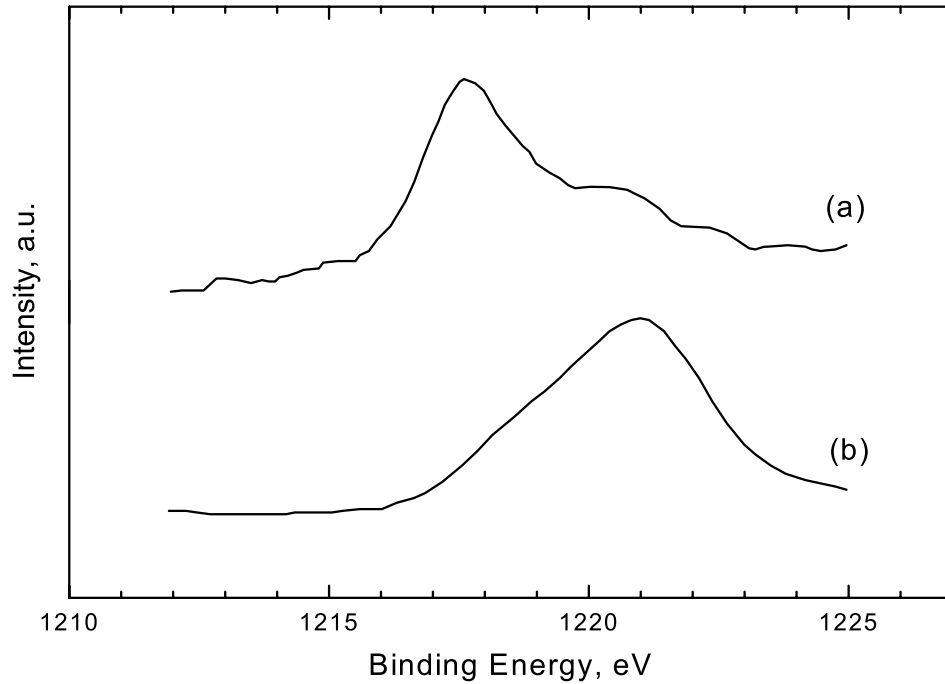


Figure 4.2: XPS spectra around  $2p_{3/2}$  peak from a sample implanted with  $1 \times 10^{17} \text{ cm}^{-2}$   $^{74}\text{Ge}$ . Both spectra are taken after sputtering in from the surface: (a) is from a sample annealed for 15 min at  $1000 \text{ }^\circ\text{C}$  and is interpreted as arising from a region with Ge crystalline precipitates, (b) from a sample annealed for 1 h at  $1000 \text{ }^\circ\text{C}$  and is interpreted as coming from a region with Ge in an oxidized state probably a SiGe glass. Note that the tabulated binding energies of Ge and  $\text{GeO}_2$  around  $2p_{3/2}$  peak are 1217 and 1220 eV, respectively.

we discussed in Chapter 2: The annealing time, annealing temperature and atmosphere are very important parameters for the evolution of semiconductor nanocrystals. It is understood clearly from these figures that there is a critical annealing time for a fix annealing temperature or viceversa for the formation of Ge nanocrystals. Disappearing of Ge nanocrystals at  $1000 \text{ }^\circ\text{C}$  might be expected as the melting temperature of bulk Ge is  $938 \text{ }^\circ\text{C}$ . Above the melting temperature the Ge nanocrystals are dissolved and Ge accumulates towards the surface and Si/SiO<sub>2</sub> interface as seen in the Fig. 4.4.

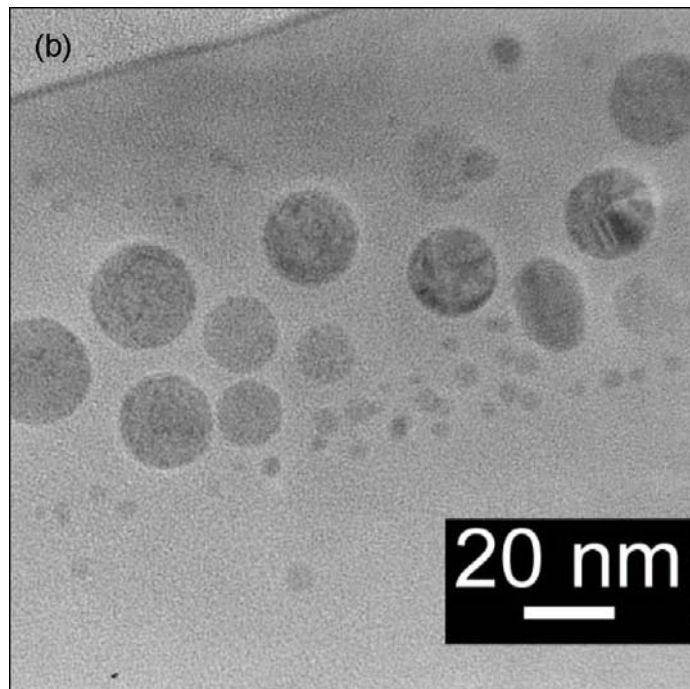
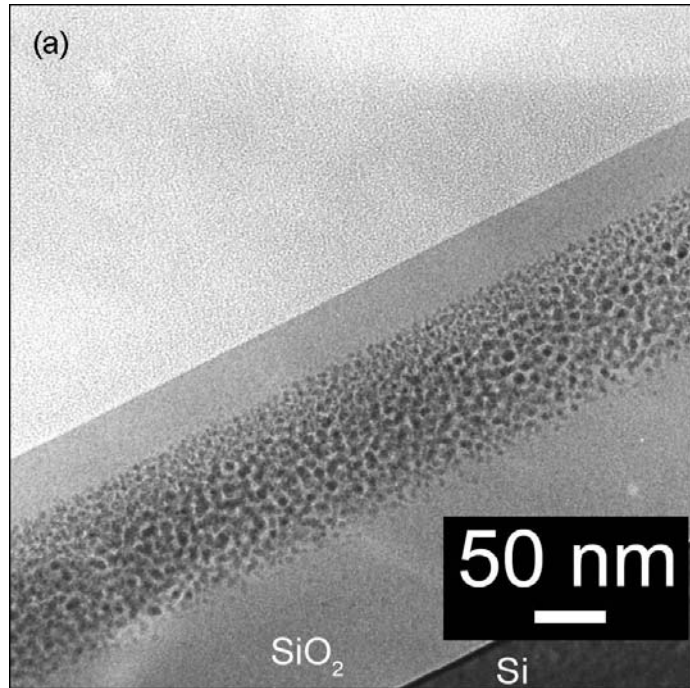


Figure 4.3: TEM cross-section of a sample which is implanted with  $^{74}\text{Ge}$  at a dose of  $1 \times 10^{17} \text{ cm}^{-2}$  at 100 keV and annealed at (a) 800 °C and (b) 900 °C for 60 min under  $\text{N}_2$  atmosphere.

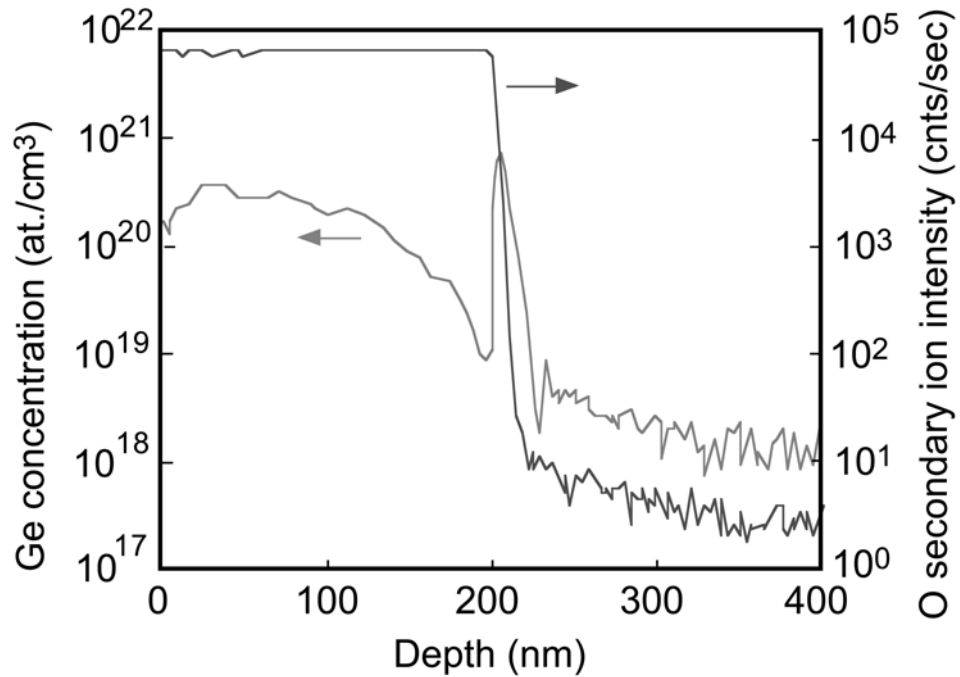


Figure 4.4: SIMS depth profile of a SiO<sub>2</sub> layer implanted with a dose of  $7 \times 10^{15}$  cm<sup>-2</sup> at 100 keV and annealed at 1050 °C for 45 min under N<sub>2</sub> atmosphere.

The features observed in 4.1 can be interpreted as the effect of annealing ambient. Trace amount of O<sub>2</sub> in the N<sub>2</sub> gas causes Ge atoms to oxidized. This behavior was confirmed by others, as well [58]. As it is very hard to control the O<sub>2</sub> amount in the flowing gas, one should be very careful when drawing general conclusion on the formation of Ge nanocrystals. Variations between experiments and laboratories might be expected.

In addition to the annealing time and temperature, it is observed that the implantation dose is also important for the formation of semiconductor nanocrystals.

Fig. 4.5 shows a high resolution TEM picture of a comparably lower dose ( $3 \times 10^{16}$

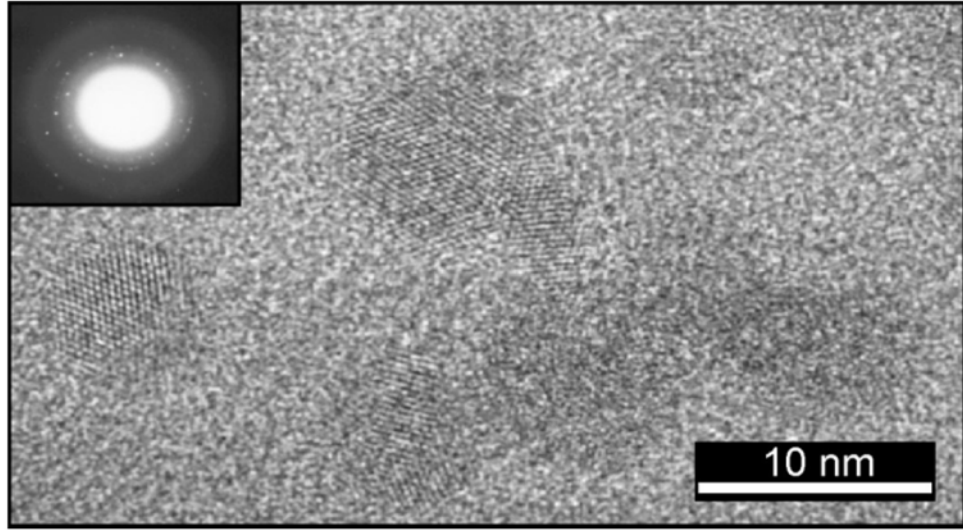


Figure 4.5: TEM cross-section of a sample which is implanted with  $^{74}\text{Ge}$  at a dose of  $3 \times 10^{16} \text{ cm}^{-2}$  at 100 keV and annealed at 800 °C for 60 min under  $\text{N}_2$  atmosphere. Lattice fringes and spots in the corresponding diffraction pattern (inset) provide evidence of crystallinity.

$\text{cm}^{-2}$ ) than that of the sample in Fig. 4.3 with the corresponding diffraction pattern. One can clearly see lattice fringes in the picture and spots in the diffraction pattern, which are both evidences of crystallinity. Comparison of Figs. 4.5 and 4.3(a) shows us clearly that the average nanocrystal size is an increasing function of implantation dose.

We observed Ge nanocrystals at a minimum dose of  $3 \times 10^{16} \text{ cm}^{-2}$ . For the samples implanted with a dose of  $2 \times 10^{15} \text{ cm}^{-2}$ ,  $7 \times 10^{15} \text{ cm}^{-2}$  and  $1 \times 10^{16} \text{ cm}^{-2}$  we could not observe Ge nanocrystal formation.

The last parameter which will effect the formation of nanocrystals is the implantation energy. In order to investigate the relationship between the implantation energy and the formation of nanocrystals we have implanted our samples

with an energy of either 30 or 100 keV. At 30 and 100 keV the projected ranges for the Ge distributions are approximately 26 and 70 nm, respectively. For the low energy implantations since the projected range is closer to the surface Ge is comparatively more prone to oxidation by diffusing species from the surface during the annealing process. For the samples implanted at an energy of 30 keV no precipitates were observed.

In conclusion, in order to form Ge nanocrystals in the SiO<sub>2</sub> matrix there are important parameters as mentioned above that should be taken into account. By changing these parameters it is possible to control the sizes, numbers and positions of Ge nanocrystals in the SiO<sub>2</sub> matrix.

#### 4.2.2 Voids

Up to now, the formation mechanism of Ge nanocrystals and its dependence on the processing parameters were discussed. In this section we attempt to clarify the possible reasons for the formation of bright disks (attributed to voids) observed in the samples annealed at higher temperatures and in the samples with a projected range closer to surface.

It is well known phenomenon that ion implantation causes the formation of cavities in crystalline materials [59, 60]. Such cavities have been divided into two groups, namely voids and bubbles. Bubbles are gas filled cavities which are formed after implanting materials with inert gases. Voids are empty cavities and are formed by vacancy clustering. During ion implantation damage is introduced into the material. Both vacancies and interstitials are generated. Voids can form

when more vacancies than interstitials arrive at the void surface. In crystalline materials dislocations are suggested to act as a stronger sink for interstitial atoms than for vacancies, resulting in a higher concentration of vacancies than that of interstitials, which again favor growth of voids when these point defects are mobile [59]. Bubbles can be considered to be more closely related to voids than they are related to other precipitates since the binding energy between the constituents of the cavity is small (if any) in the former case.

It is clearly observed from Fig. 4.1 that the bright disks are appeared for long annealing times (45 and 60 min). Especially, Fig. 4.1(c) is of interest because of constituting both Ge nanocrystals and bright disks. For 45 min annealing it is observed that the Ge nanocrystals begin to dissolve and Ge will diffuse away from the nanocrystals towards the surface region, leaving their positions to bright disks. From Fig. 4.1(d), it is seen that the Ge nanocrystals dissolve completely and a dark band near the surface emerges. Same feature was observed for the samples implanted with lower dose of  $3 \times 10^{16} \text{ cm}^{-2}$  (see Fig. 4.6). We pointed out in the previous section that this band is in the form of SiGe-glass. It is important to note that for the diffusion of Ge from Ge precipitates to the surface there should be a driving force. At 1000 °C the Ge precipitate is expected to be in the liquid state since this temperature is higher than the melting temperature of bulk Ge. Hence, it could be acceptable to suggest that the driving force arises from the free energy change of Ge in the liquid and Ge in the SiGe-glass network (the oxide bond is stronger than that of Ge-Ge (see Appendix B)).

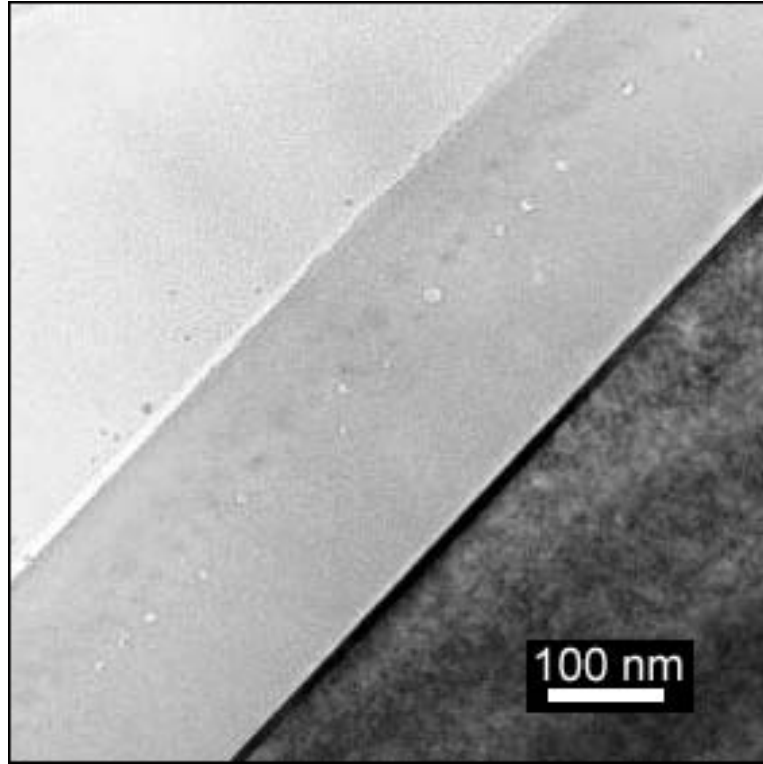


Figure 4.6: TEM cross-section of a sample which is implanted with  $^{74}\text{Ge}$  at a dose of  $3 \times 10^{16} \text{ cm}^{-2}$  at 100 keV and annealed at 1000 °C for 60 min under  $\text{N}_2$  atmosphere.

Actually, the direct evidence from Fig. 4.1 is not sufficient to identify the bright disks as voids. The bright disks observed from this picture corresponds to areas of less electron scattering than the surroundings. This reduced scattering could be due to a material of lighter average atomic number or areas of thinner effective sample thickness than the surroundings. These features could be associated with segregation of light elements or void formation.

It is observed by SIMS that the as-implanted sample contains excess H and F atoms. The origin of F in the samples is from contamination of the beam during

ion implantation.  $\text{GeF}_4$  was used as the gas source as mentioned in Chapter 2 and  $\text{F}_4^+$  molecules can evidently be implanted simultaneously with  $^{74}\text{Ge}^+$ . The excess H could partly arise from the implantation or could be due to an increased uptake of H or water vapor by the heavily damaged oxide network which has been suggested by Schmidt et al [61]. Therefore, the possibility of bright disks to be gas bubbles containing H or F should be taken into account. In order to clarify this, annealed samples, at 1000 °C, analyzed by SIMS again and it was observed that the SIMS signals of F and H are practically absent in the  $\text{SiO}_2$  matrix. This indicates that F and H have diffused out of the  $\text{SiO}_2$  matrix. This observation further supports the assumption of bright disks being voids but only together with some other results.

Another interesting feature of samples, containing bright disks, were observed when they were exposed to intense electron beam radiation. In Fig 4.7 it is seen that the bright disks are gradually filled by the surrounding material during the exposure and darker micro-regions appear in the Ge-rich layer. The migration of O, Si and Ge in Ge implanted  $\text{SiO}_2$  films induced by intense electron beam irradiation in a TEM has previously been reported [62, 63, 64]. Given sufficient energy to mobilize the atoms in the network, Si-Ge glass will segregate into a Si rich and Ge rich oxide, respectively. It should be noted that this is a well known phenomenon. SiGe glass is commonly used in fiber optics, and this segregation is used to write gratings in the glass or the fiber. The segregation can be induced by energetic photons [65] or by electrons [64].

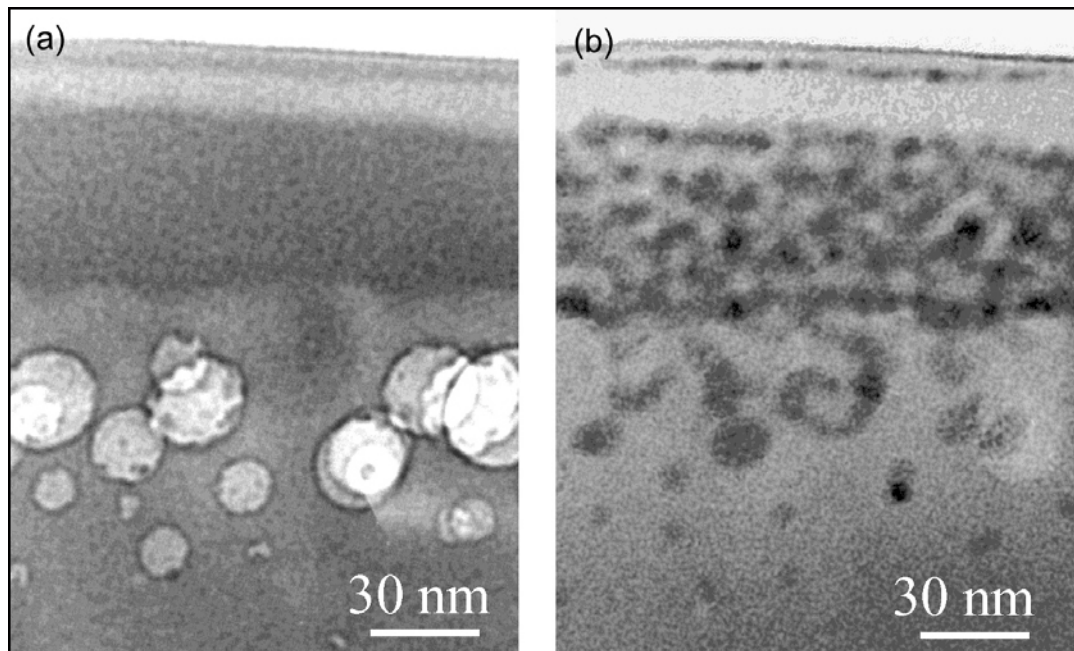


Figure 4.7: TEM cross-section of a sample which is implanted with  $^{74}\text{Ge}$  at a dose of  $1 \times 10^{17} \text{ cm}^{-2}$  at 100 keV and annealed at 1000 °C for 60 min under  $\text{N}_2$  atmosphere: (a) before intense electron beam irradiation and (b) after intense electron beam irradiation.

In the light of the above results, we conclude that the observed disks are voids not gas bubbles.

## CHAPTER 5

### RAMAN ANALYSIS OF Ge NANOCRYSTALS

#### 5.1 Introduction

The characterization of nanocrystals is an important metrological issue due to the difficulties in the measurement of small quantities with nanometric dimension. Diagnostic techniques such as TEM or XRD, should have high resolution capabilities for a detailed observation. PL, which is most widely used characterization technique, does not provide unambiguous results in some cases as it may result from other luminescent centers, such as defects in the host matrix, rather than quantum size effects. Raman spectroscopy is a powerful and non-destructive technique in the analysis of solid chemical structures. In particular, it provides fingerprint evidence for the formation of Ge-Ge bonds, and hence nanocrystals in a host matrix such as SiO<sub>2</sub>. In addition to the qualitative information about the chemical structure, Raman spectroscopy has been shown to be useful in determining the size of the nanocrystals [66]. This approach relies on a theoretical model, which relates the peak widening and peak shift to the size of the nanocrystals. In addition, the size distribution of nanocrystals, which is an important issue in the case of ion implantation, can be estimated by fitting the theoretical function to the asymmetry in the Raman peak resulting from the variations in the sizes

of the nanocrystals [67].

In this chapter, we report on the characterization of Ge nanocrystals embedded in a SiO<sub>2</sub> matrix by Raman analysis. The size and size distribution of Ge nanocrystals were both estimated by a theoretical analysis based on the phonon confinement model. Theoretical calculations were compared with the experimental results of Raman spectrometry. A comparison was made with the TEM analysis in order to verify the estimations deduced from the theoretical calculations.

## 5.2 Size Determination of Ge Nanocrystals by Raman Line Profile Analysis

### 5.2.1 Experimental Procedures

SiO<sub>2</sub> films implanted with <sup>74</sup>Ge ions with doses of 3x10<sup>16</sup> cm<sup>-2</sup> and 1x10<sup>17</sup> cm<sup>-2</sup> at an energy of 100 keV were used in this study. Implanted films were processed with annealing temperature ( $T_a$ ) of 700, 900 and 1050 °C and an annealing time ( $t_a$ ) of 45 min under N<sub>2</sub> ambient.

Raman scattering spectra of the films were obtained before and after annealing, in back-scattering configuration with a Renishaw RM series Raman microscope using a 514.5 nm Ar<sup>+</sup> laser excitation source. All of the measurements were carried out at room temperature, using a total laser power of either 4 or 0.4 mW (on the sample). The beam diameter was 1 μm on the sample surface and scattered light was collected with a CCD camera on the head of the microscope. The spectral resolution was 1 cm<sup>-1</sup>.

### 5.2.2 Theoretical Model

For semiconductor nanocrystals, spatial confinement of phonons in a finite volume (on the order of a few hundred angstroms [68]) is expected to partially relax the wave vector selection rules and hence cause modifications in the bulk Raman peak such as peak-frequency shifting, peak broadening, and emergence in peak asymmetry [66, 69, 70, 71]. The reason for these alterations is the partial breakdown of the  $\mathbf{q} = 0$  selection rule due to the spatial confinement of the phonons in a finite volume [72, 73]. A phonon can no longer be described by a plane wave, as it is for the bulk crystal, but instead by a wave packet spatially confined inside the nanocrystal. A finite particle size  $L$  would bring about an uncertainty in wavevector on the order of  $\pm 2\pi/L$ , which will be larger for smaller crystal sizes. In an infinite (bulk) crystal, uncertainty is 0, and as only the phonons near the zone center can contribute to the first-order Raman spectrum, the Raman peak will be rather sharp. If the phonon dispersion curves are not flat near  $\mathbf{q} = 0$ , then, for nanocrystals, the spectral features will shift, broaden, and become asymmetric by the phonon confinement.

To calculate the mean size of the spherical Ge nanocrystals formed in the  $\text{SiO}_2$  matrix by ion implantation, the phonon confinement model developed by Santos and Torriani [67] was employed. The spherical shape of nanocrystals was confirmed by TEM (see Fig. 4.3(b)). The Raman spectrum at frequency  $\omega$ ,  $I(\omega)$ , for nanocrystals developed by Santos and Torriani can be written as

$$I(\omega) = \int_0^\infty P(L)dL I_L(\omega) \quad (5.1)$$

where  $I_L(\omega)$  is the Raman spectrum without size distribution function and  $P(L)$  is a size distribution function with mean value  $\bar{L}$  and standard deviation  $\sigma$ . Assuming  $P(L)$  to be a Gaussian function, the integral above can be solved with the result [67]:

$$I(w)\alpha \int_0^{2\pi/a} q^2 dq f(q) e^{-(q\bar{L}f(q)/4\pi)^2} C(w, q) \quad (5.2)$$

where

$$f(q) \equiv (1 + \sigma^2 q^2 / 8\pi^2)^{-\frac{1}{2}}, \quad (5.3)$$

$$C(w, q) = \int_{-\infty}^{\infty} \frac{\Gamma/\pi}{(w - w\mu(q) - x)^2 + \Gamma^2} T(x) dx, \quad (5.4)$$

and

$$T(x) = \begin{cases} (2\Gamma_s - |x|)/4\Gamma_s^2 & \text{for } |x| \leq 2\Gamma_s \\ 0 & \end{cases} \quad (5.5)$$

Here,  $\Gamma$  is the natural (bulk) linewidth ( $\approx 3.5 \text{ cm}^{-1}$ ),  $w\mu(q) = A + B\cos(qa/2)$  is the optical phonon dispersion relation with  $A = 288.30 \text{ cm}^{-1}$  and  $B = 12.01 \text{ cm}^{-1}$  and  $a$  is the lattice parameter where  $a_{Ge} = 0.565 \text{ nm}$ .  $T(x)$  is the triangular instrumental transfer function with a FWHM,  $\Gamma_s$  ( $= 1 \text{ cm}^{-1}$  for our experimental conditions).

### 5.2.3 Results and Discussion

Figures 5.1(a) and 5.1(b) display the calculated peak frequency and linewidth of Raman spectra as a function of mean crystallite size ( $\bar{L}$ ) using the experimental bulk value  $3.5 \text{ cm}^{-1}$  as the natural linewidth ( $\Gamma$ ) and  $a_{Ge} = 0.565 \text{ nm}$  as the Ge lattice constant. As seen from both curves, significant changes to the Raman spectra must become observable below a critical diameter of about 20 nm.

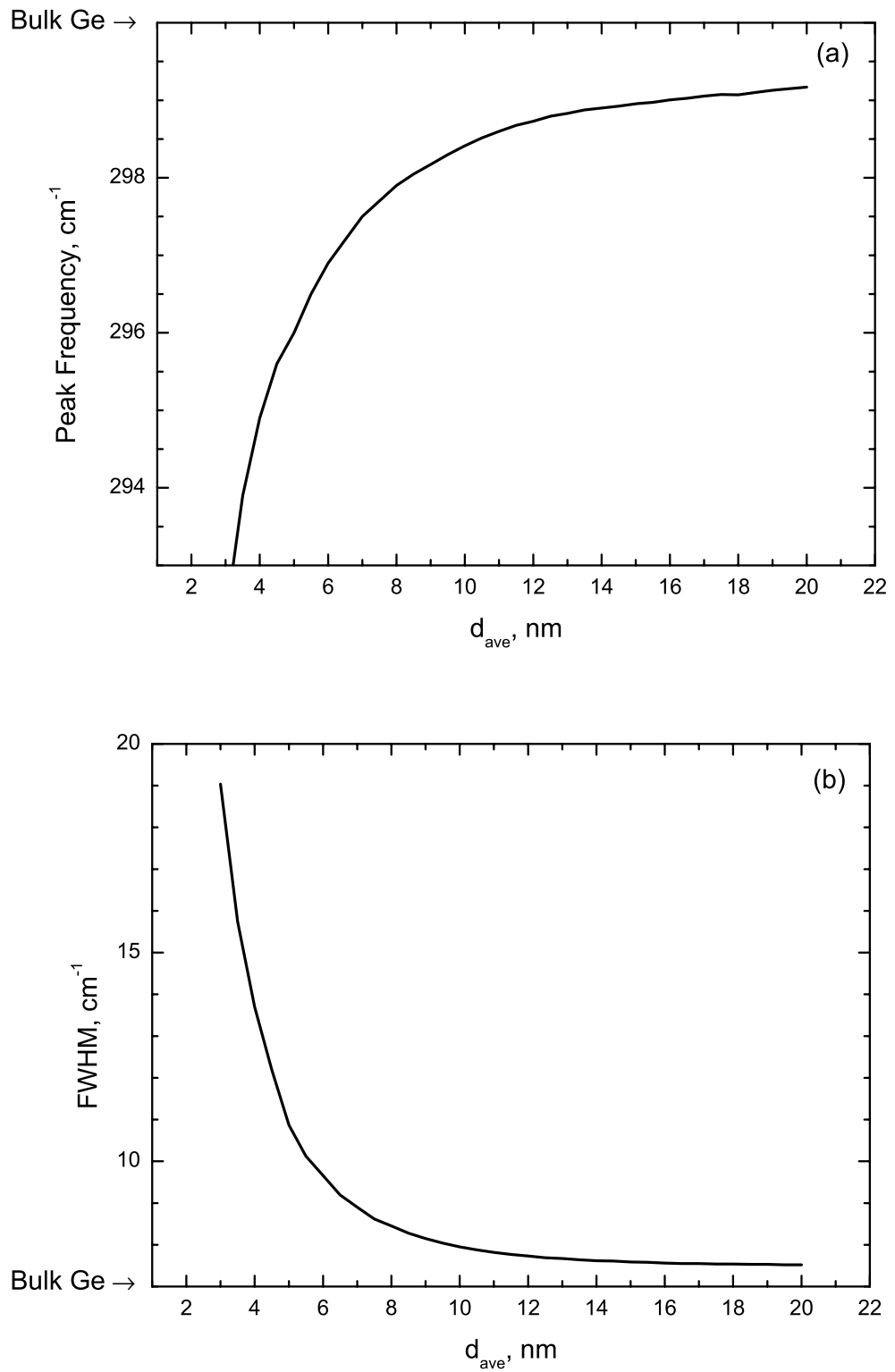


Figure 5.1: The calculated (a) peak frequency and (b) linewidth (FWHM) as a function of Ge crystal size ( $d_{ave}$ ). Corresponding bulk Ge values are indicated.

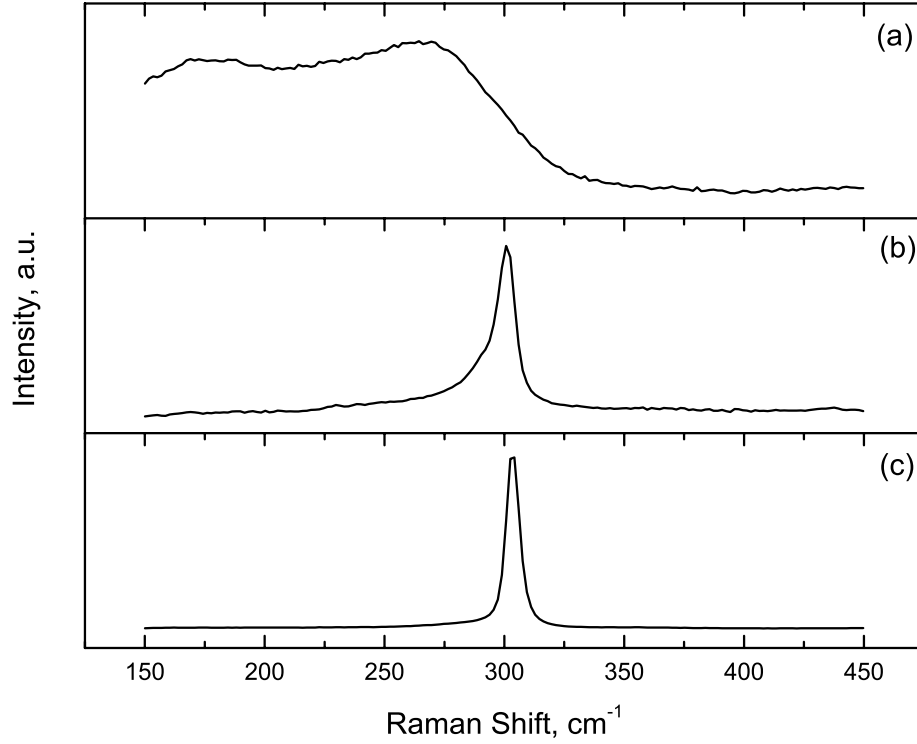


Figure 5.2: Raman spectra for a  $1 \times 10^{17} \text{ cm}^{-2}$   $^{74}\text{Ge}$ -implanted  $\text{SiO}_2$  film (a) before and (b) after annealing (at  $900 \text{ }^\circ\text{C}$  for 45 min under  $\text{N}_2$  atmosphere) and (c) bulk Ge.

Therefore, it is expected for stress-free Ge nanocrystals that as  $\bar{L}$  decreases the peak frequency should shift to lower frequency (i.e. redshift), while the linewidth of the peak increases for  $\bar{L} < 20 \text{ nm}$ .

Figure 5.2 shows the Raman spectra of the film implanted with  $1 \times 10^{17} \text{ cm}^{-2}$   $^{74}\text{Ge}$ . The annealed film in this figure is similar to the one for which the TEM image was given in Fig. 4.3(b), except that  $t_a$  was 15 min longer for the TEM sample. The Raman spectrum of the as-implanted film (Fig. 5.2(a)) is similar to that of amorphous-Ge [74, 75]. In the case of disordered semiconductors, such as amorphous and nanocrystalline, the  $\mathbf{q} = 0$  selection rule that determines the

Raman spectra of the bulk crystals is either fully or partially violated (relaxed) so that phonons other than the zone-centered phonons can also be observed in their Raman spectra. On the other hand, the spectrum of the annealed film exhibits a sharp peak near  $300\text{ cm}^{-1}$ , indicating the crystallization of Ge in the film. The width and spectral shape of this peak are different from those of bulk Ge but similar to those of nanocrystalline Ge [76, 77]. In these measurements, the zone-centered Ge optical phonons peaked at  $303.3\text{ cm}^{-1}$  with a FWHM of  $7.0\text{ cm}^{-1}$  in the spectrum of bulk Ge (Fig. 5.2(c)); whereas the peak in the spectrum of nanocrystalline Ge (Fig. 5.2(b)) is downshifted to  $301.5\text{ cm}^{-1}$  and asymmetrically broadened towards the lower frequency with respect to the bulk Ge peak.

It should also be noted that silicon, which was used as the substrate material in this study, also possesses a peak near  $300\text{ cm}^{-1}$  and two weaker features at  $229$  and  $435\text{ cm}^{-1}$  (besides the main peak at  $520\text{ cm}^{-1}$ ) in its Raman spectrum. Kolobov et al. [78] argued that most studies on the Raman scattering from Ge nanostructures grown on Si substrates have actually reached incorrect conclusions by totally ignoring this point and attributed this peak to the formation of Ge nanocrystals. Moreover, it is discussed in Chapter 4 that some of the Ge atoms are segregated on to the Si substrate and forms a Ge rich layer at the  $\text{SiO}_2/\text{Si}$  interface. This Ge rich layer might also contribute to the observed Raman spectrum. In order to eliminate the scattering signal both from the Si substrate and from the Ge rich layer at the interface, Raman spectra were acquired before and after removing the  $\text{SiO}_2$  layer by wet etching in diluted HF. As shown in Fig. 5.3, Raman spectrum

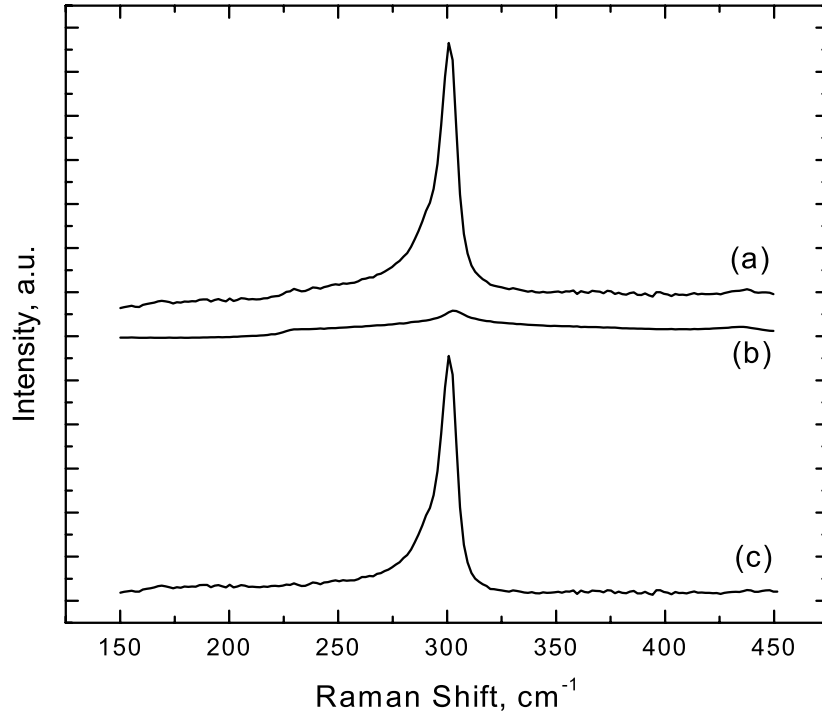


Figure 5.3: Raman spectra for a  $\text{SiO}_2$  film implanted with  $1 \times 10^{17} \text{ cm}^{-2} \text{ } ^{74}\text{Ge}$  and (a) annealed at  $900 \text{ } ^\circ\text{C}$  (b) after etching in HF and (c) the difference between curves a and b.

of the etched sample (Fig. 5.3(b)) was subtracted from that of nanocrystalline Ge (Fig. 5.3(a)). As can be seen from the difference of the two spectra (Fig. 5.3(c)), the contribution of the scattering from the substrate is almost negligible. From these we can conclude that the Ge nanocrystals inside the oxide is the main source for the observed Raman peak at around  $300 \text{ cm}^{-1}$ .

For the background-subtracted optical phonon peak in Fig. 5.2(b), a lineshape fit is made in Fig. 5.4. As seen in this figure, a successful fit was obtained for  $\bar{L} = 8.7 \text{ nm}$  and  $\sigma = 2.1 \text{ nm}$ . When compared with the TEM picture of the nanocrystals grown in a similar sample (e.g. Fig. 4.5), it is observed that this value (8.7 nm)

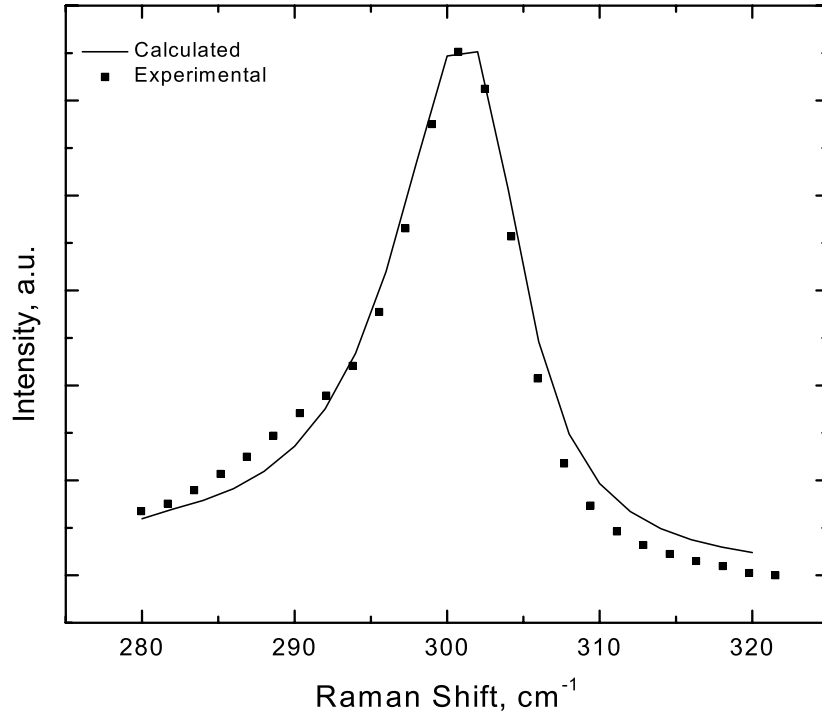


Figure 5.4: Experimental background-subtracted Raman spectrum of Ge nanocrystals compared to theoretical Raman spectrum calculated for  $\bar{L} = 8.7$  nm and  $\sigma = 2.1$  nm using a phonon confinement model.

falls into the size range obtained directly from the TEM picture. The size of the crystal islands can be determined from the TEM pictures even though the actual size might be larger than the apparent size which depends on where the nanocrystals are cut during the preparation of cross-sectional sample. Bearing this uncertainty in mind, the nanocrystals size is estimated to vary in the range of 2-25 nm. It is seen from the TEM picture that these nanocrystals fall into two groups: group1 with small nanocrystals having an average grain size of 4 nm and group 2 constituting large nanocrystals with an average grain size of 20 nm. This can be understood by considering the growth and coarsening theory (see Chapter

3) according to which some nanocrystals grow while the others shrink. Keeping in mind that the Raman spectra changes drastically when the mean crystallite size is below 20 nm we can conclude that the effect of group 2 nanocrystals (with  $\bar{L} = 20$  nm) on the asymmetry of the Raman spectra is small. This was confirmed by using multiple size distribution functions in our calculations. In addition, we expect group 1 nanocrystals (with  $\bar{L} = 4$  nm) to be larger and group 2 nanocrystals to be smaller with respect to the sizes measured from the TEM image, since the annealing time was 15 min shorter for the Raman samples. We can thus confidently conclude that the average size of 8.7 nm calculated from the Raman spectrum is a good estimate of the average size of the nanocrystals. For the respective crystal size the peak frequency of the Raman peak is expected to redshift by  $2 \text{ cm}^{-1}$  from the corresponding bulk value ( $300.0 \text{ cm}^{-1}$ ). This shift is about  $1.8 \text{ cm}^{-1}$  in the case of experimental spectra. Although the experimental resolution was  $1 \text{ cm}^{-1}$ , the small difference in the expected value of the redshift can be, alternatively, due to a compressive stress on the nanocrystals; compressive stress is well known to cause the Raman spectrum to blueshift (e.g. [79]). Fujii et al. prepared Ge nanocrystals embedded in  $\text{SiO}_2$  matrices by annealing co-sputtered Ge- $\text{SiO}_2$  films and studied the size dependence of their Raman spectra [76, 77]. They reported that, despite the fact that the linewidth broadens as the average crystal size decreases (from 15 to 6.1 nm) in good agreement with the expectations (i.e. with their phonon confinement model), the peak frequency did not shift appreciably (even a small blueshift was observed for the smaller sizes). They attributed the latter effect to a compressive stress exerted on the

Ge nanocrystals by the surrounding SiO<sub>2</sub> medium. Since the nearest-neighbor distances are 0.24 nm and 0.16 nm for Ge and SiO<sub>2</sub>, respectively, it is considered that the lattice mismatch yields a compressive stress on the Ge nanocrystals [66, 76, 77].

Figure 5.5 gives the Raman spectra of the films implanted with  $3 \times 10^{16} \text{ cm}^{-2}$  <sup>74</sup>Ge before and after annealing (for  $T_a = 700, 900, 1050 \text{ }^\circ\text{C}$ ). The spectrum of the as-implanted film is similar to that in Fig. 5.2(a) and shows that the Ge in the film is in an amorphous phase. The Raman spectra for all of the annealed films, on the other hand, are characterized by a peak near the optical phonon mode of crystalline Ge, i.e.  $300 \text{ cm}^{-1}$ , indicating the crystallization of Ge and formation of nanoparticles. By fitting of the Ge peak around  $300 \text{ cm}^{-1}$  with calculated Raman spectra appropriate to their lineshapes, we estimate the  $\bar{L}$  as 5.0, 5.4, 6.0 nm and  $\sigma$  as 1.1, 1.2, 1.6 nm in the films annealed at 700, 900 and 1050  $^\circ\text{C}$  for 45 min, respectively (the corresponding FWHM values are 13.8, 12.8 and 12.1  $\text{cm}^{-1}$ ). It is not surprising that the  $\bar{L}$  increases with the annealing temperature. It is expected that the peak frequency should redshift from the corresponding bulk value by 4.0, 3.6 and 3.1  $\text{cm}^{-1}$  for the films annealed at 700, 900 and 1050  $^\circ\text{C}$ , respectively. In fact, as the  $\bar{L}$  (or annealing temperature) decreases the peak slowly blueshifts: the peak frequency is 302.9, 303.6, and 304.4  $\text{cm}^{-1}$  for the films with  $T_a = 1050, 900,$  and  $700 \text{ }^\circ\text{C}$ , respectively (the measured bulk value is 303.3  $\text{cm}^{-1}$ ). This observation is in line with the report of Fujii et al. [76, 77], adding more weight to the proposal that a compressive stress is exerted onto the Ge

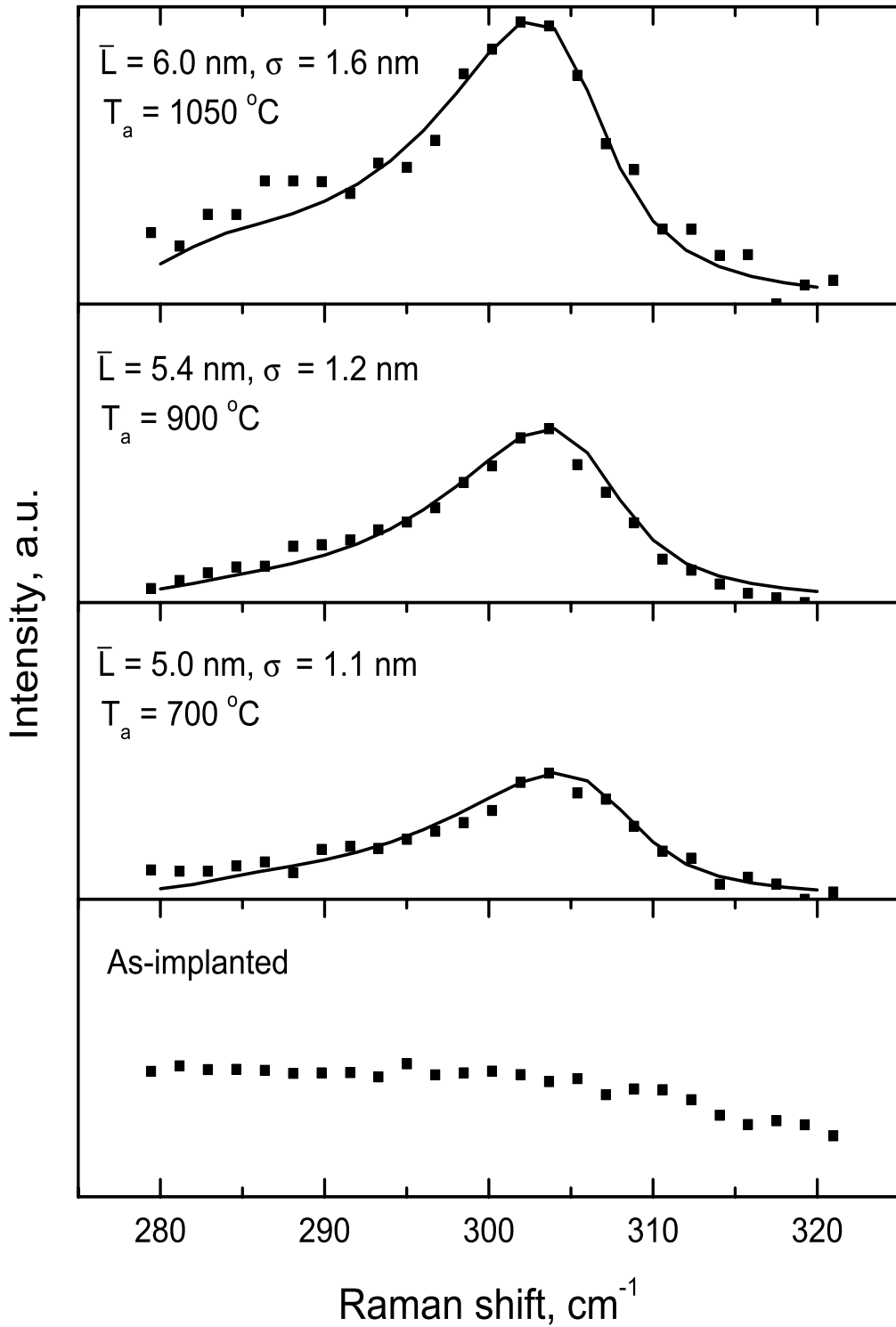


Figure 5.5: Raman spectra for the films implanted with  $3 \times 10^{16} \text{ cm}^{-2} \text{ }^{74}\text{Ge}$ . The spectrum of the as-implanted film is amorphous Ge-like. The crystalline Ge peaks in the spectrum of annealed films (squares) are fitted using a phonon confinement model considering spherical nanocrystals (solid lines). Calculated  $\bar{L}$ , and annealing temperatures are indicated near the theoretical curves.

Table 5.1: Summary of the  $\bar{L}$ , experimental and theoretical peak frequency shift (PFS) and corresponding FWHM values. For experimental and theoretical PFS, 303.3 and 300.0  $\text{cm}^{-1}$  were used as the bulk Ge value, respectively.

Parameter	Dose: $3 \times 10^{16} \text{ cm}^{-2}$			Dose: $1 \times 10^{17} \text{ cm}^{-2}$
	700 °C	900 °C	1050 °C	900 °C
$L$ , nm	5.0	5.4	6.0	8.7
Experimental PFS, $\text{cm}^{-1}$	+ 1.1	+ 0.3	- 0.4	- 1.8
Theoretical PFS, $\text{cm}^{-1}$	- 4.0	- 3.6	- 3.1	- 2.0
Experimental FWHM, $\text{cm}^{-1}$	13.8	12.8	12.1	9.5
Theoretical FWHM, $\text{cm}^{-1}$	10.9	10.2	9.7	8.2

nanocrystals by the surrounding oxide. The summary of the obtained parameters can be seen in Table 5.1.

Another interesting feature in the Raman results shown in Fig. 5.5 is the emergence of a shoulder peak at around 288  $\text{cm}^{-1}$  in samples annealed at 900 and 1050 °C. Similar Raman peaks were observed by Kolobov et al. [78] and attributed to “Ge related compounds”. This peak could also result from the oxidation of Ge nanocrystals. It was mentioned in Chapter 4 that Ge atoms leave their positions and oxidize at high temperatures forming a band of  $\text{GeO}_x$  layer. The oxidation of Ge causes nanocrystals to shrink and presumably changes the stress profile in them. As discussed above, a decrease in the nanocrystals size with a decrease in the amount of stress would generate a shift to lower wave number values.

## CHAPTER 6

### PL SPECTROSCOPY OF Si NANOCRYSTALS

#### 6.1 Introduction

The observation of PL from the semiconductor nanocrystals embedded into the SiO<sub>2</sub> matrix has drawn much attention in recent years because of its promising solution for the fabrication of Si-based LEDs. With this motivation many studies have been reported recently on the PL from Si nanocrystals embedded in SiO<sub>2</sub> matrix. In these studies, two PL spectral regions, 400-670 and 670-1000 nm, have been prominent [80-93]. The former is attributed to the defects which is formed in the SiO<sub>2</sub> matrix while the latter is attributed to the electron-hole recombination in the semiconductor nanocrystals. Especially, the region 670-1000 nm is important because the PL signal obtained in this region is tunable by the nanocrystal size, which is quite desirable for device production.

In this chapter, we present a study of the PL emitted from Si nanocrystals formed by ion implantation technique and post annealing. The experimental results support the conclusion that the classical quantum confinement effect can be a reasonable model for explaining the PL from the Si nanocrystals.

## 6.2 PL Spectroscopy

PL spectroscopy is a contactless, nondestructive method of measuring light emission and then probing the electronic structure of materials. Specifically, light is directed onto a sample, where it is absorbed and imparts excess energy into the material in a process called “photo-excitation”. One way this excess energy can be dissipated by the sample is through the emission of light, or luminescence. In the case of photo-excitation, this luminescence is called PL. The intensity and spectral content of this PL is a direct measure of various important material properties.

More specifically, photo-excitation causes electrons within the material to move into permissible excited states. When these electrons return to their equilibrium states, the excess energy is released through the emission of light (a radiative process) or through collision with lattice atoms (a nonradiative process). The energy of the emitted light or PL is related to the difference in energy levels between the two electron states involved in the transition that is, between the excited and the equilibrium states. The quantity of the emitted light is related to the relative contribution of the radiative process.

PL Applications:

- Band gap determination. The most common radiative transition in semiconductors is between states in the conduction and valence bands, with the energy difference being known as the band gap. Band gap determination is particularly useful when working with new compound semiconductors.

- Impurity levels and defect detection. Radiative transitions in semiconductors also involve localized defect levels. The PL energy associated with these levels can be used to identify specific defects and the amount of PL can be used to determine their concentration.
- Recombination mechanisms. As discussed above, the return to equilibrium, also known as “recombination”, can involve both radiative and non-radiative processes. The amount of PL and its dependence on the level of photo-excitation and temperature are directly related to the dominant recombination process. Analysis of PL helps to understand the underlying physics of the recombination mechanism.
- Material quality. In general, non-radiative processes are associated with localized defect levels, whose presence is detrimental to material quality and subsequent device performance. Thus, material quality can be measured by quantifying the amount of radiative recombination.

Special Features:

- Various excitation wavelengths allow for varying penetration depths into the material, and thus, varying levels of volume excitation.
- Detection of PL from 0.4 to 2.8  $\mu\text{m}$  using diffraction and Fourier-transform-based systems.
- Sample temperatures of 4 to 300 K.

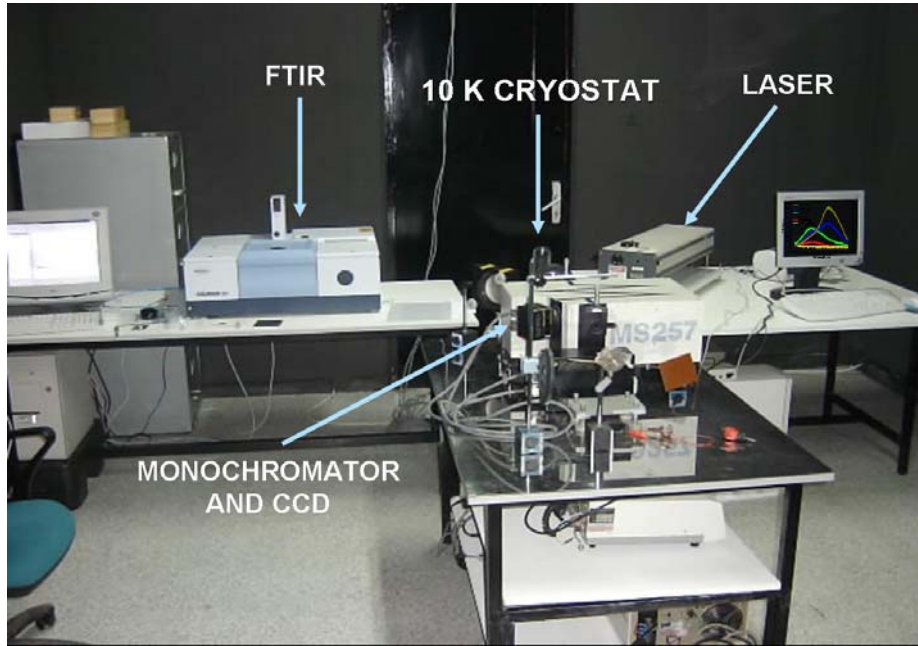


Figure 6.1: PL setup consisting of a laser, monochromator, CCD and cryostat.

In order to observe PL from our Si implanted samples we used an experimental set-up (see Fig. 6.1) consisting of an excitation source, MS-257 type monochromator, Hamamatsu CCD camera and closed-cycle He cryostat. In our PL experiments, 532 nm NdYag, 337 nm N<sub>2</sub> laser or 1000 W Hg-Xe arc lamp was used as an excitation source. NdYag laser is a continuous laser with a maximum power of 3 W while N<sub>2</sub> laser is a pulse laser with an average power of 7 mW. By using the cryostat it is possible to carry out temperature dependent PL experiments between 10 - 300 K.

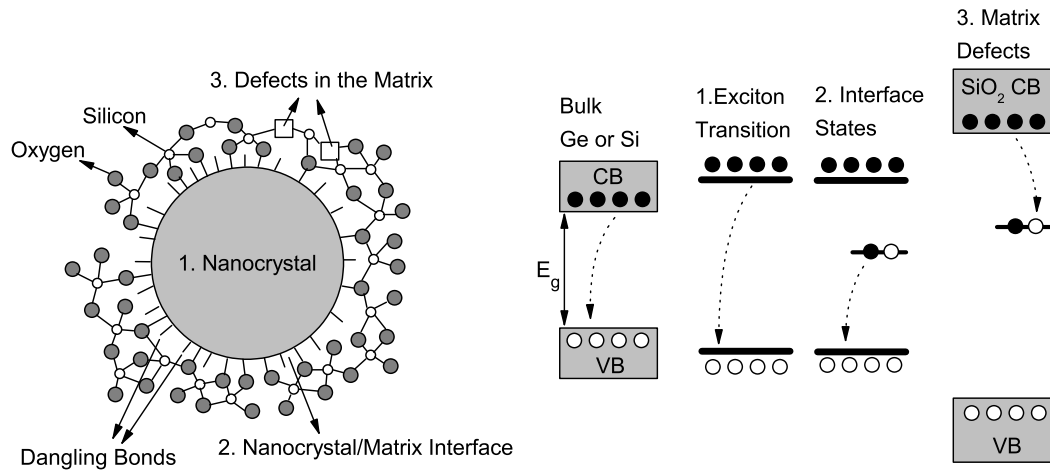


Figure 6.2: Possible light emitting mechanism of PL from nanocrystal/SiO<sub>2</sub> system: Left: pictorial illustration, right: energy levels including (1) recombination of electron-hole pairs in the nanocrystal, (2) radiative states at the interface between the nanocrystal and SiO<sub>2</sub> matrix (3) luminescent defect centers due to the matrix defects.

### 6.3 Possible Light Emitting Mechanisms from a Nanocrystal/SiO<sub>2</sub> System

Fig. 6.2 illustrates the possible light emitting mechanisms from SiO<sub>2</sub> matrix contains nanocrystals. The origin of PL from a nanocrystal/SiO<sub>2</sub> system, can be explained with two mechanisms. One is the radiative recombination of excitons in the nanocrystal. The other is the defect related mechanisms such as dangling bonds located at the interface between nanocrystal and SiO<sub>2</sub> matrix or matrix defects in the SiO<sub>2</sub> matrix. The classification of obtained PL from these structures is very important. For excitonic transitions one should see a size-dependent emission energy and PL lifetime due to the quantum confinement. On the other

hand, for defect-related transitions non-systematic emission energy and PL lifetime as a function of size is observed. Therefore, size-dependent PL emission energy is an evidence of nanocrystal formation in the SiO<sub>2</sub> and this is a widely used characterization method for nanocrystals.

#### 6.4 PL Spectrum of Si Nanocrystals

Fig. 6.3 depicts PL spectra of Si implanted samples taken at room temperature with a NdYag laser, using a total laser power of 300 mW. The beam diameter was smaller than 2 mm on the sample surface and emitted light was detected with a CCD camera. Samples were implanted with <sup>28</sup>Si at a dose of  $1.5 \times 10^{17} \text{ cm}^{-2}$  and annealed at various temperatures for 2 or 5 hr under N<sub>2</sub> atmosphere. For the as-implanted sample and samples annealed below 1050 °C a broad peak at  $\sim 625 \text{ nm}$  is observed. By increasing the annealing temperature up to 1050 °C we observed that the intensity of this peak increases first and decreases later, while a new peak appears at  $\sim 850 \text{ nm}$  (red arrow) which has two sub-peaks at  $\sim 775$  and  $900 \text{ nm}$ . The increase in the PL peak intensity at  $\sim 625 \text{ nm}$  could be explained in terms of annealing of defects that can give rise to non-radiative recombination. In addition, the increase in the annealing time at this temperature, causes the peak at  $\sim 625 \text{ nm}$  to disappear and the intensity of the peak at  $\sim 850 \text{ nm}$  to increase. It is interesting to see that at comparably high annealing time and temperature the peak at  $\sim 625 \text{ nm}$  disappears. Same behavior in Si implanted samples were reported by Ghislotti et al. [94]. They attributed this peak to the defects like clusters or chain of silicon. This assumption was also confirmed by

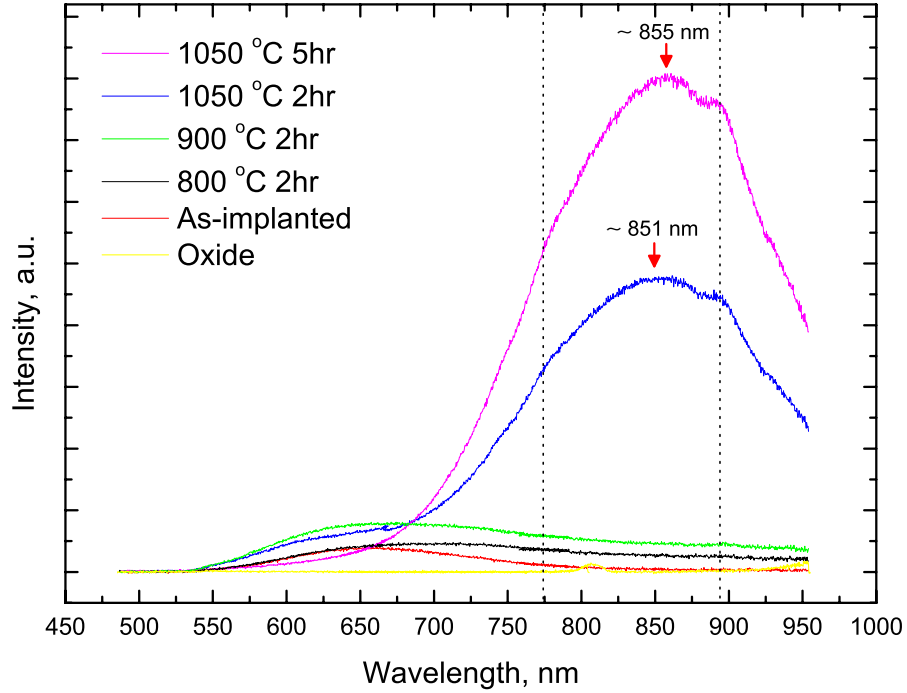


Figure 6.3: Room temperature PL of a sample which is implanted with  $^{28}\text{Si}$  at a dose of  $1.5 \times 10^{17} \text{ cm}^{-2}$  at 100 keV and annealed at various temperatures and times.

our etch experiment which will be discussed later in this chapter.

Comparison of the peak positions of samples annealed at 1050 °C for 2 and 5 hr points that, the peak at  $\sim 850 \text{ nm}$  shows a little redshift with increasing annealing time while the peaks at  $\sim 775$  and  $900 \text{ nm}$  remains at the same position. The redshift is expected because the size of the nanocrystals increases with annealing time and temperature, indicating that this peak results from the nanocrystals. The sudden appearance of this peak at 1050 °C evidences also that the source of this peak is nanocrystals. Since this temperature is closer to the melting temperature of bulk Si (the formation mechanism of nanocrystals is discussed in Chapter 2), the formation of nanocrystals is expected at this temperature.

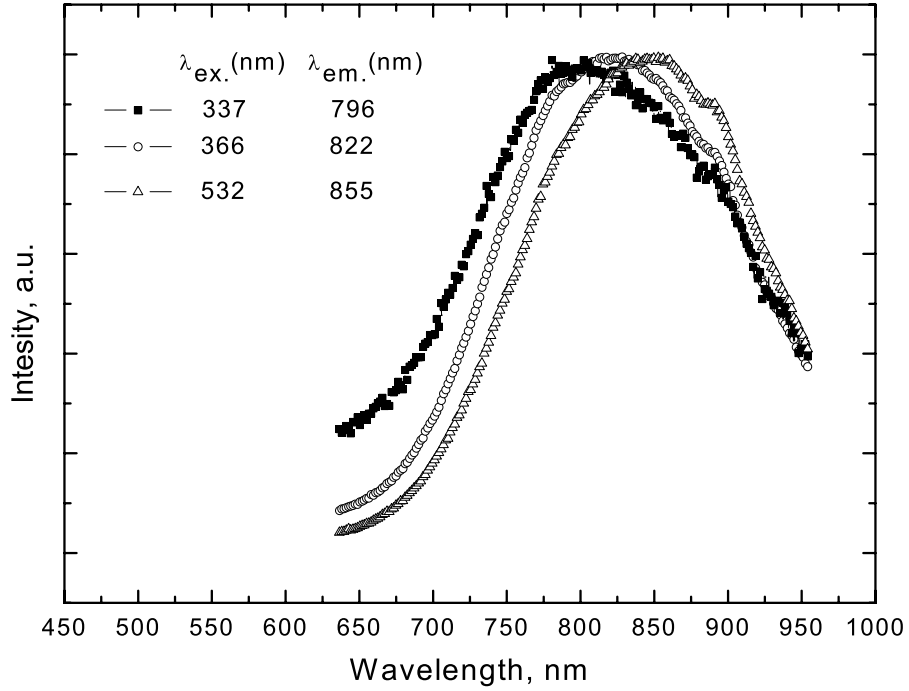


Figure 6.4: Excitation wavelength dependence of a sample implanted with  $^{28}\text{Si}$  at a dose of  $1.5 \times 10^{17} \text{ cm}^{-2}$  at 100 keV and annealed at  $1050 \text{ }^\circ\text{C}$  for 5 hr. The PL intensity was normalized in order to spot the shift easily.

Finally, it is remarkable to report that, the PL from these samples can be seen by naked eye in a dark room. It is observed that the samples annealed below  $1050 \text{ }^\circ\text{C}$  shows a green-yellow PL emission while the samples annealed at  $1050 \text{ }^\circ\text{C}$  shows a red PL emission under ultraviolet excitation.

#### 6.4.1 Dependence on Excitation Source

Dependence of PL spectra on the excitation source may reveal some useful information on the nanocrystals and their distribution. Fig. 6.4 shows the dependence of the peak, observed at  $\sim 850 \text{ nm}$  to the excitation wavelength ( $\lambda_{ex}$ ). It is clear that the PL peak shifts to higher energies as  $\lambda_{ex}$  decreases, showing

the presence of a selective excitation of nanocrystals. As we reported in the next section the PL peak shifts to lower energies when part of the SiO<sub>2</sub> matrix is removed from the surface. This indicates that nanocrystals with smaller size are located closer to the surface in agreement with the expected distribution of implanted Si atoms. The variation seen in Fig. 6.4 is then due to the fact that the absorption is enhanced with higher photon energy in the region close to the surface, where the smaller nanocrystals reside. Photons with smaller energy can penetrate deep into the matrix where larger nanocrystals are located. This, however may not be sufficient alone to explain the amount of shift seen in Fig. 6.4. Another possible mechanism leading to the selective excitation and shift in the PL spectrum might be the effect of the region surrounding the nanocrystals. As was suggested by Tetelbaum et al [95] the region surrounding the Si nanocrystals may have a different structure with different excitation and emission properties. This condition is schematically shown in Fig. 6.5. One might expect more efficient excitation/emission by the surface region with higher photon energy. If the surface region surrounding the nanocrystals has a higher band gap energy levels they should be more effective with light source having larger photon energy.

## 6.5 Observation of Si Nanocrystal Distribution by Etch-Measure Experiment

In order to verify the origin of the PL peaks, we carried out an etch-measure experiment. In this experiment, a thin layer (7 nm) of SiO<sub>2</sub> was removed from the surface and PL spectrum was taken. This process was repeated until the whole SiO<sub>2</sub> film was etched away. Buffered HF which consists of 250 gr NH<sub>4</sub>F,

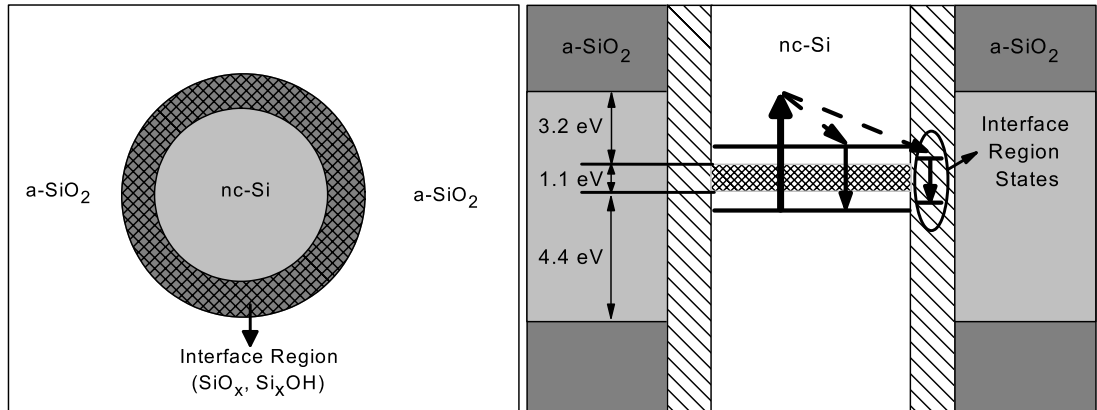


Figure 6.5: The sketch and energy band diagram of nc-Si/SiO<sub>2</sub> structure.

350 ml H<sub>2</sub>O and 12 ml HF was used as the etchant. The thickness of the non-implanted and implanted parts of the oxide layer were measured separately using an ellipsometer. It is found that, this solution has an etch rate of approximately 7 nm/min for the non-implanted SiO<sub>2</sub> while the etch rate of the implanted part is quite different and it varies with the Si concentration. It was observed that the etch rate slows down and reaches a minimum at around 140 nm from the surface where Si concentration is maximum (see Fig. 6.6).

In this experiment, we used the sample which was annealed at 1050 °C for 2 hr. This sample was chosen specially in order to observe the behavior of all main and sub peaks seen at ~ 625, 775, 850 and 900 nm. Since the peak position at ~ 900 nm remained unchanged with experimental conditions, the origin of this peak could not be from the nanocrystals. Although the peak at ~ 775 nm did not show any change either, this peak was attributed to the small nanocrystals

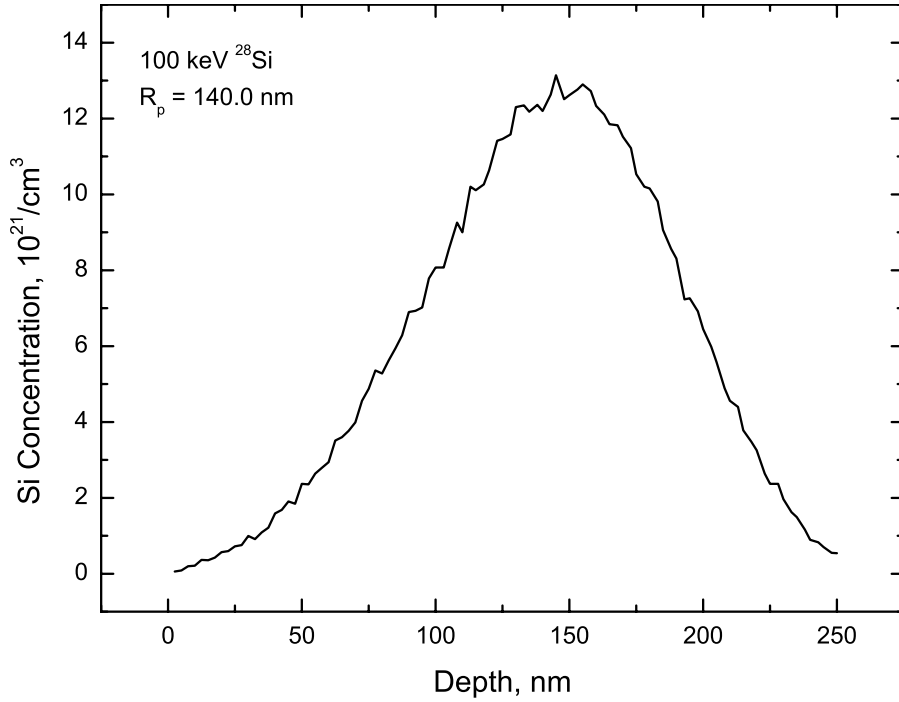


Figure 6.6: Depth profile calculated using the TRIM code for a Si implanted sample at a dose of  $1.5 \times 10^{17} \text{ cm}^{-2}$ . Corresponding Projected Range ( $R_p$ ) is indicated in the inset.

according to the result of the etch-measure experiment.

Fig. 6.6 illustrates the depth profile of implanted Si atoms as calculated by using the TRIM program. It can be seen from the figure that the Si concentration increases towards 140 nm from the surface and then decreases. We can then expect that by going deeper in the  $\text{SiO}_2$  matrix, the size of nanocrystals should increase first and then decrease later leading to a redshift first and blueshift later in the PL spectrum during the etch-measure experiment. Actually, this is the condition exactly what we observed from the experiment. Fig. 6.7 and 6.8 display the PL spectrum and the peak position of the PL spectrum as a function

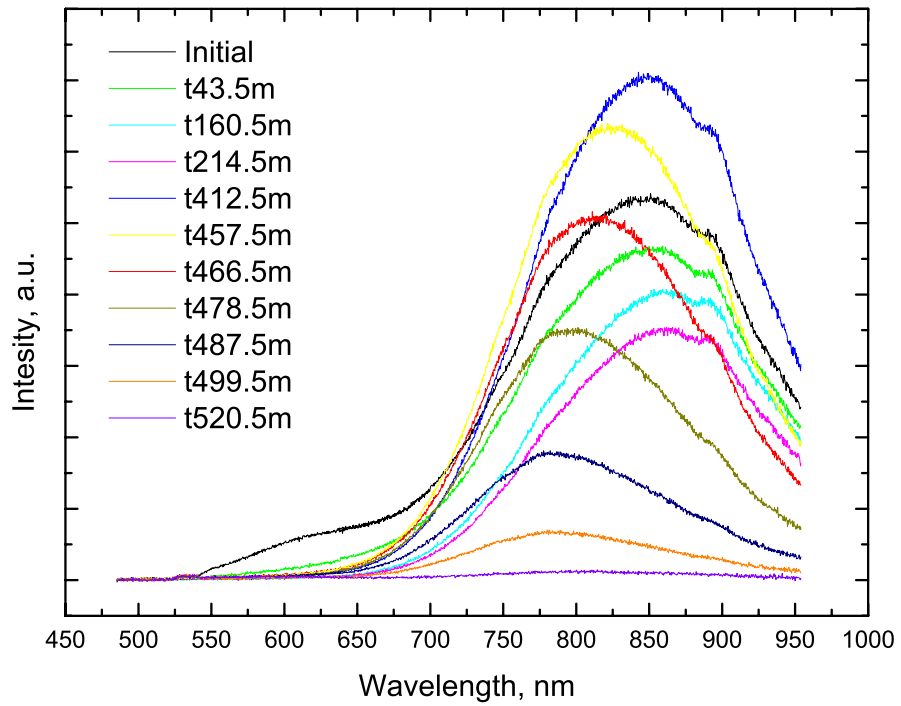


Figure 6.7: Room temperature PL of an etched sample which is implanted with  $^{28}\text{Si}$  at a dose of  $1.5 \times 10^{17} \text{ cm}^{-2}$  at 100 keV and annealed at  $1050^\circ\text{C}$  for 2 hr under  $\text{N}_2$  atmosphere.

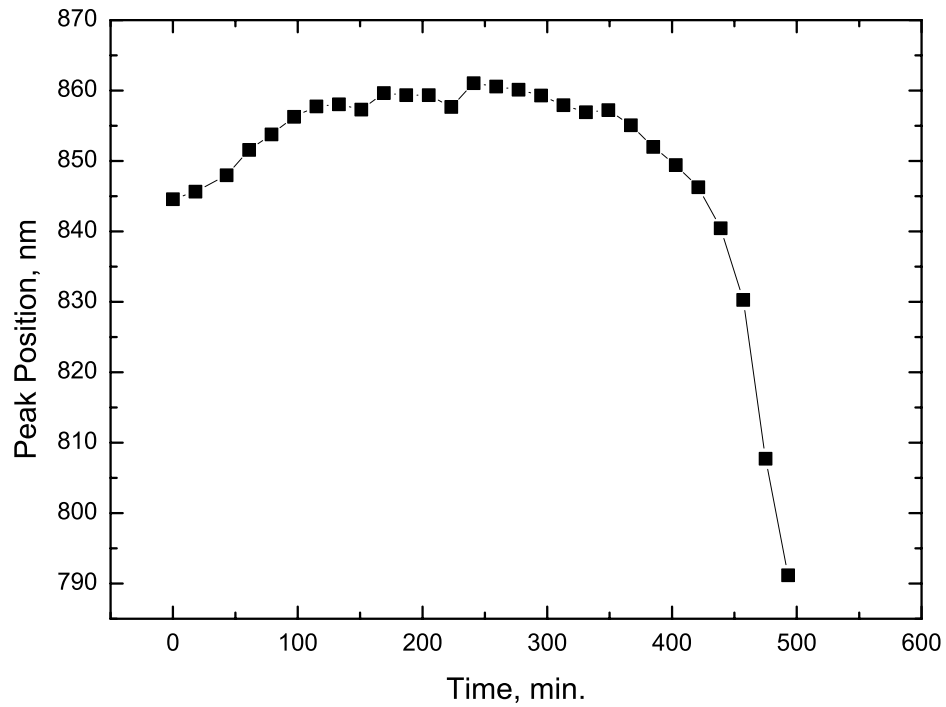


Figure 6.8: Room temperature PL summary of the peak position of the etched sample.

of etch time, respectively. It is seen that the PL peak at  $\sim 850$  nm shows a redshift first and blueshift afterwards down to a wavelength of 775 nm. This is in correlation with the Si distribution in the SiO<sub>2</sub> matrix, indicating strongly that the origin of both peaks at  $\sim 775$  nm and 850 nm are Si nanocrystals. Another important feature observed in Fig. 6.7 is that the intensity of the PL peak decreases with redshift and when the blueshift begins, it increases abruptly and then decreases again. This can be explained by considering the Si distribution and size dependent phenomenon: The size of the nanocrystals increases towards the projected range but the number of the larger nanocrystals decreases causing a decrease in the PL intensity. When the larger nanocrystals are removed by etching, a blueshift and an increase in the PL intensity was observed. Since the larger nanocrystals removed, small nanocrystals can be excited more easily, which means an increase in the PL intensity. As the number of the small nanocrystals decreases, with increasing the etch time, a decrease in the PL intensity again was observed at the final stage.

Another important result of this experiment is the behavior of the peak at  $\sim 625$  nm. After a small etch time this peak disappears, which indicates that the origin of this peak is related to the defects like clusters or chain of silicon located in the region close to the surface. Otherwise, this peak should have appeared for the further etch times. The result of the temperature dependent PL experiment provide more evidence for this conclusion.

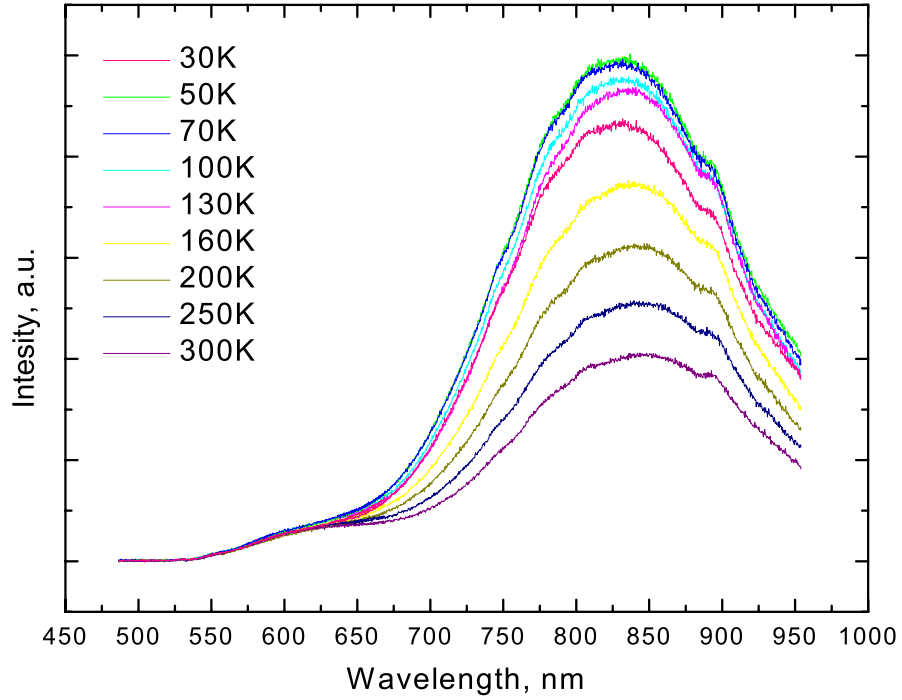


Figure 6.9: Temperature dependent PL of a sample which is implanted with  $^{28}\text{Si}$  at a dose of  $1.5 \times 10^{17} \text{ cm}^{-2}$  at 100 keV and annealed at  $1050 \text{ }^\circ\text{C}$  for 2 hr under  $\text{N}_2$  atmosphere.

## 6.6 Temperature Dependence of PL Spectrum

In order to study the temperature dependence of the PL spectrum a cryostat system which can work between 10-300 K was used. The excitation source is the 532 nm NdYag laser with a power of approximately  $7.5 \text{ W/cm}^2$  on the sample.

PL spectrum taken at various temperatures are shown in Fig. 6.9. It is seen that intensity of the PL peak at  $\sim 850 \text{ nm}$  increases with decreasing temperature between 70-300 K and decreases for further decrease in temperature, while that of the peak at  $\sim 625 \text{ nm}$  remains same. The temperature dependent PL intensity is theoretically described by Brongersma et al. [96]: The excitonic levels are split

by an energy,  $\Delta$ , due to the exchange interaction between the electron and hole (see Fig. 6.10). The lower level corresponds to a triplet state which is threefold degenerate and has a radiative decay rate  $R_T$ . The upper level corresponds to a singlet state having a radiative decay rate  $R_S$ . Then, the temperature dependence of the total radiative decay rate,  $R_R$ , can be calculated by assuming thermal equilibrium between the two levels:

$$R_R = \frac{3R_T + R_S \exp(-\Delta/kT)}{3 + \exp(-\Delta/kT)}. \quad (6.1)$$

At low temperature ( $T \approx 30$  K), only the triplet state is occupied and the radiative decay rate is small. Actually, the radiative decay rate of a pure triplet state should be zero as the transition is parity forbidden. However, the spin-orbit interaction slightly mixes the singlet and triplet states, making the transition weakly allowed. At higher temperatures, the singlet state becomes populated and the radiative rate increases between 30 and 70 K. When the temperature is increased further, the population in the singlet state converges to its high temperature value which is 1/3 of the total triplet population, and  $R_R$  is dominated by  $R_S$ .

The variation of PL spectra with the temperature observed in this work agrees well with this model. Further theoretical analysis of this result will be discussed in section 6.8.

## 6.7 Excitation Power Dependence of PL Spectrum

Recombination of electrons and holes is a process by which both carriers annihilate each other: Electrons fall in one or multiple steps into an empty state

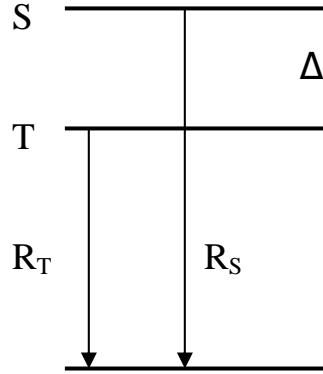


Figure 6.10: Schematic of the singlet and triplet energy levels, split by the electron-hole exchange energy  $\Delta$ .

which is associated with the hole. Both carriers eventually disappear in the process. The energy difference between the initial and final state of the electron is given off. This leads to one possible classification of the recombination processes: In the case of radiative recombination, this energy is emitted in the form of a photon, in the case of non-radiative recombination it is passed on to one or more phonons and in Auger recombination it is given off in the form of kinetic energy to another electron or hole (as shown in Fig. 6.11).

In this section, we discuss the excitation power dependence of nanocrystals, which is likely to be related with Auger recombination. It is well known that the radiative decay times of nanocrystals are of the order of ms [94]. The slow radiative decay time of nanocrystals causes the Auger recombination process to dominate at higher excitation power [97, 98]. During a fast Auger recombination

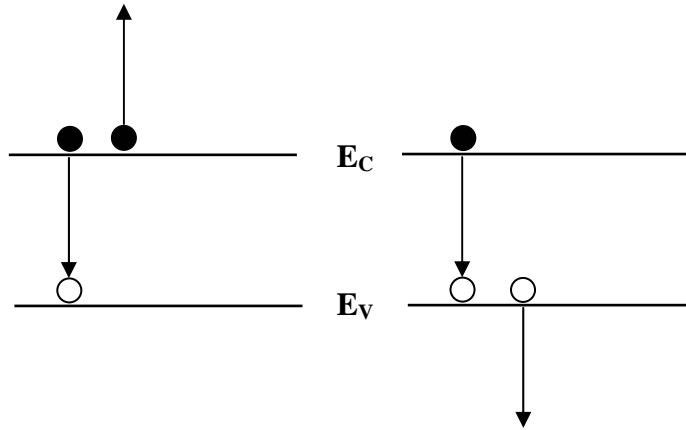
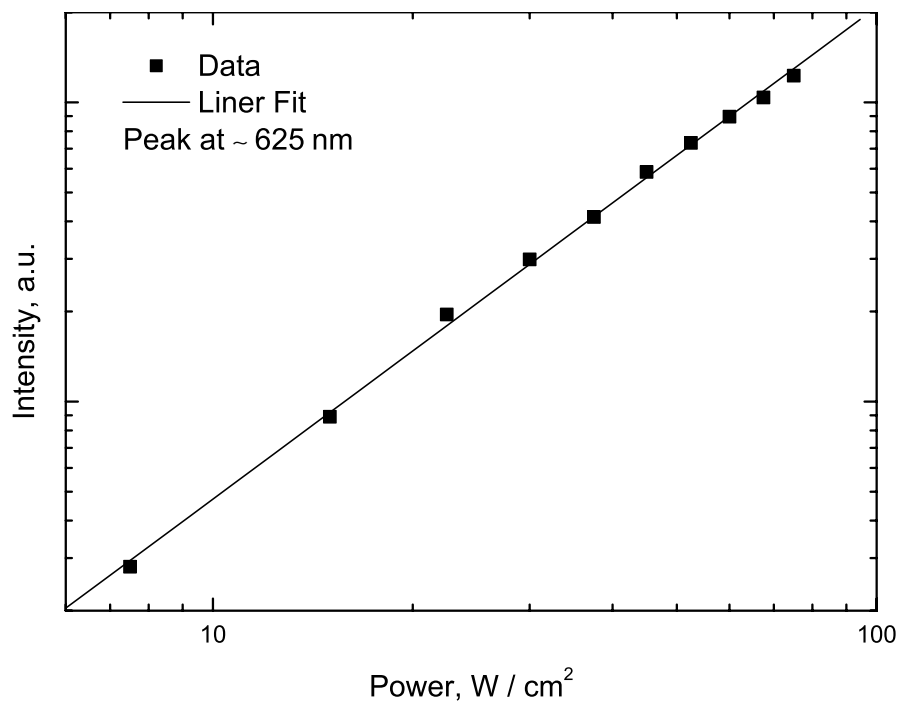


Figure 6.11: Illustration of Auger recombination. Filled and empty circles denote electrons and holes, respectively. Energy released during a transition from the conduction band ( $E_c$ ) to the valence band ( $E_v$ ) is given to another electron or hole.

process [99, 100], electron-hole pairs recombine non-radiatively leading to a reduction of the quantum yield of the PL. In Fig. 6.12, the different behaviors of the two PL peak at  $\sim 625$  and  $850$  nm against the laser power is clearly seen. The peaks at  $\sim 625$  and  $\sim 850$  nm have radiative decay times of the order of ns and ms, respectively [94]. Since the radiative decay time of the Auger process is of the order of ns, the peak at  $\sim 625$  nm is not affected by Auger process and has a direct proportionality with excitation power. In contrast to the peak at  $\sim 625$  nm, the peak at  $\sim 850$  nm has a slow radiative decay time and is dominated by Auger process at high excitation powers which quenches the PL intensity.

## 6.8 Theoretical Results

Since TEM and Raman measurements are not easily performed for Si nanocrystals in  $\text{SiO}_2$  matrix the PL measurements are the main source of information.



However PL spectroscopy does not provide any direct measurement of size and distribution of the nanocrystals. A theoretical calculation with some approximation is needed in order to extract this quantitative information from the PL spectroscopy of nanocrystals. ‘Average size’ and the distribution of the nanocrystal size can be estimated by using a model developed by Chen et al. [101] and later modified by Trwoga et al. [102]. Chen et al. have studied the effect of size distribution on PL spectra for Si nanocrystals and derived a relationship for the PL spectrum,  $P(\Delta E)$ , for quantum confinement of crystals that takes into account the increase in electron-hole pairs with increasing size:

$$P(\Delta E) = \frac{K}{\Delta E^3} \exp \left\{ -\frac{1}{2} \left( \frac{d_0}{\sigma} \right)^2 \left[ \left( \frac{\Delta E_0}{\Delta E} \right)^{1/2} - 1 \right]^2 \right\}, \quad (6.2)$$

where  $d_0$  is the average nanocrystal diameter,  $\sigma$  the standard deviation,  $K = bc^2/2\sqrt{2\pi}\sigma$  a normalization constant,  $\Delta E = \hbar\omega - (E_g - E_b)$  the energy shift due to confinement and  $\Delta E_0 = c/d^2$  a mean shift related to  $d_0$ . Here,  $E_g$  is the bulk Si gap,  $E_b$  the exciton energy,  $d$  the nanocrystal diameter,  $b$  a suitable normalization constant and  $c$  an appropriately dimensioned constant. Trwoga et al. included the oscillator strength,  $f(\Delta)$ , into their calculations in order to add the effect of the change in oscillator strength with  $d$  which was addressed by Khurgin et al. [103]. Based on the model of luminescence spectrum of Si nanocrystals by Chen et al. and extended by Trwoga et al., assuming the radiative recombination of confined excitons to be the major contributor to the luminescence spectra, the spectrum  $S(\Delta E)$  can be represented by

$$S(\Delta E) = P(\Delta E) \times f(\Delta E), \quad (6.3)$$

where,  $f(\Delta) = 0.15\Delta E^{2.25}$ . Fig. 6.13 and Table 6.1 show the calculated  $d_0$  and  $\sigma$  values of two different samples and the parameters used in our calculations, respectively. The calculated  $d_0$  values are consistent with the values available in the literature [82, 104], obtained directly from TEM picture.

Table 6.1: Parameters and values for the calculation of PL fit.

Parameter	Value
$E_g$	1.14 eV
$E_b$	0.08 eV
$c$	1323 eV $\text{\AA}^2$
$b$	0.1

We mentioned several times throughout this thesis that, increasing annealing temperature and time results in an increase in the nanocrystal size and the PL spectrum shows a redshift. This behavior is seen from Fig. 6.13 where the calculated  $d_0$  for sample annealed at 1050 °C for 5 hr is bigger than that for 2 hr. This is a further verification that the peak at  $\sim 850$  nm results from the Si nanocrystals.

The temperature dependence of PL spectrum was described by theoretical models [105, 106] according to which the intensity of the PL spectrum is given by

$$I(T) = \frac{I_0}{1 + \nu_0 \exp\left(\frac{T}{T_n} + \frac{T_r}{T}\right)}. \quad (6.4)$$

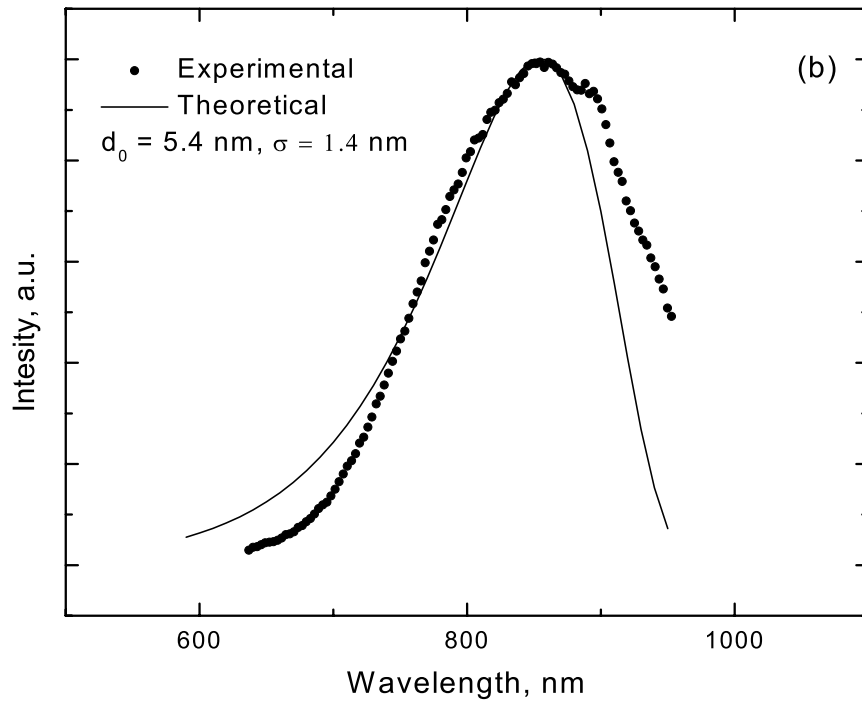
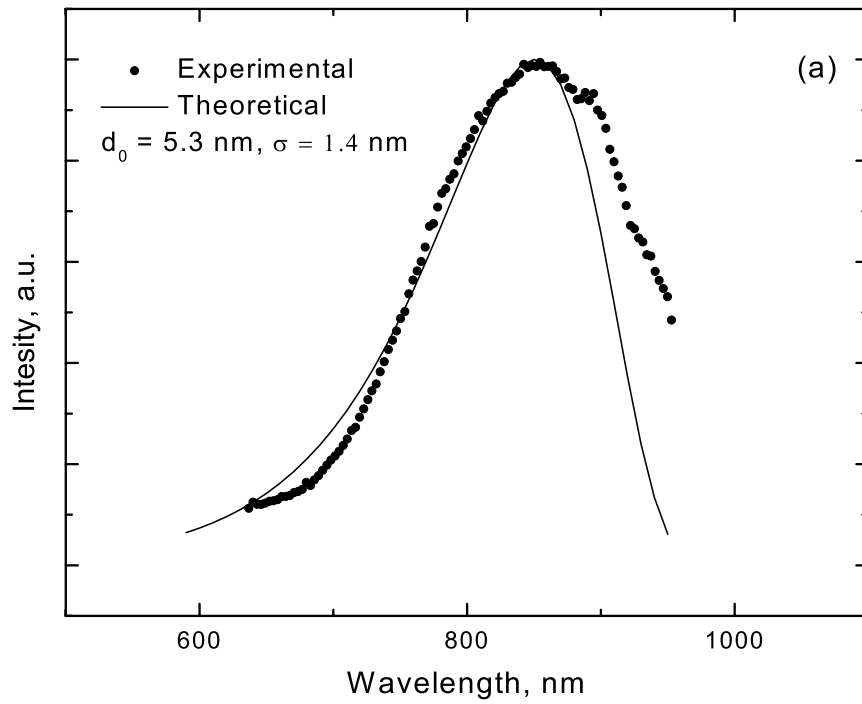


Figure 6.13: Theoretical PL fit result of a sample which is implanted with  $^{28}\text{Si}$  at a dose of  $1.5 \times 10^{17} \text{ cm}^{-2}$  at 100 keV and annealed at 1050 °C for (a) 2 hr and (b) 5 hr.

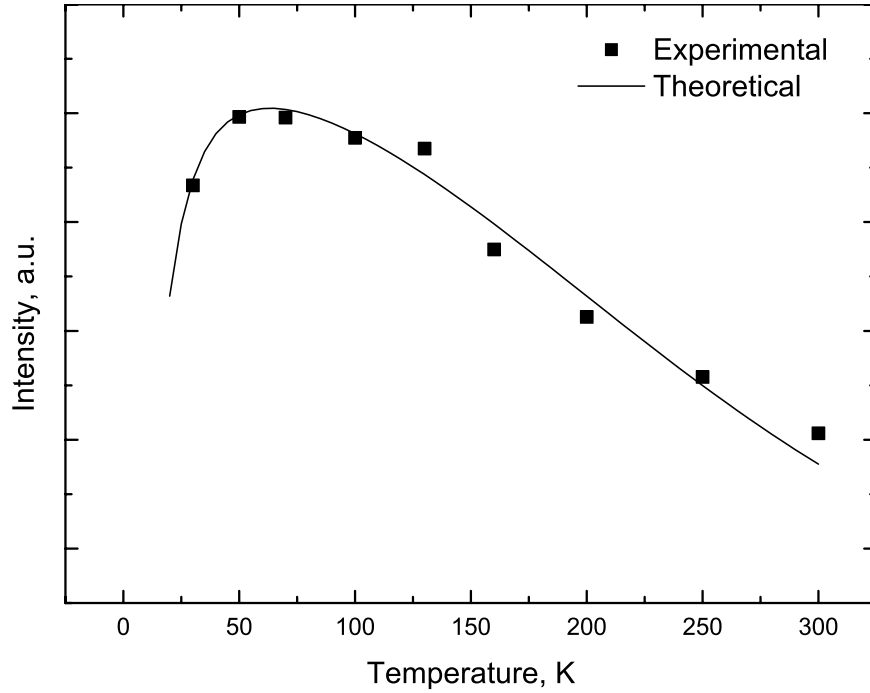


Figure 6.14: The variation of PL intensity with temperature.

Where,  $\nu_0 = \nu_n/\nu_r$  is the reduced frequency,  $I_0$  the initial intensity,  $T_n$  the characteristic non-radiative temperature and  $T_r$  the characteristic radiative temperature. We adopted this approach to our experimental results. In our calculations we used  $\nu_r = 7000 \text{ s}^{-1}$ ,  $\nu_n = 1000 \text{ s}^{-1}$ ,  $T_r = 40 \text{ K}$  and  $T_n = 100 \text{ K}$ . In Fig. 6.14 the comparison of experimental (squares) and theoretical (solid line) results are shown. It is seen from Fig. 6.14 that the agreement between the theoretical model and experimental results are very good.

## 6.9 Conclusion

In this chapter, it is shown that Si implanted and post annealed  $\text{SiO}_2$  exhibit broad and intense PL spectra at  $\sim 625$  and  $\sim 850 \text{ nm}$  depending on the annealing

temperature. It is demonstrated by etch experiment that the peak observed at  $\sim 850$  nm can be tuned between 790 and 860 nm which is related to the nanocrystal size.

To clarify the origin of the PL peaks seen at  $\sim 625$  and  $\sim 850$  nm, we have carried out different experiments such as temperature and excitation power dependence of PL spectrum. The result of these experiments together with that of the etch experiment shows us that the origin of these peaks are different. The peak at  $\sim 625$  nm found to be defect-related such as clusters or chain of silicon located near the surface while the peak at  $\sim 850$  nm was attributed to the Si nanocrystals.

Finally, by using a PL fit model, the average size and the distribution of the nanocrystal size is estimated for two similar samples annealed at same temperature but different annealing time and it was shown that the sample annealed at longer time contains larger nanocrystals compared to that of annealed shorter time.

## CHAPTER 7

### FTIR ANALYSIS OF Si AND Ge NANOCRYSTALS

#### 7.1 Introduction

FTIR spectroscopy is a widely used technique in the characterization of semiconductors and dielectrics. It is especially a powerful technique in the analysis of impurity content of SiO<sub>2</sub> grown on Si substrate. The stoichiometry of the SiO<sub>2</sub> and the hydrogen level can easily be obtained by FTIR measurements. We apply the FTIR analysis to Ge and Si implanted samples to observe and understand Ge and Si nanocrystal formation in SiO<sub>2</sub> matrix as a function of processing parameters.

FTIR measurements were conducted in the absorbance mode (350-2500 cm<sup>-1</sup>, 2 cm<sup>-1</sup> resolution), and the SiO stretching peak, including its intensity, FWHM and frequency, was used to monitor the structural changes of the SiO<sub>x</sub> films with annealing temperature.

#### 7.2 FTIR Spectroscopy

FTIR spectroscopy is a characterization technique widely used in physics, chemistry, and biology. It has the advantages of high spectral resolution, good signal-to-noise ratios, and the ability to measure a broad region of the spectrum

in a short amount of time. At the heart of an FTIR spectrometer is a Michelson interferometer. A parallel beam of collimated light from a broadband source is directed at a semitransparent beamsplitter. One of the two beams reflects off a movable mirror while the other beam reflects off a fixed mirror. The two beams recombine at the beamsplitter, travel through the sample, and finally impinge upon a detector. The detector signal is proportional to the intensity of the interfered beam and the plot of intensity versus optical path difference in real space is the interferogram. When the interferogram is Fourier transformed, the resulting function is a plot of the spectrum in frequency space. In practice, to maximize the signal-to-noise ratio, several hundred to several thousand interferograms are obtained and averaged before the Fourier transform is performed.

### 7.3 FTIR Results of Si Implanted SiO<sub>2</sub> Films

In this section, the effects of annealing on the structure of Si-rich SiO<sub>x</sub> ( $x < 2$ ) films formed by ion implantation into thermally grown SiO<sub>2</sub> films (250 nm) is presented. Samples implanted with a dose of  $1.5 \times 10^{17}$  Si cm<sup>-2</sup> at 100 keV and annealed at 800, 900 and 1050 °C for 2 hr under N<sub>2</sub> atmosphere were used in this study.

FTIR spectra of Si implanted samples as a function of annealing temperature and a non-implanted oxide are shown in Fig. 7.1. A characteristic feature seen in this figure is the asymmetric shape of the Si-O-Si bond stretching vibration peak in the lower wavenumber part of the spectra. This asymmetric feature can be related to the presence of the Si-O bond stretching vibration in SiO<sub>x</sub>. Tsu et al.

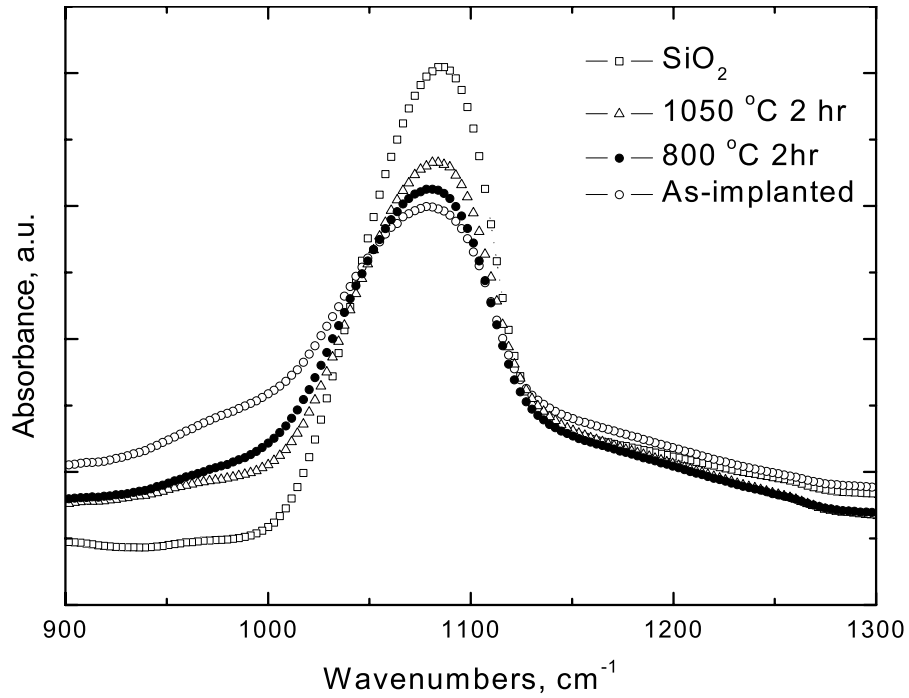


Figure 7.1: FTIR spectra of Si implanted samples.

[108] have shown that the Si-O bond stretching vibration for  $\text{SiO}_x$  ( $x < 2$ ) occurs between  $965$  and  $1060 \text{ cm}^{-1}$ . Thus, effect of ion implantation manifests itself as the formation of non-stoichiometric oxide with  $x < 2$ . This is understandable because of two main effects of Si ion implantation into  $\text{SiO}_2$ : the introduction of excess Si into the matrix and the breaking Si-O bonds during slowing down of the implanted atoms. Upon annealing at sufficiently high temperature the deformed oxide bonds start to recover and Si atoms precipitate to form nanocrystals, leading to decrease in the shoulder seen in the low wavenumber side of the FTIR curve.

Fig. 7.2 shows the evolution of the Si-O stretching peak, starting from the as-implanted state, as a function of annealing temperature. The effect of annealing on the stretching frequency is depicted in Fig. 7.2a. It is observed that an ion

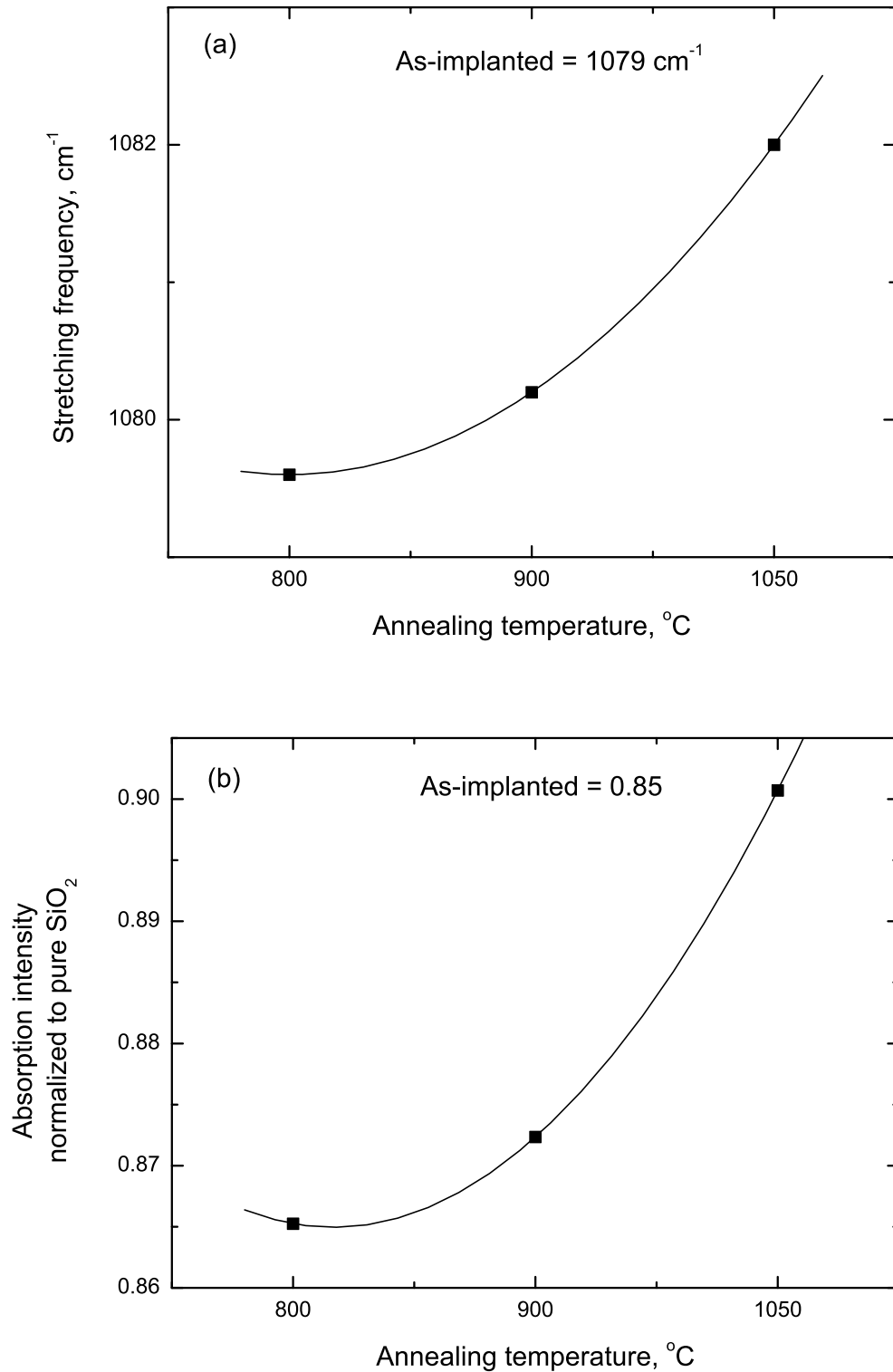


Figure 7.2: Annealing temperature dependence of (a) Si-O stretching frequency, (b) absorption intensity of the Si-O stretching peak, obtained from Si implanted samples. For reference, the as-implanted values are indicated also.

implantation energy of 100keV causes a redshift of the frequency from  $1084.8\text{ cm}^{-1}$  for thermally grown  $\text{SiO}_2$  to a lower frequency of  $1079.1\text{ cm}^{-1}$ . This indicates that ion implantation causes a change in the Si-O bond structures, and the redshift could be interpreted as the narrowing of the O-Si-O bond angle as a result of the replacement of O atoms by the implanted Si atoms and the formation of Si-Si bonds [107]. After annealing at  $1050\text{ }^\circ\text{C}$  the frequency is increased up to a value  $1082\text{ cm}^{-1}$  which indicates recovery of most of the Si-O networks from the as-implanted state. In Fig. 7.2b, absorption intensity normalized to pure  $\text{SiO}_2$  is presented. From this figure we observe that the intensity increases with annealing temperature which indicates that annealing causes the recovery of the Si-O networks.

#### 7.4 FTIR Results of Ge Implanted $\text{SiO}_2$ Films

In this study,  $\text{SiO}_2$  films implanted with Ge ions at an energy of 100 keV with a dose of  $1.5 \times 10^{17}\text{ cm}^{-2}$  were used. Thermal annealing was carried out at 800, 900 and  $1000\text{ }^\circ\text{C}$  for 1 hr under  $\text{N}_2$  ambient. FTIR spectrum obtained from the as-implanted sample shows a similar behavior to that of Si implanted sample (see Figs. 7.1 and 7.3). The same shoulder resulted from the deformation in the  $\text{SiO}_2$  matrix is seen in the low wavenumber side of the main peak. However, there are significant differences between the FTIR spectra of the Ge and Si implanted samples. A comparison of Figs. 7.1 and 7.3 reveals that the recovery of Si-O

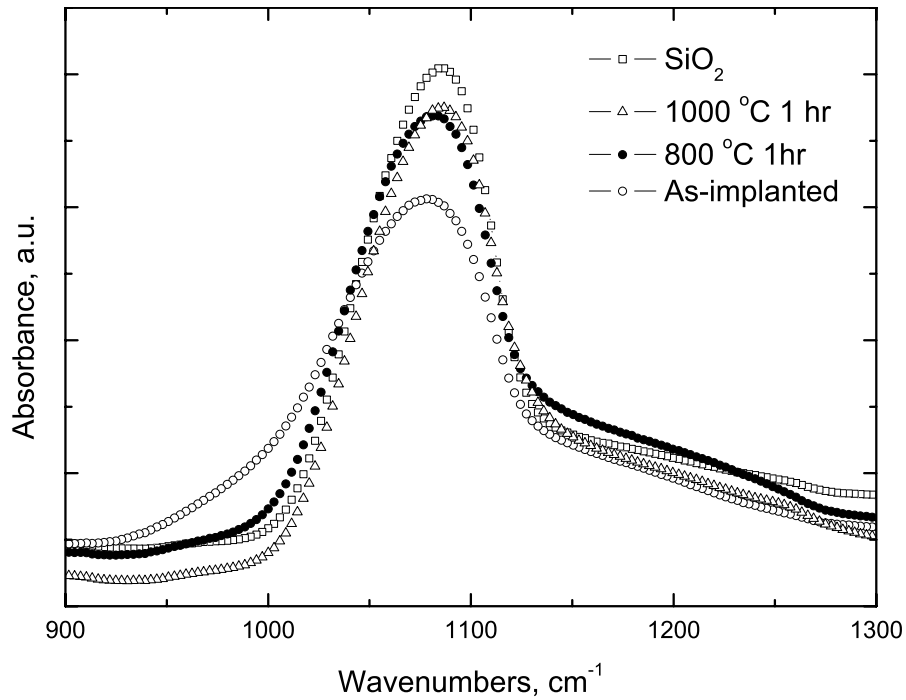


Figure 7.3: FTIR spectra of Ge implanted samples.

networks occurs at much lower temperatures in the case of the Ge implantation. This situation can be explained as follows: Excess Ge and Si ions in the  $\text{SiO}_2$  matrix deformed the Si-O bond structure by bonding with the O or Si. For example in the case of Ge implantation, Si-O bonds were broken and some Si-Ge-O, Ge-Ge, Ge-O, Si-Si and Si-Ge and individual dangling bonds are formed [109]. During the annealing process the excess Ge and Si atoms leave their initial positions and form clusters of a few nanometers. This segregation process is observed in the FTIR spectra as the reduction of the shoulder peak and recovery of the stoichiometry of the  $\text{SiO}_2$  matrix. It is well known that Ge atoms are not soluble in  $\text{SiO}_2$  and completely segregated out of the growing oxide if one oxidizes Si crystal containing Ge atoms [110]. This is due to the fact that the formation of

SiO<sub>2</sub> is thermodynamically more favorable than the formation of GeO [111] and that the binding energy of the Si-O bonds (8.3 eV) is greater than that of Ge-O (6.8 eV). In addition to the segregation as the precipitation into the matrix, we showed that some Ge atoms are segregated on the underlying Si substrate [112]. The rejection of Ge by the SiO<sub>2</sub> matrix leads to high diffusivity for Ge atoms. This results in the formation of Ge nanocrystals at low temperatures compared to Si nanocrystals. This situation can also be perceived from the Figs. 7.2 and 7.4. In these figures, stretching frequency and absorption intensity show direct proportionality in the case of Ge implanted samples whereas in the case of Si implanted samples, they show little increase at low annealing temperatures.

Fig. 7.5 shows the FWHM of the Si-O stretching peak, obtained from Ge and Si implanted samples, as a function of annealing temperature. For both implantation the FWHM of the Si-O stretching peak decreases with increasing annealing temperature, which implies that annealing promotes the growth of a well-ordered SiO<sub>2</sub> structure in the SiO<sub>x</sub> films. The FWHM of the FTIR signal is a measure of the chemical and structural perfectness of the film. We see that FWHM of the Ge implanted film approaches that of pure SiO<sub>2</sub> film quicker than the Si implanted sample, showing again that SiO<sub>2</sub> recovers itself as a result of Ge segregation at low temperatures.

## 7.5 Conclusion

FTIR spectroscopy has been employed to observe and understand Ge and Si nanocrystal formation in SiO<sub>2</sub> matrix as a function of processing parameters.

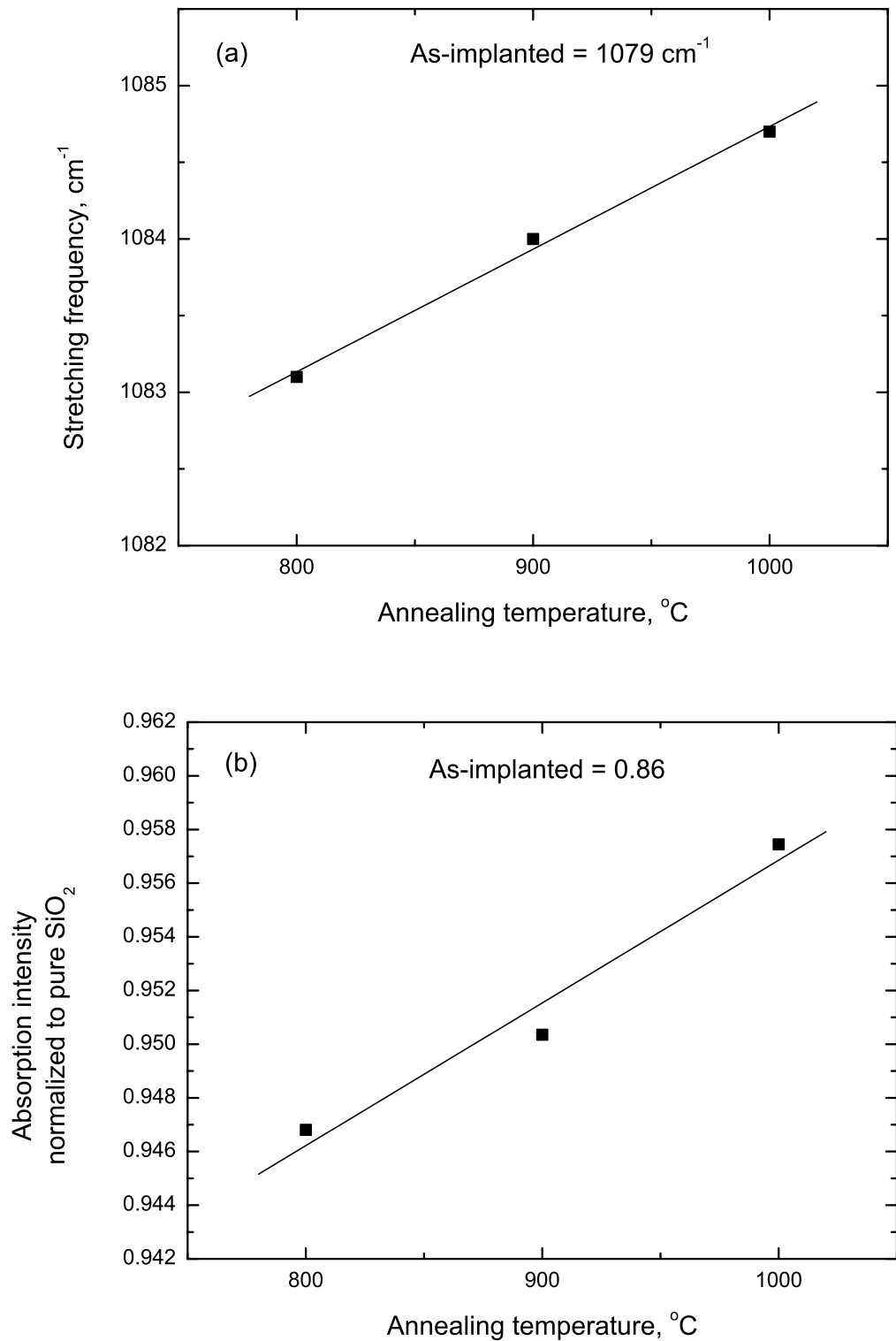


Figure 7.4: Annealing temperature dependence of (a) Si-O stretching frequency, (b) absorption intensity of the Si-O stretching peak, obtained from Ge implanted samples. For reference, the as-implanted values are indicated also.

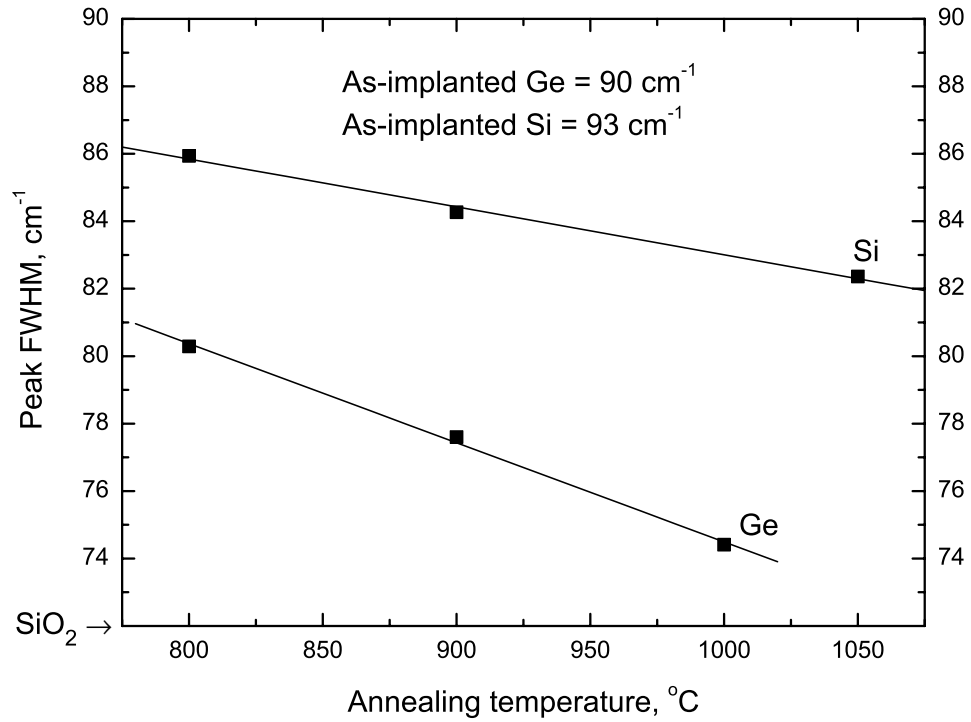


Figure 7.5: Annealing temperature dependence of FWHM of the Si-O stretching peak, obtained from Ge and Si implanted samples. For reference the non-implanted SiO<sub>2</sub> and corresponding as-implanted values are indicated.

The Si-O stretching peak of FTIR spectra was used to monitor the structural changes of the SiO<sub>x</sub> films with annealing temperature. It was demonstrated that, deformed Si-O bonds tend to recover as a function of annealing temperature. FTIR spectra analysis of implanted samples shows that the recovery process is quite different in Ge and Si implanted samples. It was shown that, in Ge implanted samples the recovery process occurs at low temperatures compared to the Si implanted ones.

## CHAPTER 8

### CONCLUSION

Si has been the basic material of microelectronics for 40 years because of its excellent mechanical, chemical and electrical properties. However, the decrease in size of microelectronic parts used in today's technology force the physical limits of Si. In addition to this, the huge development of communication technology demands for optoelectronic functional units able to generate, modulate and process optical signals. Unfortunately, because of its inefficient light emitting property, Si can not be used to operate as a light emitter. This problem is the main motivation of intense research for replacing the light emitting materials used in today's technology with another one which is integrated well in the current Si technology. Recently, it is shown that semiconductor nanocrystals embedded in SiO<sub>2</sub> matrix is a way to find the missing link between Si based electronics and optoelectronics in microelectronic devices.

In this study, Ge and Si ions were implanted into SiO<sub>2</sub> films at various doses and energies in order to form Ge and Si nanocrystals in SiO<sub>2</sub>. Implanted samples were annealed at different temperatures and times to characterize the formation and evolution of nanocrystals in SiO<sub>2</sub> matrix. Implanted and annealed samples were investigated by using TEM, XPS, SIMS, EDS, SAD, PL, Raman and FTIR spectroscopy.

In Chapter 4, the formation and evolution of Ge nanocrystals were clearly demonstrated by TEM. It was shown that, annealing time, annealing temperature, annealing ambient, implantation dose and implantation energy are important parameters for the formation and evolution of semiconductor nanocrystals in the SiO<sub>2</sub> matrix. We demonstrated that Ge nanocrystal sizes increase as a function of annealing temperature, annealing time and implantation dose and reaches a maximum of 25 nm for the sample implanted with Ge at a dose of  $1 \times 10^{17} \text{ cm}^{-2}$  at 100 keV and annealed at 1000 °C for 30 min or 900 °C for 1hr. It was shown that annealing Ge implanted samples at 1000 °C for 1 hr under N<sub>2</sub> (probably contains trace amount of O<sub>2</sub> or H<sub>2</sub>) results in an increase in diffusivity of Ge atoms in SiO<sub>2</sub> matrix which causes the Ge nanocrystals to dissolve, diffuse towards the surface and oxidized there.

It was shown in Chapter 5 that, it is possible to calculate both the size and size distribution of Ge nanocrystals, by fitting the asymmetry appears at the left side of the Raman lineshapes, in the framework of the phonon confinement model. A comparison with the TEM images indicated that this model provided a successful estimation of the size and size distribution of Ge nanocrystals in SiO<sub>2</sub> matrix.

In Chapter 6, Si implanted samples were examined by using PL spectroscopy and two broad PL bands were observed for the annealed samples. It was found that samples annealed at low and high temperatures exhibit a yellow-orange and near-infrared emission, respectively. These emission bands have been attributed to two distinct sources: Defects such as clusters or chain of silicon atoms located

near the surface and radiative recombination of quantum-confined excitons in the Si nanocrystals. It was shown that PL band observed at the near-infrared region exhibits a redshift and shows an increase in intensity as a function of annealing time for samples annealed at 1050 °C as an indication of nanocrystal formation. Maximum intensity for the PL peak at  $\sim 850$  nm was obtained by annealing Si implanted samples at 1050 °C for 5 hr. We demonstrated that intensity of the PL peak observed at  $\sim 625$  nm reaches its maximum at 900°C for 2 hr annealing and decreases for further increase in annealing temperature.

One of the samples, which contains both PL peaks, was investigated by an etch experiment and the variation in the PL spectrum was designated. The result of this experiment revealed that the PL spectrum shows a redshift (blueshift) with an increase (decrease) in the nanocrystal size. It was illustrated with this experiment that the PL emission, obtained from a sample which is implanted with  $^{28}\text{Si}$  at a dose of  $1.5 \times 10^{17} \text{ cm}^{-2}$  at 100 keV and annealed at 1050 °C for 2 hr under  $\text{N}_2$  atmosphere, can be tuned between 790-860 nm.

PL spectrum of Si implanted samples were studied by using different excitation sources. The spectrum was found to depend on the wavelength of the excitation source. The peak position was varied in the wavelength range of 796-855 nm by using different sources having wavelengths between 337-532 nm.

It was verified by temperature and excitation power dependence of PL spectrum, obtained from Si implanted samples, that the origin of the two PL peaks observed at  $\sim 625$  and 850 nm is different. Intensity of the peak at  $\sim 850$  nm exhibits a temperature dependent behavior while the peak at  $\sim 625$  nm does

not exhibit any significant change. We observed that intensity of the peak  $\sim 850$  nm increases (compared to that of the room temperature) with decreasing sample temperature and reaches a maximum value at 70K. Further decrease in the sample temperature causes the peak intensity to decrease and this behavior was explained by a model related with the splitting of excitonic levels due to the exchange interaction between the electron and hole. It was shown by excitation power dependence of PL spectrum experiment that the intensity of the peak observed at  $\sim 850$  nm has been dominated by the Auger process at high excitation powers.

Finally in Chapter 7, FTIR spectroscopy was employed to the Ge and Si implanted samples to observe and understand Ge and Si nanocrystal formation in SiO<sub>2</sub> matrix as a function of processing parameters. The formation of Ge and Si nanocrystals in SiO<sub>2</sub> matrix was monitored by an indirect way which is the recovery of Si-O networks. We have shown that the recovery process in Si-O networks is quite different in Ge and Si implanted samples and the deformation caused by Ge atoms in the SiO<sub>2</sub> matrix can be recovered by annealing the implanted samples at 900 °C for 1 hr under N<sub>2</sub> ambient while for the Si implanted samples the recovery process could not be completed even at 1050 °C for 2 hr annealing. This is a result of effective segregation of Ge atoms from the SiO<sub>2</sub> matrix.

## REFERENCES

- [1] Faradays diary, Vol. VII, The Royal Institution of Great Britain, *T. Martin, Bell and Sons* (1936) 63.
- [2] J. F. Suyver, “Synthesis, Spectroscopy and Simulation of Doped Nanocrystals”, Ph. D. Thesis, Physics and Chemistry of Condensed Matter, Debye Instituut., Universiteit Utrecht, Netherlands (2003).
- [3] G. Jaeckel, *Z. Tech. Phys.* **6** (1926) 301.
- [4] L. T. Canham, *Appl. Phys. Lett.* **57** (1990) 1046.
- [5] Fundamentals of photonics, *B. E. A. Saleh and M. C. Teich, Wiley* (1991) 573.
- [6] Optical Properties of Semiconductor Nanocrystals, *S. V. Gaponenko, Cambridge University Press* (1998) 28.
- [7] A. D. Yoffe, *Adv. Phys.* **42** (1993) 173.
- [8] Optical Properties of Semiconductor Nanocrystals, *S. V. Gaponenko, Cambridge University Press* (1998) 41.
- [9] T. Takagahara and K. Takeda, *Phys. Rev. B* **46** (1992) 15578.
- [10] Optical Characterization of Semiconductors: Infrared, Raman, and Photoluminescence Spectroscopy, *S. Perkowitz, Academic Press* (1993) 27.
- [11] M. Hao, H. Hwang, and J. C. Lee, *Appl. Phys. Lett.* **62** (1993) 1530.
- [12] S. Tiwari, F. Rana, H. Hanafi, A. Hartstein, E. F. Crabbé, and Kevin Chan, *Appl. Phys. Lett.* **68** (1996) 1377.
- [13] H. I. Hanafi, S. Tiwari and I. Khan, *IEEE T. Electron. Dev.* **43** (1996) 1553.
- [14] Y. Shi, K. Saito, H. Ishikuro and T. Hiramoto, *J. Appl. Phys.* **84** (1998) 2358.
- [15] J. von Borany, T. Gebel, K. H. Stegemann, H. J. Thees and M. Wittmaack, *Solid. State. Electron.* **46** (2002) 1729.
- [16] P. Dimitrakis, E. Kapetanakis, P. Normand, D. Skarlatos, D. Tsoukalas, K. Beltsios, A. Claverie, G. Benassayag, C. Bonafos, D. Chassaing, M. Carrada and V. Soncini, *Mat. Sci. Eng. B* **101** (2003) 14.

- [17] O. González-Varona, B. Garrido, S. Cheylan, A. Pérez-Rodríguez, A. Cuadras and J. R. Morante, *Appl. Phys. Lett.* **82** (2003) 2151.
- [18] G. Molas, B. De Salvo, D. Mariolle, G. Ghibaudo, A. Toffoli, N. Buffet and S. Deleonibus, *Solid. State. Electron.* **47** (2003) 1645.
- [19] Silicon Strategies, <http://www.siliconstrategies.com>
- [20] L. Rebohle, J. von Borany, R. A. Yankov, W. Skorupa, I. E. Tyschenko, H. Fröb and K. Leo *Appl. Phys. Lett.* **71** (1997) 2809.
- [21] M. J. Lu, X. M. Wua and W. G. Yao, *Mat. Sci. Eng. B* **100** (2003) 152.
- [22] J. Y. Zhang, Y. H. Ye and X. L. Tan, *Appl. Phys. Lett.* **74** (1999) 2459.
- [23] J. Y. Zhang, Y. H. Ye, X. L. Tan and X. M. Bao, *IEEE Appl. Phys. A* **71** (2000) 299.
- [24] N. Lalic and J. Linnros, *J. Lumin.* **80** (1999) 263.
- [25] G. Franzò, A. Irrera, E. C. Moreira, M. Miritello, F. Iacona, D. Sanfilippo, G. Di Stefano, P. G. Fallica and F. Priolo, *Appl. Phys. A* **74** (2002) 1.
- [26] T. Matsuda, M. Kawabe, H. Iwata, Nonmembers and T. Ohzone, *IEICE T. Electron.* **11** (2002) 1895.
- [27] J. De La Torre, A. Souifi, A. Poncet, C. Busseret, M. Lemiti, G. Bremond, G. Guillot, O. Gonzalez, B. Garrido, J. R. Morante and C. Bonafos, *Physica E* **16** (2003) 326.
- [28] A. Irreraa, D. Pacifici, M. Miritello, G. Franzo, F. Priolo, F. Iacona, D. Sanfilippo, G. Di Stefano and P.G. Fallica, *Physica E* **16** (2003) 395.
- [29] K. V. Shcheglov, C. M. Yang, K. J. Vahala and H. A. Atwater, *Appl. Phys. Lett.* **66** (1995) 745.
- [30] D. Muller, P. Knápek, J. Fauré, B. Prevot, J. J. Grob, B. Hönerlage and I. Pelant, *Nucl. Instr. and Meth. B* **148** (1999) 997.
- [31] L. Rebohle, J. von Borany, H. Fröb and W. Skorupa *Appl. Phys. B* **71** (2000) 131.
- [32] Evident Technologies, <http://www.evidenttech.com>
- [33] T. S. Iwayama, M. Ohshima, T. Niimi, S. Nakao, K. Saitoh, T. Fujita and N. Itoh, *J. Phys.: Condens. Matter* **5** (1993) L375.
- [34] J. von Borany, R. Grotzschel, K.H. Heinig, et al., *Solid-State Electron* **43** (1999) 1159.
- [35] T. S. Iwayama, S. Nakao and K. Saitoh, *Appl. Phys. Lett.* **65** (1994) 1814.

- [36] R. K. Soni, L. F. Fonseca, O. Resto, M. Buzaianu and S. Z. Weisz, *J. Lumin.* **83-84** (1999) 187.
- [37] Y. Maeda, N. Tsukamoto, Y. Yazawa, Y. Kanemitsu and Y. Masumoto, *Appl. Phys. Lett.* **59** (1991) 3168.
- [38] H. Takagi, H. Ogawa, Y. Yamazaki, A. Ishizadi and T. Nakagiri, *Appl. Phys. Lett.* **56** (1990) 2379.
- [39] Y. Ishikawa, N. Shibata and S. Fukatsu, *Jpn. J. Appl. Phys.* **36** (1997) 4035.
- [40] VLSI Technology, 2<sup>nd</sup> ed. *S. M. Sze, McGraw Hill* (1988) 98.
- [41] M. Sahin, "Synthesis of Silicon-Germanium by High Dose Germanium Ion Implantation into Silicon", M. Sc. Thesis, Department of Physics, METU, Ankara (1999).
- [42] SRIM: The Stopping and Range of Ions in Matter, Program Manual *J. F. Ziegler* (1996).
- [43] M. L. Brongersma, A. Polman, K. S. Min, E. Boer, T. Tambo and H. A. Atwater, *Appl. Phys. Lett.* **72** (1998) 2577.
- [44] A. R. Wilkinson, and R. G. Elliman, *Phys. Rev. B* **68** (2003) 155302.
- [45] E. Neufeld, S. Wang, R. Apetz, Ch. Buchal, R. Carius, C. W. White and D. K. Thomas, *Thin Solid Films* **294** (1997) 238.
- [46] Fundamentals of Physical Metallurgy, *J. D. Verhoeven, John Wiley and Sons* (1975) 400.
- [47] J. M. Lifshitz and V. V. Slyozov, *J. Phys. Chem Solids* **19** (1961) 35.
- [48] C. Wagner, *Z. Elektrochem.* **65** (1961) 581.
- [49] The Mechanism of Phase Transformations in Crystalline Solids, Fundamentals of Physical Metallurgy, *J. C. Cahn, Institute of Metals: London* (1969) 103.
- [50] C. Bonafos, B. Colombeau, M. Carrada, A. Altibelli and A. Claverie *Mat. Sci. Eng. B* **88** (2002) 112.
- [51] M. Volmer and A. Weber, *Z. Physik. Chem.* **119** (1925) 277.
- [52] Fundamentals of Physical Metallurgy, *J. D. Verhoeven, John Wiley and Sons* (1975) 220.
- [53] Fundamentals of Physical Metallurgy, *J. D. Verhoeven, John Wiley and Sons* (1975) 222.

- [54] The Mechanism of Phase Transformations in Crystalline Solids, Fundamentals of Physical Metallurgy, *J. C. Cahn, Institute of Metals: London* (1969) 110.
- [55] Fundamentals of Physical Metallurgy, *J. D. Verhoeven, John Wiley and Sons* (1975) 402.
- [56] C. Y. Li and R. A. Oriani, in Oxide Dispersion Strengthening, G. S. Ansell, T. D. Cooper, and F. V. Lenel, *Eds. Metallurgical Society Conference, Vol. 47, Gordon and Breach, New York* (1968) 431.
- [57] E. S. Marstein, A. E. Gunnæs, U. Serincan, R. Turan, A. Olsen and T. G. Finstad, *Surf. Coatings Technol.* **158** (2002) 544.
- [58] A. Markwitz, B. Schmidt, W. Matz, R. Grötzschel and A. Mücklich, *Nucl. Instr. and Meth. B* **142** (1998) 338.
- [59] Scanning Microscopy 7 *J.H. Evans* (1993) 837.
- [60] Treatise on Materials Science and Technology, Microstructure of Irradiated Materials, 7, *H.S. Rosenbaum, Academic Press* (1975).
- [61] B. Schmidt, D. Grambole and F. Herrmann, *Nucl. Instr. and Meth. B* **191** (2002) 482.
- [62] M. Klimenkov, W. Matz and J. von Borany, *Nucl. Instr. and Meth. B* **168** (2000) 367.
- [63] M. Klimenkov, W. Matz, S.A. Nepijko and M. Lehmann, *Nucl. Instr. and Meth. B* **179** (2001) 209.
- [64] K. Beltsios, P. Normand, E. Kapetanakis, D. Tsoukalas and A. Travlos, *Microelectron. Eng.* **61** (2002) 631.
- [65] H. Hosono and J. Nishi, *Opt. Lett.* **24** (1999) 1352.
- [66] X. L. Wu, T. Gao, X. M. Bao, F. Yan, S. S. Jiang and D. Feng, *J. Appl. Phys.* **82** (1997) 2704.
- [67] D. R. dos Santos and I. L. Torriani, *Solid State Commun.* **85** (1993) 307.
- [68] P. M. Fauchet and I. H. Campbell, *Critical Rev. Solid State Mat. Sci.* **14** (Supplement 1) (1988) 79.
- [69] A. G. Rolo, M. I. Vasilevskiy, O. Conde and M. J. M. Gomes, *Thin Solid Films* **336** (1998) 58.
- [70] S. Choi, S. Han and S. Hwang, *Thin Solid Films* **413** (2002) 177.
- [71] D. Nesheva, C. Raptis, A. Perakis, I. Bineva, Z. Aneva, Z. Levi, S. Alexandrova and H. Hofmeister, *J. Appl. Phys.* **92** (2002) 4678.

- [72] H. Richter, Z.P. Wang, and L. Ley, *Solid State Commun.*, **39** (1981) 625.
- [73] I. H. Campbell and P.M. Fauchet, *Solid State Commun.*, **58** (1986) 739.
- [74] A. Czachor , *Phys. Rev. B* **32** (1985) 5628.
- [75] D. Bermejo and M. Cardona , *J. Non-Cryst. Solids* **32** (1979) 405.
- [76] M. Fujii, S. Hayashi and K. Yamamoto, *Appl. Phys. Lett.* **57** (1990) 2692.
- [77] M. Fujii, S. Hayashi and K. Yamamoto, *Jpn. J. Appl. Phys.* **30** (1991) 687.
- [78] A.V. Kolobov, *J. Appl. Phys.* **87** (2000) 2926.
- [79] M. Kawata, S. Nadahara, J. Shiozawa, M. Watanabe and T. Katoda, *J. Elec. Mater.* **19** (1990) 407.
- [80] W. Skorupa, R. A. Yankov, I. E. Tyschenko, H. Fröb , T. Böhme and K. Leo, *Appl. Phys. Lett.* **68** (1996) 2410.
- [81] L. S. Liao, X. M. Bao, X. Q. Zheng, N. S. Li and N. B. Min, *Appl. Phys. Lett.* **68** (1996) 850.
- [82] S. Guha, M. D. Pace, D. N. Dunn and I. L. Singer, *Appl. Phys. Lett.* **70** (1997) 1207.
- [83] M. Zacharias and P. M. Fauchet, *Appl. Phys. Lett.* **71** (1997) 380.
- [84] J. Y. Zhang, X. M. Bao, Y. H. Ye and X. L. Tan, *Appl. Phys. Lett.* **73** (1998) 1790.
- [85] S. Guha, *J. Appl. Phys.* **84** (1998) 5210.
- [86] T. Gao, S. Tong, X. Bao and G. G. Siu, *Phys. Lett. A* **253** (1999) 234.
- [87] J. Y. Jeong, S. Im, M. S. Oh, H. B. Kim, K. H. Chae, C. N. Whang and J. H. Song, *J. Lumin.* **80** (1999) 285.
- [88] J. Y. Jeong, S. I. Im, M. S. Oh, H. B. Kim, K. H. Chae, C. N. Whang and J. H. Song, *J. Korean Phys. Soc.* **35** (1999) 591.
- [89] S. Takeoka, M. Fujii, S. Hayashi and K. Yamamoto, *Appl. Phys. Lett.* **74** (1999) 1558.
- [90] X. L. Wu, T. Gao, G. G. Siu, S. Tong and X. M. Bao, *Appl. Phys. Lett.* **74** (1999) 2420.
- [91] H. B. Kim, K. H. Chae, C. N. Whang, J. Y. Jeong, M. S. Oh, S. Im and J. H. Song, *J. Lumin.* **80** (1999) 281.
- [92] S. P. Withrow, C. W. White, A. Meldrum, J. D. Budai, D. M. Hembree and J. C. Barbour, *J. Appl. Phys.* **86** (1999) 396.

- [93] X. M. Wu, M. J. Lu and W. G. Yao, *Surf. Coatings Technol.* **161** (2002) 92.
- [94] G. Ghislotti, B. Nielsen, P. Asoka-Kumar, K. G. Lynn , A. Gambhir, L. F. Di Mauro and C. E. Bottani, *J. Appl. Phys.* **79** (1996) 8660.
- [95] D. I. Tetelbaum, S. A. Trushin, A. N. Mikhaylov, A. K. Mukhamatullin and D. M. Gaponova, *Proceedings of 8th Japan-Russian International Symposium on Interaction of Fast Charged Particles with Solids, Kyoto University, Japan, 24-30 November, 2002* (2003) 167.
- [96] M. L. Brongersma, P. G. Kik, A. Polman, K. S. Min and H. A. Atwater, *Appl. Phys. Lett.* **76** (2000) 351.
- [97] K. S. Zhuravlev, A. M. Gilinsky and A. Yu. Kobitsky , *Appl. Phys. Lett.* **72** (1998) 2962.
- [98] D. Kovalev, J. Diener, H. Heckler, G. Polisski, N. Künzner and F. Koch , *Phys. Rev. B* **61** (2000) 4485.
- [99] C. Delerue, M. Lannoo, G. Allan, E. Martin, I. Mihalcescu, J.C. Vial, R. Romestain, F. Muller and A. Bsiesy , *Phys. Rev. Lett.* **75** (1995) 2228.
- [100] V.A. Kharchenko and M. Rosen , *J. Lumin.* **70** (1996) 158.
- [101] X. Chen, J. Zhao, G. Wang and X. Shen, *Phys. Lett. A* **212** (1996) 285.
- [102] P. F. Trwoga, A. J. Kenyon and C. W. Pitt, *J. Appl. Phys.* **83** (1998) 3789.
- [103] J. B. Khurgin, E. W. Forsythe, S. I. Kim, B. S. Sywe, B. A. Khan and G. S. Tompa, *Mater. Res. Soc. Symp. Proc.* **358** (1995) 193.
- [104] J. G. Zhu, C. W. White, J. D. Budai, S. P. Withrow and Y. Chen, *J. Appl. Phys.* **78** (1995) 4386.
- [105] G. C. John and V. A. Singh , *Phys. Rev. B* **54** (1996) 4416.
- [106] M. Kapoor, V. A. Singh and G. K. Johri , *Phys. Rev. B* **61** (2000) 1941.
- [107] Y. Liu, T. P. Chen, Y. Q. Fu, M. S. Tse, J. H. Hsieh, P. F. Ho and Y. C. Liu, *J. Phys. D: Appl. Phys.* **36** (2003) L97.
- [108] D. V. Tsu, G. Lucovsky and B. N. Davidson, *Phys. Rev. B* **40** (1989) 1795.
- [109] M. Yamamoto, T. Koshikawa, T. Yasue, H. Harima and K. Kajiyama, *Thin Solid Films* **369** (2000) 100.
- [110] R. Turan and T. G. Finstead, *Semicond. Sci. Technol.* **7** (1992) 75.
- [111] S. Margalit, A. Bar-lev, A. B. Kuper, H. Aharoni and A. Neugroschel *J. Cryst. Growth.* **17** (1972) 288.

- [112] E. S. Marstein, A. Gunnæs, U. Serincan, S. Jørgensen, A. Olsen, R. Turan and T. G. Finstad, *Thin Solid Films* **158** (2003) 544.
- [113] Optical Properties of Semiconductor Nanocrystals, *S. V. Gaponenko, Cambridge University Press* (1998) 19.
- [114] A. G. Cullis, L. T. Canham and P. D. J. Calcott, *J. Appl. Phys.* **82** (1997) 909.
- [115] CRC Handbook of Chemistry and Physics, 84<sup>th</sup> ed. (2003-2004).

## APPENDIX A

### ABBREVIATIONS AND ACRONYMS

<b>BJT</b>	Bipolar Junction Transistor
<b>CVD</b>	Chemical Vapor Deposition
<b>EDS</b>	Energy-Dispersive X-ray Spectroscopy
<b>EL</b>	Electroluminescence
<b>FTIR</b>	Fourier Transform Infrared
<b>FWHM</b>	Full Width at Half Maximum
<b>LED</b>	Light Emitting Diode
<b>MBE</b>	Molecular Beam Epitaxy
<b>MOSFET</b>	Metal Oxide Semiconductor Field Effect Transistor
<b>PECVD</b>	Plasma Enhanced Chemical Vapor Deposition
<b>PL</b>	Photoluminescence
<b>SAD</b>	Selected-Area Diffraction
<b>SIMS</b>	Secondary Ion Mass Spectroscopy
<b>SRIM</b>	the Stopping and Range of Ions in Matter
<b>TEM</b>	Transmission Electron Spectroscopy
<b>TRIM</b>	the Transport of Ions in Matter
<b>XPS</b>	X-ray Photoelectron Spectroscopy
<b>XRD</b>	X-ray Diffraction

## APPENDIX B

### PHYSICAL PARAMETERS

Table B.1: Parameters of the most common semiconductors [113].

	Band gap energy $E_g, eV$	Exciton Bohr radius $a_B, nm$
Ge	0.74 <sup>a</sup>	17.7 <sup>b</sup>
Si	1.17 <sup>a</sup>	4.3
GaAs	1.52	12.5
CdSe	1.84	4.9
CdS	2.58	2.8
ZnSe	2.82	3.8
CuCl	3.40	0.7

<sup>a</sup> Indirect band gap

<sup>b</sup> Source: Cullis et al [114].

Table B.2: Bond Strengths In Diatomic Molecules [115].

Molecule	Bond Strength, eV
Ge-Ge	2.7
Ge-O	6.8
Ge-Si	3.1
Si-O	8.3
Si-Si	3.4

Table B.3: Melting Temperatures of Ge, Si and SiO<sub>2</sub> [115].

	Melting Temperature, °C
Ge	938
Si	1414
SiO <sub>2</sub>	1700

## VITA

Author of this work was born in 1973 at Nicosia as a Turkish Republic of Northern Cyprus citizen. He has achieved his BS degree in Physics Education in 1996 and MS degree in Physics in 1998 at METU. Presently he works as a research assistant in the Department of Physics, METU, Ankara.

### List of Publications:

1. “Can chemically-etched Ge or Ge nanocrystals emit visible PL?”, G. Kartopu, S. C. Bayliss, **U. Serincan**, R. Turan, R. E. Hummel, Y. Ekinici, A. E. Gunnæs and T. G. Finstad, *submitted to Physica Status Solidi (c)*.
2. “Introduction of interface states by Ge accumulation at the Si-SiO<sub>2</sub> interface by annealing Ge implanted SiO<sub>2</sub> films”, E. S. Marstein, A. E. Gunnæs, A. Olsen, T. G. Finstad, R. Turan and **U. Serincan**, *Journal of Applied Physics* (at press).
3. “Electrical and magnetic properties of Si ion implanted YBCO thin films and microbridges”, I. Avci, M. Tepe, **U. Serincan**, B. Oktem, R. Turan and D. Abukay, *Thin Solid Films* (at press, available online).

4. "Characterization of Ge Nanocrystals Embedded in SiO<sub>2</sub> by Raman Spectroscopy", **U. Serincan**, G. Kartopu, A. Guennes, T. G. Finstad, R. Turan, Y. Ekinici and S.C.Bayliss, *Semiconductor Science and Technology* **19** (2004) 247.
5. "Electrical properties of nitrogen implanted GaSe single crystal", O. Karabulut, M. Parlak, R. Turan, **U. Serincan**, E. Tasarkuyu and B. G. Akinoglu, *Crystal Research and Technology* **38** (2003) 811.
6. "Ultrathin oxynitridation process through ion implantation in a Poly-Si<sub>1-x</sub>Ge<sub>x</sub> gate MOS capacitor", A. P. Jacob, T. Myrberg, M. Friesel, O. Nur, M. Willander, **U. Serincan** and R. Turan, *Materials Science in Semiconductor Processing* **6** (2003) 37.
7. "Mechanisms of void formation in Ge implanted SiO<sub>2</sub> films", E. S. Marstein, A. Gunnæs, **U. Serincan**, S. Jørgensen, A. Olsen, R. Turan and T. G. Finstad, *Nuclear Instruments and Methods in Physics Research B* **207** (2003) 424.
8. "Nanocrystal and nanocluster formation and oxidation in annealed Ge-implanted SiO<sub>2</sub> films", E. S. Marstein, A. E. Gunnæs, **U. Serincan**, R. Turan, A. Olsen and T. G. Finstad, *Surface and Coatings Technology* **158** (2002) 544.

### International conferences/meetings:

1. “Can chemically-etched (porous) Ge or Ge nanocrystals emit visible PL?”, G. Kartopu, S. C. Bayliss, **U. Serincan**, R. Turan, R. E. Hummel, Y. Ekinici, A. E. Gunns and T. G. Finstad. Oral presentation in the 4<sup>th</sup> International Conference of Semiconductor Science and Technology (PSST 2004), Cullera-Valencia, Spain, March 14-19, 2004.
2. “On the analysis of semiconductor nanocrystals by Raman spectrometry”, **U. Serincan**, G. Kartopu, S. C. Bayliss, A. Guennes, T. G. Finstad and R. Turan. Poster presented at the International School and Workshop on Nanotubes & Nanostructures, Frascati, Italy, September 15-19, 2003.
3. “Nitridation of ultrathin oxide MOS poly-Si<sub>1-x</sub>Ge<sub>x</sub> capacitor through ion implantation”, A. P. Jacob, T. Myrberg, M. Friesel, O. Nur, M. Willander, **U. Serincan** and R. Turan. Poster presented in Challenges in Predictive Process Simulation (ChiPPS-2002), Prague, Czech Republic, October 13-17, 2002.
4. “Vanishing nano Ge crystal balls” T. G. Finstad, R. Turan, A. E. Gunns, **U. Serincan**, E. Marstein and A. Olsen. Poster presented at the International Workshop on Nanostructures for Electronics and Optics, Dresden, Germany, August 18-21, 2002.

5. “Evolution of Ge nanostructures formed by ion implantation in SiO<sub>2</sub>” R. Turan, T. G. Finstad, **U. Serincan**, A.E. Gunnæs, E. S. Marstein, A. Olsen and G. Kartopu. Poster presented at the 2nd Workshop on Nanomaterials: Fundamentals and Applications, COST meeting, Sevilla, Spain, August 18-21, 2002.
6. “The effect of processing parameters on the formation of Ge nanocrystals in SiO<sub>2</sub>” A. E. Gunnæs, E. S. Marstein, **U. Serincan**, R. Turan, S. Jørgensen, T. G. Finstad and A. Olsen. Poster presented at the Materials Congress, London, England, April 9-11, 2002.
7. “Ion beam synthesis of Ge nanoclusters in SiO<sub>2</sub>” E. S. Marstein, A.E. Gunnæs, **U. Serincan**, R. Turan, A. Olsen, T. G. Finstad. Poster presented at the 12<sup>th</sup> International conference on surface modification of materials by ion beams, (SMMIB2001), Marburg, Germany. September 9, 2001.

**National conferences/meetings:**

1. “Formation of Si and Ge nanocrystals in SiO<sub>2</sub> matrix by ion implantation for optical and electrical applications”, **U. Serincan**, R. Turan, G. Kartopu, A. Gunnæs and T. G. Finstad. Poster presented at 5<sup>th</sup> National Optic, Electro-optic, and Photonic Meeting, Ankara, Turkey, December 12, 2003.
2. “Voids formation in SiO<sub>2</sub> layer”, **U. Serincan**, R. Turan, T. G. Finstad, A. Gunnæs, E. Marstein, A. Olsen. Poster presented at 9<sup>th</sup> National Condensed Matter Physics Meeting, Ankara, Turkey, December 20, 2002.

3. “İyon ekme yöntemi kullanarak azot ile katkılandırılmış GaSe kristalinin elektriksel karakterizasyonu”, O. Karabulut, M. Parlak, R. Turan, **U. Serincan**, B. G. Akinođlu. Poster presented at 8<sup>th</sup> National Condensed Matter Physics Meeting, Ankara, Turkey, November 9, 2001.